AUTOMATIC DETECTION, SEGMENTATION AND MOTION CHARACTERIZATION OF THE HEART FROM TAGGED MRI

BY ZHEN QIAN

A dissertation submitted to the

Graduate School—New Brunswick

Rutgers, The State University of New Jersey

in conjunction with

The Graduate School of Biomedical Sciences

the University of Medicine and Dentistry of New Jersey

in partial fulfillment of the requirements for the

Joint Degree of Doctor of Philosophy

Graduate Program in Biomedical Engineering

Written under the direction of

Dimitris N. Metaxas and Leon Axel

and approved by

_____

_____

_____

_____

_____

New Brunswick, New Jersey

May, 2008

ABSTRACT OF THE DISSERTATION

Automatic Detection, Segmentation and Motion Characterization of the Heart from Tagged MRI

by Zhen Qian

Dissertation Director: Dimitris N. Metaxas and Leon Axel

Cardiac disease is the leading cause of death in the developed countries. To reduce the mortality, early diagnosis is critical. Tagged MRI is a non-invasive technique for the study of cardiac deformation. It generates an MRI-visible tag pattern within the heart that deforms with the tissue during the cardiac cycle in vivo, which gives motion information of the myocardium. It has the potential of early diagnosis and quantitative analysis of various kinds of heart diseases and malfunctions. The difficulty preventing this technique from clinical use is the lack of efficient post-processing methods that automatically extract and analyze cardiac motion from tagged MRI data, which consists of image analysis tasks such as image preprocessing, tagging lines enhancement and tracking, tag removal, heart detection, cardiac boundaries segmentation, and motion or strain estimation. In this dissertation, a system of accurate and reliable automatic / semi-automatic tagged MR image analysis solutions will be given to all these problems. The methodologies of this system involves the interplay between traditional image processing techniques and state-of-the-art statistics, physics and machine learning based methods. In addition, medical prior knowledge and practices have been incorporated into the algorithms. In this research, a wavelet-like Gabor filter-based method has been developed to solve tasks such as tag enhancement, tag removal, myocardial tracking,

and strain estimation. Because of its wide applications, Gabor filtering has the potential to become a routine function in tMRI analysis systems. We are also the first that introduced learning-based approaches into the detection and boundary segmentation of the heart in cardiac tMRI, by integrating statistical shape analysis, learning-based local appearance modeling, and sampling-based tracking techniques. For myocardial deformation analysis, we developed both tracking and non-tracking-based strain estimation algorithms, and conducted a quantitative comparison with registered ultrasound elastography. Based on our strain estimates, a novel tensor-based classification framework has been developed to identify and localize regional cardiac abnormalities in human subjects. Experimental results show the automatic detection, segmentation and motion characterization methods that we have developed in this dissertation can automate and largely speed up the image analysis process of tMRI, and achieve robust and accurate results. This research provides a promising avenue to make tMRI clinically accessible.

Acknowledgements

First of all, I would like to thank my advisors, Professor Dimitris Metaxas and Professor Leon Axel, for their constant support, encouragement and guidance in this research. I have greatly benefited from Professor Metaxas's keen appreciation of the frontiers and challenges in Medical Image Analysis and Computer Vision. His insightful discussions and advice significantly contributed to the smooth and successful completion of this dissertation. I am grateful to Professor Axel who exposed me to the fascinating research areas of Radiology, Medical Image Processing, and Cardiovascular Research. Always friendly, patient, and willing to offer help, Professor Axel has been a wonderful source of knowledge and support. I am very fortunate to have them as my mentors.

I would like to thank the other members of my doctoral committee: Prof. John Li, Prof. Nada Boustany and Prof. Anant Madabhushi for their valuable advice, help and suggestions regarding this dissertation. I am grateful to Prof. Li for being my committee chair. I thank Prof. Madabhushi for his many enlightening discussions and suggestions during my preparation for the dissertation proposal.

Thanks also go to Professor Elisa Konofagou and her student Wei-Ning Lee, and Professor David Shreiber and his student Jason Maikos for our fruitful collaborations.

I thank my colleagues for the close team working environment and friendly atmosphere at the Center for Computational Biomedicine Imaging and Modeling (CBIM). I am grateful to Xiaolei Huang (now Professor) for her warm-hearted help and enlightening discussions regarding this research. Thanks also go to Qingshan Liu, Rui Huang, Xiaoxu Wang and Ting Chen, for our productive collaborations. I thank Rong Zhang, Kyoungju Park, Atul Kanaujia, Zhiguo Li, Viorel Mihalef, Jinghao Zhou, Suejung Huh, Chansu Lee, Peng Yang, Junzhou Huang, and Yuchi Huang for their friendship, help, and the enjoyable research life together. Thanks also go to Tushar Manglik, Jöel

Schaerer and other members in the Radiology Department at NYU Medical Center.

Finally, I wish to express my deepest gratitude to my parents Qian Bingliang and Yang Shimin, and my sister Qian Feng. Without their unconditional love and support, I cannot go this far.

Dedication

Dedicated to my parents Qian Bingliang and Yang Shimin

and my sister Qian Feng

Table of Contents

Abstract ii

Acknowledgements iv

Dedication vi

List of Tables xii

List of Figures xiii

1. Introduction 1

1.1. Motivation 1

1.2. Specific Goals 3

1.3. Structure of dissertation 5

2. Background 7

2.1. Brief Introduction of Tagged MRI 7

2.2. Related work 8

2.2.1. Image Preparation 8

2.2.2. Tag Segmentation and Tracking 9

2.2.3. Tag Removal 9

2.2.4. Myocardial Boundary Segmentation 10

2.2.5. Strain Estimation 10

3. Tag Extraction and Tracking 12

3.1. Image Preprocessing 12

3.1.1. Background 12

3.1.2. Methodology 13

3.1.3. Experimental Results 14
3.1.4. Other Applications 15
3.2. 2D Tagging Lines Enhancement and Tracking Using Gabor Filter Bank 17
3.2.1. Background 17
3.2.2. Methodology 18
Basic definitions 19
Gabor Filter Bank Design for Tagging Line Extraction 20
Normalization 23
3.2.3. Experimental Results 23
3.2.4. Tagging Lines Tracking 24
Tracking Results 28
3.3. 3D Gabor Extension and 3D Tagging Sheets Tracking 28
3.3.1. Background 28
3.3.2. Methodology 30
Basic Definitions: 3-D Gabor filter 30
3D Gabor filters design 31
Interpolation and Parameter Tuning 34
3.3.3. Experimental Results 34
3.4. Conclusion 37

4. Tag Removal 38
4.1. Gabor-based Tag Removal 39
4.1.1. Background 39
4.1.2. Methodology 39
4.1.3. Preprocessing for Grid Tagging Data 41
4.1.4. Experimental Results 43
4.2. Band-Stop Filtering-Based Tag Removal 44
4.2.1. Background 44
4.2.2. Methodology 46

Partition The Spectrum Image Via Mean Shift 48
Model Harmonic Peaks Via PCA Analysis 49
4.2.3. Experimental Results and Applications 51
4.3. Conclusion 53

5. Boundary Segmentation 55
5.1. Boundary Segmentation via Tag removal and 4D Spatio-temporal Propagation 56
5.1.1. Background 56
5.1.2. Methodology 57
MetaMorphs Segmentation on Tag Removed Image 57
Myocardial tracking 58
Integration and the Prototype System 61
5.1.3. Experimental Results 64
5.1.4. Discussion 64
5.2. Learning-based Segmentation Approach 66
5.2.1. Background 66
5.2.2. Methodology 67
ASM Shape Modeling 68
Learning Boundary Criteria Using Adaboost 70
Segmentation Based On Confidence Ratings 73
5.2.3. Automatic Initialization: Heart Detection 74
Feature Design 76
The Attentional Cascade Detection 76
Detection Experiments and Results 77
5.2.4. Experimental Results and Validation 81
5.2.5. Discussion 83
5.3. Boosting and Nonparametric Based Boundary Tracking 85
5.3.1. Background 85

5.3.2. Methodology . . . 86
Shape Modeling and Boosting The Boundary Criteria . . . 86
Nonparametric Shape Tracking . . . 89
5.3.3. Experimental Settings and Results . . . 92
5.3.4. Discussion . . . 93
5.4. Conclusion . . . 94

6. Strain Estimation and Regional Cardiac Function Analysis . . . 96
6.1. Introduction . . . 96
6.2. Tracking Based Strain Estimation in 2D tMRI . . . 97
6.2.1. In Case of 1D Tagging Lines . . . 97
6.2.2. In Case of 2D Tagging Grids . . . 98
6.2.3. Strain Calculation From Tracking . . . 99
6.3. Comparison With Registered Ultrasound Myocardial Elastography . . . 102
6.3.1. Ultrasound And tMRI Data Acquisition . . . 103
6.3.2. Rigid-body Registration of 2D Elastography with 3D Tagged MRI 104
6.3.3. Strain Estimation . . . 106
Ultrasound Myocardial Elastography . . . 106
Tagged MRI . . . 107
6.3.4. Experimental Results . . . 108
6.3.5. Discussion . . . 112
6.4. Non-tracking Based Strain Estimation . . . 113
6.4.1. Gabor Filter Design . . . 114
6.4.2. Strain Estimation . . . 114
6.4.3. Evaluation on Phantom Images . . . 116
6.4.4. Experiments On Real Data . . . 121
6.4.5. Discussion . . . 121
6.5. Identifying Regional Cardiac Abnormalities Using Tensor Analysis . . . 123
6.5.1. Quantitative data preparation . . . 125

6.5.2. Spatio-Temporal Tensor LDA 126
Learn the classifier 126
Regional abnormality analysis 128
6.5.3. Experiments and Results 129
6.5.4. Discussion 131
6.6. Conclusion 132

7. Conclusions and Future Topics 134

References 137

Curriculum Vita 145

List of Tables

5.1. Average error distances. 82

5.2. Average cross distances 83

5.3. Myocardial wall tracking algorithm 92

5.4. Error analysis in millimeters. 95

6.1. The ST-LDA algorithm. 128

6.2. Comparison with other conventional classification algorithms. 130

List of Figures

1.1. The framework of the whole dissertation. 5

2.1. Some examples of the tagged cardiac MRI images. 7

3.1. An example of intensity inhomogeneity in tagged cardiac MRI images. 12

3.2. The histogram of the input 4D tagged MR image. i_0 is the intensity threshold to determine whether a voxel belongs to the foreground or the background. 14

3.3. (1a) is the down-sampled 2D slice of a 4D input image set. The original image can be found in 3.1; (1b) is the foreground image I_f. (2a) is the Gaussian blurred foreground image; (2b) is the inhomogeneity corrected image I_b. Image (1a), (1b) and (2a) are down-sampled to achieve faster implementation. 15

3.4. (1a) is the 3D view of a down-sampled 3D abdominal MRI set; (1b) is the 3D view of the foreground image I_f. (2a) is the 3D view of the Gaussian blurred foreground image; (2b) is the 3D view of the inhomogeneity corrected image I_b. Image (1a), (1b) and (2a) are down-sampled to achieve faster implementation. 16

3.5. Simplified 1D model of HARP and Gabor filters in frequency domain (left) and spatial domain (right). Upper is HARP; lower is Gabor filter bank. A Gabor filter bank uses the combination of a group of Gabor filters to selectively cover the whole bandpass frequency range; each single filter can still get full constraints in its spatial domain, but HARP cannot. 18

3.6. Real part of a Gabor filter in the spatial domain. 21

3.7. The indicated pixel is the first harmonic peak of the tagged image in the Fourier domain. By finding the location of this peak, (U, V) can be determined by its coordinates. 22
3.8. Different θ fits different cardiac region. 23
3.9. A shape modified Gabor filter with $p = 3$ that has a more similar appearance with the tagging line. 24
3.10. (a) Three tagged cardiac MR images in short axis. They are taken from an MRI sequence during systole. (b) The output results of our method. (c) HARP's phase angle result. The myocardium contours are drawn manually for better readability. 25
3.11. Initialization of the Snake set. 26
3.12. The model of our tagging lines tracking *Snakes*. 27
3.13. Tracking results at phases of mid-systole (lhs) and end-systole (rhs). . . 28
3.14. (a) shows tagging lines are intersections of the tagging sheets and the imaging planes. (b) shows a 3D tagged MR image dataset. 29
3.15. (a) A slice view of a 3D Gabor filter. (b) An iso-surface view of a 3D Gabor filter. Here $\sigma_{x'} = \sigma_{y'} = \sigma_{z'}$, which makes the Gaussian envelope symmetric and the iso-surfaces in (b) circle-shaped; the normal of these iso-surfaces are (1,1,1), because $U = V = W$. 31
3.16. (a) Tagging sheet's rotation has three possible orientations. But only ϕ, ψ are observable. The in-plane rotation φ is ignored. (b) The y axis is set to be parallel to the initial tagging lines. 32
3.17. A Slice view of a 3D Gabor Filter used in our experiment. 33
3.18. a) A slice view of the 3D Segmentation result. b) The two tagging sheets that are tracked along time sequences. Tracking results of the sheets are shown in Fig 3.20. 35
3.19. The rotation angle ψ at time $t + 1$ is constrained by the angle ω and θ at time t, which prevents tagging sheets aliasing. 35

3.20. Tracking results for two tagging sheets at different locations (from time 1 to time 6). The warm color in (a) represents the tagging sheet motion out of the plane and away from the viewer, and the cold color in (b) represents the tagging sheet motion out of the plane and towards the viewer. A deformable mesh is imposed onto each tagging sheet at time 1, and captures the deformation over time. 36

4.1. Tagged cardiac MR sample images in the short axis view. The heart is located at the center of the image with deformed tag patterns. (a) is an example of line pattern, and (b) is an example of grid pattern. Both tag patterns are routinely used in research and clinical environments. . . . 38

4.2. The real and imaginary parts of a 2D complex Gabor filter. We can see the 2D sinusoid of the imaginary part is shifted by $\pi/2$ from that of the real part. 40

4.3. After Fourier transform, the grid tagging image has four first harmonic peaks and other higher order harmonic peaks in its spectral domain. . 42

4.4. The framework of the low-pass filtering method used to separate the grids data into two sets of tagging lines. 43

4.5. The results of the tagging lines image derived from the grid data. Row 1 is the input grid data. Row 2 is the derived image with horizontal tagging lines. Row 3 is the derived image with vertical tagging lines. . . 44

4.6. Tag removal results. Examples of original images (a1 and b1) with their tag removed images (a2 and b2). Notice that the first image in (a1) is taken right after the initial tagging administration, and the tagging lines in the blood pool are not flushed way yet, which leads to an unsatisfactory tag removal results 45

4.7. (a) A tagged cardiac MR sample image in the short axis view. The heart is located at the center of the image with deformed tagging lines. (b) The magnitude spectrum image of (a). This image is symmetric w.r.t. the center origin. Besides the low frequency region, it has four visible harmonic peaks, two first harmonics and two second harmonics. 46

4.8. The flowchart of our proposed framework. First the input image is transformed to the frequency domain. Then the spectrum image is divided into regions based on the spectral energy peaks. Third, for regions containing a harmonic peak (there are the first and the second harmonic peaks in the image), we fit a 2D Gaussian to model it. Finally the band-stop filters are designed to attenuate the 2D Gaussian regions. The output image is from the inverse Fourier transform of the filtered spectrum image. 47

4.9. (a) shows the mean shift tracks starting from four pixels, two of which converge to the first harmonic peak, and the other two converge to the low frequency. (b-d) are the partition results using $\sigma = 3$, 4, and 5.5 respectively. 49

4.10. We compare our new method with the previous Gabor-based method. Here we listed two time sequences. Rows (a) show the input tagged MR images. Rows (b) show the tag removed results from our new method. Rows (c) are results from the previous Gabor-based method. The red curves are the segmentation results. Note that for the first few frames in a time sequence, the previous method cannot help with the segmentation, because the tag pattern still remains in the blood pool. 52

4.11. An example of the papillary muscle segmentation on the tag removed images. The first row is the input image sequence. The papillary muscles are drawn in red in the second row. 53

4.12. An unsuccessful example of the band-stop filtering method applied on grid tagging data. The contrast between the myocardium and blood pool is so low that it is difficult to differentiate them even if the tagging grids are removed. 54

5.1. MetaMorphs segmentation on de-tagged images. (1) segmentation at time 7, slice position 7. (2) segmentation at time 7, slice position 10. (a) original image. (b) image with tags removed by gabor filtering. (c) cardiac contours segmented by MetaMorphs on de-tagged image. (d) contours projected on the original image. 58

5.2. (a) The upper left image is the original input MR image. The upper right one is the spacing m map. The warm color indicates the spacing between tagging lines is smaller, and the cold color indicates the spacing is bigger. The lower left image is the orientation $\Delta\phi$ map. The warm color means the orientation of the tagging lines is from lower left to upper right; the cold color means the orientation is from lower right to upper left. The lower right image is the phase ω map. The color varying from dark to bright means the phase angles vary from $-\pi$ to $+\pi$. The gray areas in the maps mean the parameters are not changed or there is no tagging lines. (b) illustrates the relationship between tag spacing and the phase shift. 60

5.3. A mesh is imposed on the myocardium area and deforms along time. We can find the mesh contracts properly overall as the underlying heart tissue contracts. But in local regions, the mesh deformation results are not accurate enough. This is because our model is wholly based on the tag texture feature, which may very likely be corrupted by the neighboring boundaries and the high level noise. 61

5.4. The framework of our automated segmentation in 4D spatio-temporal MRI-tagged images. We start at a center time when the tag lines are flushed away in the blood area while they remain clear in the myocardium. Boundary segmentation is done in several key frames on the de-tagged images before the boundary contours are spatially propagated to the other positions. Then at each position, the boundaries are temporally propagated to other times. 62

5.5. Screen snapshots of our segmentation and tracking system. (1a) read in the SA and LA volumes. (1b,1c,2a) examine the data sets. (2b) de-tagged image at the center time. (2c,3a) MetaMorphs segmentation based on de-tagged images. (3b,3c) segmentation results. The papillary muscle is excluded from the myocardium by manual interaction. (4a,4b) temporal propagation. (4c) a segmentation result after manual correction. 65

5.6. (a) Here we used 50 points to represent one set of contours. (b) shows the the shape variations by the first six principle components. The 2^{nd} and 5^{th} columns are the mean shapes. The shapes to the left and right sides of the mean shapes are the variate shapes produced by adding or minus a certain amount of a principal component. 69

5.7. Sample sets of feature filters: (a) are the derivatives of Gaussian used for edge detection, (b) are the second derivatives of Gaussian used for ridge detection, and (c) are the half-reversed Gabor filters used for tag line breakpoint detection. 71

5.8. The illustration of the method to set the training data. The solid box is the positive sample around the landmark points. The four dashed line boxes along the normal are the negative samples. This way of setting the negative samples is chosen to make the classifier more adaptive to the particular landmark position. 72

5.9. (a) and (b) show the training error (solid lines) and testing error (dash lines) of two landmark points versus Adaboost iteration times. (a) is a point on the LV, (b) is a point on the Epi. Note how the training and testing error decrease as Adaboost iterates. Also note the testing error of (a) is higher than (b): we are more confident of landmark point (b)'s classification result. 73

5.10. Example features. They are two-rectangle and four-rectangle features with different orientations. The white-colored pixels equal 1, the black-colored pixels equal -1, and the gray equal 0. In total there are 62208 features in a (24x24) sized image. 76
5.11. An illustration of integral image. Sum within rectangle $D = ii_4 + ii_1 - ii_2 - ii_3$. 77
5.12. A feature example, whose filtered result $= ii_5 + ii_1 - ii_2 - ii_4 - (ii_6 + ii_2 - ii_3 - ii_5)$. 77
5.13. Five cascade stages with a total number of 100 features are used. At the first stage which consists of only one feature, 124915 out of 127020 candidate sub-images are rejected. At the second stage, 1865 sub-images are rejected, and so on. Finally in a certain image we have total 44 detections. The highest boosting result is chosen as the final detection. We can see during the first two stages, most sub-images are rejected, which makes the computation faster. 78
5.14. A random sample of the heart training set. 79
5.15. The first five features Adaboost selects compared with a training image. 79
5.16. This figure shows the error of the weak classifier that Adaboost selects at each boosting round. The error increases non-monotonously as the distribution of the training examples becomes more difficult to classify. . 80
5.17. This figure shows the error of the strong classifier on the training data. The error drops to zero after five rounds. 80
5.18. This figure shows the error of the strong classifier on the testing data. The testing error continues to decrease after the training error approaches zero, which means more iterations leads to larger margin and higher accuracy. 81
5.19. Three representative detection results. For image (c), the image was rotated by a set of discrete angles before the detection, and the final detection is of the highest probability among all the discrete angles tested. 82

5.20. The first and second rows of images come from the the first and second dataset, respectively. For better representation, the images in the first row vary in position and remain at the same phase, while the images in the second row vary in phase but remain at the same position. The solid contours are from our automatic segmentation method; the dashed contours are manual. Notice that the papillary muscles in LV are excluded from the endocardium. The third and fourth rows are from the third dataset. Manual contours are not available for this dataset, so we compare our segmentation results between the the horizontal and vertical tagged images that are at same position and phase. Qualitatively, the contours are quite consistent, allowing for possible misregistration between the nominally corresponding image sets. In (3a), (3c) and (3e) the dashed contours are testing examples of poor initializations, while the final contours are solid. Although the initialization is far away from the target, the shape model moves and converges well to the target. . . 84

5.21. The flow chart of our proposed framework illustrates the learning and tracking processes. In the manual contour block, the red circles indicate the cusp points between the septum and the RV endocardium. The green circle indicates the location of papillary muscle. In the dynamic block, cooler color turning into warmer color indicates the dynamic model's evolution during systole. 87

5.22. (a) shows 3 sample sets of static feature filters, from top to bottom, the derivatives of Gaussian used for edge detection, the second derivatives of Gaussian used for ridge detection, and the half-reversed Gabor filters used for tag line breakpoint detection. (b) illustrates the function of the motion feature filter, which helps remove the tangential motion. 90

5.23. The testing error rates of the boundary criteria boosting. The red curve which integrates both motion and static features has lower error rates than the other two. 91

5.24. Snapshots from three example sequences of our experimental results. The solid contours are from our tracking method, while the dashed are from manual segmentations. The first 2 rows are data from 2 normal subjects. The last row is from a patient with heart failure. Note that our tracking method can exclude the papillary muscle from the ventricle endocardium, and always keep the cusp points at the RV-LV junctions. 93

5.25. The mean error for each time sequence measured in pixel. The red solid curve represents the overall error. The blue dashed, black dash-dot and green dotted curves represent the mean error distances in the LV, RV endocardium and epicardium respectively. 94

6.1. Four sequential tracking examples (a to d) during systole. 98

6.2. Four sequential tracking examples (a to d) during systole. Note that only the nodes inside the myocardium are tracked by spline-based method. . 99

6.3. Displacement in vertical and horizontal coordinates. 100

6.4. Strain map in vertical and horizontal coordinates. 101

6.5. Strain map in radial and circumferential coordinates. 102

6.6. The flowchart of the rigid-body registration framework. The stack of the untagged images is interpolated using splines to achieve a 3D isotropic volume. The user can freely tune the translation and rotation parameters of the US imaging plane. After manual initialization, a pseudo US image is constructed from the untagged MRI. The position of the simulated US probe gives the US beam direction. Finally a mutual information-based registration procedure is performed to fine-tune the manual initialization. 105

6.7. Strain pattern comparison between tMRI and UME on a healthy subject. Horizontal and vertical strains of the left ventricle are displayed. For each strain component, four time frames are shown from the end-of-diastole (ED) phase to the end-of-systole (ES) phase. The pseudo color is displayed on a scale of the strain value from -0.5 to 0.5. 108

6.8. Strain pattern comparison between tMRI and UME on a healthy subject. Radial and circumferential strains of the left ventricle are displayed. For each strain component, four time frames are shown from the end-of-diastole (ED) phase to the end-of-systole (ES) phase. The pseudo color is displayed on a scale of the strain value from -0.5 to 0.5. 109

6.9. Illustrates the division of the 6 sectors. 110

6.10. In each sector of the LV, the mean and standard deviation of the radial and circumferential strain values are calculated from end-diastole to end-systole. We find that the UME results have an overall trend which is similar with that of the tMRI. However the standard deviation of the US results tends to keep growing quickly, while that of the tMRI remains stable. 111

6.11. The strain error mean of the UME technique compared with tMRI. We find in UME modality, from ED to ES, the errors are also accumulative. 112

6.12. The illustration of $\mathbf{F}$ calculation. After tag deformation, $d_x = S_x \cos\Delta\phi_y / \sin\phi$, and $d_y = S_y \cos\Delta\phi_x / \sin\phi$, which are used in Equation. 6.10. 115

6.13. These two rows are the simulated phantom images with horizontal and vertical tagging lines, which undergo an inward contraction with a rotation from t_0 to t_4. 117

6.14. The deformations are extracted from the phantom images at t_4 using our Gabor filter method. 117

6.15. The comparison of the ground truth and our estimation. Circumferential strain, radial strain and rotation angle at t_1 to t_4 are compared. 118

6.16. Quantitative comparisons of the mean and standard deviation, at each time frame, of the radial strain (left-hand-side), the circumferential strain (middle) and the rotation angle (right-hand-side) show our estimations are consistent with the ground truth. 119

6.17. A representative of real world tagged MR images whose left ventricle in the input image is noisy, which leads to irregular estimations of S_{x_0}/D and $\Delta\phi_{x_0}$. After 3 smoothing iterations, we get a smoother LV area and better estimations of S_{x_3}/D and $\Delta\phi_{x_3}$. 119
6.18. The flowchart of the smoothing method. 120
6.19. Quantitative analysis of the rotation angle (first row), the circumferential strain (second row) and the radial strain estimations (third row) w.r.t. the iteration number of the smoothing loop. 120
6.20. Visual comparison of normal (left-hand-side) and patient's (right-hand-side) circumferential strain (first row), radial strain (second row) and rotation angle (third row) estimations at time t_1, t_4 and t_6. For quantitative analysis, we divide the LV into 6 sectors, which is illustrated in the lower-left image. 122
6.21. In each LV sector, at each time frame, we calculate the mean value of the radial strain (left), the circumferential strain (middle) and the rotation angle (right). Thus, the colored surfaces illustrate the temporal and spatial distributions of the estimated values. The first row is from normal data. The second row is from patient data. 123
6.22. The left ventricle is divided into 20 regions. 125
6.23. Visual comparison of normal (left-hand-side) and patient's (right-hand-side) radial strain (first row), circumferential strain (second row) and rotation angle (third row) estimations at the time of ED, MS and ES. For regional cardiac function analysis, we divided the left ventricle into 20 regions and interpolate the ED to ES deformation sequence into 10 frames, so as to form a 60×10-sized feature tensor $\mathbf{T}$, which is illustrated as a pseudo-color bar. 126

6.24. Quantitative analysis of the regional abnormality from the back-projection. Warm color represents high P value, which means high degree of abnormality. The first row shows the sampling images at ES from 4 time sequences. The second row shows the analysis results. Column (a) is from a normal sequence. Column (b) is from an abnormal subject. (c) and (d) are from a patient before and after a surgery, respectively. The black dots show the surgery sites. 131

Chapter 1

Introduction

1.1 Motivation

Cardiovascular diseases (CVDs) are the leading cause of death globally. According to a report of the World Health Organization [1], each year about 17.5 million people die from CVDs, accounting for 30 percent of all global deaths. Although over 80% of CVD deaths take place in developing countries, CVDs are more fatal in the western world. Indeed, CVDs have been the number one killer for 80 years in the United States [2]. It is estimated that one in three American adults has one or more types of CVDs. Each year more than 800,000 people in the United States die from heart diseases, accounting for more than 35 percent of all deaths.

Heart diseases usually begin and develop unnoticeably. Nesto et al [3] reported that abnormal alternations in myocardial motion and contractility occur earlier than patient's feeling of uncomfortable or pathological symptoms' showing up in electrocardiogram (ECG). Since the principal work of a heart is to pump blood, myocardial motion and contractility are of the most important indicators of the cardiac function. They are highly correlated to various cardiovascular diseases or disfunctions. To reduce the mortality of cardiovascular diseases, early screening and diagnosis of myocardial motion abnormality are of great importance.

Current cardiac tomographic imaging methods consist of echocardiography (ultrasound), high speed radiographic CT, conventional MRI, and tomographic radionuclide imaging methods such as single photon emission computed tomography (SPECT) and positron emission tomography (PET) [4]. Ultrasound imaging is non-invasive and economical. But its image quality is relatively poor with the heavy speckle noises, where detailed cardiac structures are difficult to observe. Speckle tracking-based myocardial

strain estimator has been recently developed to quantify myocardial contracility. However there is still an inconclusive debate on this method's validity, especially on the validity of utilizing the speckle noise as the material markers.

CT-based tests are more expensive and invasive than ultrasound. At the same time, a common drawback of current CT imaging methods is their relatively slow acquisition procedure and weak ability of detecting motions. Recently multi-slice and multi-detector CT techniques [5, 6, 7, 8, 9, 10] have been developed to increase the temporal resolution of the CT acquisition. However, it results in a relatively high radiation exposure, which is equivalent to approximately 100-600 chest X-rays.

On the other hand, magnetic resonance imaging (MRI) has also been widely used in cardiac disease diagnosis [11, 12]. Not like CT, MRI has no ionizing radiation. Comparing with ultrasound, MRI has higher spatial resolution and higher SNR. MR images can be taken in any desired plane, and give excellent soft tissue contrast without the application of a contrast agent. The short acquisition time of MRI makes cine MRI possible. Cine MRI reconstructs about 20-30 images within a heart beat cycle, which is much higher temporal resolution than current cine CT technique.

Both CT and MRI techniques are good at depicting the cardiac boundaries, i.e., the inner and outer surfaces of the heart walls. By tracking the deformation of the heart wall boundaries, we can estimate the heart's global motion and assess the global cardiac function, such as the ejection fraction. However, many disorders of cardiac function do not affect the heart wall uniformly. It is thus essential to assess the detailed and localized intramural motion pattern. The lack of reliable identifiable landmark points on the heart wall boundaries or in the myocardium severely limits the localized myocardial function assessment, where only the radial component of the myocardial motion can be inferred from the heart wall motion; the circumferential and twisting components are invisible by conventional CT or MRI. Hence, in order to quantify regional myocardial motion, it is desirable to non-invasively label landmarks within the myocardial tissue in-vivo and let the landmarks move with the heart muscle during heart beats. This was not possible until MRI tagging technique was first developed about one and a half decades ago.

Tagging is a unique feature of MR imaging. In the tissue being imaged, specified regions are un-magnetized at the beginning of the imaging process and remain un-magnetized for a short period of time during imaging. The un-magnetized tissues have dark appearance in MR images and serve as material markers in the resulting cine MRI. Cardiac tagged MRI (tMRI) is the most important application of MRI tagging. It labels the myocardium with tagging patterns of parallel lines or grids. By extracting and tracking the tagging lines or grids through a heart beat, we can non-invasively assess the localized intramural motion and deformation [13, 14].

Although MRI tagging has been invented for more than a decade, the development of efficient image processing and analysis methods has lagged significantly behind those for the imaging itself. The process of tagged MR image analysis is generally still too labor intensive to be used for anything more than limited-scale studies of cardiac function. A typical set of cardiac tMRI 4D data consists of 600-1000 images, which vary in imaging positions, times, and tagging orientations. Manually processing this huge amount of images is prohibitively time consuming. In order to put tMRI into routine clinical use, or research applications that involve a large number of subjects, automated image processing and analysis methods are essential.

1.2 Specific Goals

The principal goal of this dissertation is to develop automated image processing and analysis techniques for cardiac tagged MRI. In order to make the technique of tMRI available in routine clinical use, the developed image analysis methods must be highly accurate and robust. To achieve these requirements, we have a set of inter-related specific goals.

First, the myocardial motion information is extracted from the deformed tagged pattern. We need to develop automated methods to extract and track the motion of the tagging lines or grids in cine MRI. However, the saturated magnetization in the myocardial tissue decreases quickly and largely disappears in about half of a heart beat, due to T1 relaxation. Thus the first important image preparation step is tag

enhancement, which will help us identify and track the tags. In a single 2D tMRI image set, tracking is performed on the tagging lines or grids in the 2D imaging plane. In a set of stacked 3D tMRI, tracking results in the neighboring slices should also be considered to help with the tracking in the current slice because of the spatial correlation. Therefore tracking the virtual tagging sheets in 3D is desirable.

Another goal of this research is to develop methods to segment the boundaries of the myocardium. Finding myocardial boundaries is critical for accurate tag extraction and tracking. Boundary segmentation confines the tracking region in the myocardium, so as to avoid the effect from the tagged patterns off the myocardium. On the other hand, myocardial segmentation is also required for 3D heart modeling. To incorporate the three mutually orthogonal motion components, a 3D model of accurate geometry needs to be constructed and deformed in a finite element model framework. In this dissertation, we will focus on two main approaches for boundary segmentation in tMRI. First, we will investigate the tag-removal methods in tMRI. As stated before, the tagged patterns are non-invasively added as material markers in the MR images to track the myocardial motion. However they also add difficulties in boundary segmentation, because the dark tags interfere with the boundaries and the intensity-homogenous regions, which makes the conventional edge or region based segmentation methods not suitable for tMRI. If we remove the tagging lines or grids in tMRI, boundary segmentation will be largely facilitated. Second, we will introduce machine learning methods into the boundary segmentation problem. The myocardial boundaries consist of several contours of the heart's geometry. It is desirable to learn a statistical shape model to help with the segmentation. Furthermore, although corrupted by the tagging patterns, the boundaries are still distinguishable by observing the local appearance. We can use machine learning methods to find certain local appearance features. In this way, we will segment tagged image without the tag-removal step.

The primary goal of the image analysis in tMRI is to automatically assess the mechanical properties of the ventricular muscle from MRI tagging. Here we use myocardial strain to describe this property. Strain is mathematically termed as the derivative of material displacement. We propose two methods for the strain estimation. First, the

strain calculation is based on the tag tracking results as described previously. Second, strain is formulated as the change ratio of the local tagging lines' or grids' spacings. To assess the strain estimate from tMRI, we will compare it with the strain result from registered ultrasound elastography. The intermodal comparison can give deeper insights into the both imaging modalities. Using the strain and motion estimation, we will develop a spatio-temporal tensor-based linear classification method to detect and localize the regional abnormalities in myocardial function.

The above three specific aims make up a concrete framework. Strain analysis (Aim 3) depends on the results from the tag tracking (Aim 1), and boundary segmentation (Aim 2). Boundary segmentation (Aim 2) helps tracking algorithms (Aim 1) avoid errors that come from outside of the boundaries. See Figure 1.1 as an illustration of the framework.

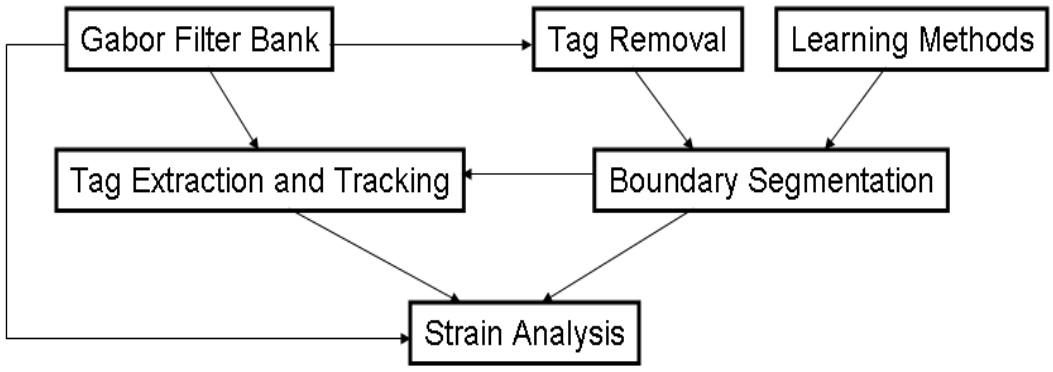

Figure 1.1: The framework of the whole dissertation.

1.3 Structure of dissertation

The structure of this dissertation is organized as follows: In chapter 2, we give the background knowledge of cardiac tagged MRI and literature review of image analysis methods in tMRI. In chapter 3, we present tag extraction and tracking methods. In chapter 4, tagging lines or grids removal methods are discussed. In chapter 5, we investigate the myocardial segmentation methods in tagged MRI. In chapter 6, myocardial strain estimation methods are provided. Finally in chapter 7, a conclusion and future

topics are presented.

Chapter 2

Background

2.1 Brief Introduction of Tagged MRI

Cardiac MRI tagging is a well-developed method for estimation of localized myocardial deformations. It was first introduced by Zerhouni [13] and Axel [14]. By spatial modulation of magnetization of the myocardium, this technique generates a set of equally spaced parallel planes or grids of saturated magnetization within the myocardium as temporary tags at end-diastole. Imaging planes are perpendicular to the tagging planes, so that the tags appear as parallel dark stripes in MRI images. The magnetization of the myocardium persists for a short period of time (on the order of the relaxation time) after the modulation, so that we observe the dark tag strips deform with the underlying myocardium during the cardiac cycle in vivo, which gives information on motion of the myocardium normal to the tagging stripes. Some example images can be seen in Figure 2.1.

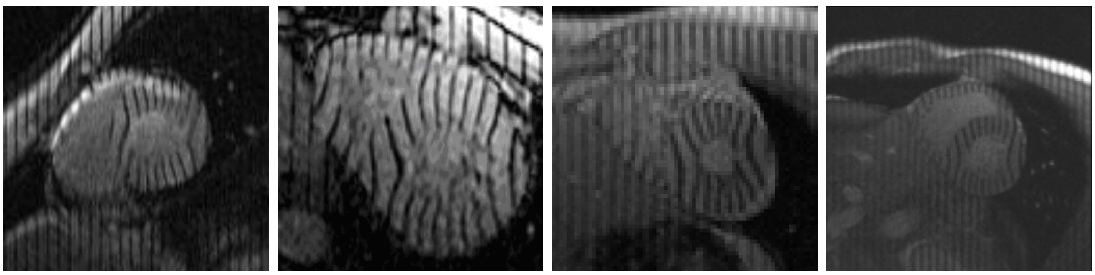

(a) (b) (c) (d)

Figure 2.1: Some examples of the tagged cardiac MRI images.

Part of the tagged MR images being processed in this dissertation are acquired using

the spatial modulation of magnetization (SPAMM) [14] technique, which uses non-selective excitation to produce saturated parallel planes throughout the entire imaging volume within a few milliseconds. One modification of this method to minimize the tag fading effect is the use of complementary SPAMM (CSPAMM) [15]. This technique acquires two tagged images with SPAMM patterns that are 180° out of phase with each other and subtracts them.

Tagged MR imaging techniques have been developing and improving throughout this dissertation work. Part of the tagged MR images used in this dissertation were acquired with single- and multiecho steady-state free precession (MESSFP) sequence [16, 17, 18]. This MESSFP imaging method achieves excellent contrast between the myocardium and the ventricular blood. See Fig. 2.1(c,d) for examples.

Most of the image processing and analysis algorithms in this dissertation are developed to work on various tagged MR techniques, such as the tag extraction and boundary segmentation methods. However, some of the algorithms are specifically designed for certain imaging settings. For example, the band-stop filtering based tag removal method works only on the MESSFP images. In the following chapters, we will discuss the algorithm's applicable imaging setting if it is not a generic method.

2.2 Related work

Since cardiac MRI tagging was invented one and a half decades ago, much effort has gone to the search for automated image processing and analysis methods for tagged MRI. In the following, we will give a brief review of the related work in areas of image preparation, tag segmentation and tracking, tag removal, myocardial boundary segmentation, and strain estimation.

2.2.1 Image Preparation

Intensity inhomogeneity is a common problem in MR images, which means different locations in the image have different intensity range. Several general methods have been developed to suppress the background intensity variation in MR images [19, 20, 21, 22,

23]. In [24, 25] Montillo et al., and Axel et al. developed two more specific methods for tagged MRI. In [24] a histogram modification method was specially adapted for tagged cardiac MRI based on the work in [26]. The author claimed that this method can help suppress the effects of tag fading as well.

2.2.2 Tag Segmentation and Tracking

The tagging lines fade over time because the myocardial tissue starts to lose its altered magnetization in less than 0.5 seconds. The major difficulty of tag tracking comes from the tag fading effect. Several researchers have developed tag enhancement or segmentation algorithms. Guttman et al. [27] extracted the tag using morphological operations. Young et al. [28] and Amini et al. [29] developed matched filters to segment the tag. Then tag tracking is performed on the tag extracted images. Dougherty et al. [30] have developed algorithms to suppress the tag fading effects. Prince and McVeigh [31, 32] proposed methods to model the tag fading portion of the variation based on MRI physics.

For tag tracking, tagging lines or grids are modeled as a set of 1D splines in [33] or 2D splines in [29]. Chandrashetara et al. [34] superimposed a 2D free-form-deformation (FFD) grid onto the tagged image, and used the approach of non-rigid registration to track the tagging grids. This method actually tracks the whole FFD region, rather than only the tagging grids. There are similar optical flow-based methods [35] that track the whole myocardial region.

Another group of tag tracking methods is based on the HARP technique [36, 37]. Rather than tracking the tag or myocardium, it operates in the spectral domain by tracking the phase angle of the tag pattern.

2.2.3 Tag Removal

To address the difficulty added by tagging lines, several researchers have proposed image preprocessing methods to remove or suppress the tagging lines. Based on the tagging line's lower intensity and narrow structure, Guttman et al. and Montillo et al. [27, 38] implemented gray-scale morphological operations to fill up the dark tagging

lines. Other researchers proposed spectral filtering-based approaches. In [36] Osman et al. developed a band-pass filtering method to enhance the tag-patterned region and increase the blood-to-myocardium contrast in the HARP framework. Manglik et al. [39] developed a Gabor filter bank-based method that is more adaptive to large local deformations.

2.2.4 Myocardial Boundary Segmentation

Myocardial boundary segmentation is an essential step in tagged MRI analysis. However, it remains a very difficult task due to the common presence of cluttered objects, complex object textures, image noise, intensity inhomogeneity, and especially the complexities added by the tagging lines.

As a result, many researchers [40, 41, 42, 43] didn't address this segmentation problem, just assuming the boundaries are known from manual input. Guttman et al. [27] developed a LV segmentation framework that is operated on the tag-removed image, using morphological operations. The segmentation is based on a dynamic programming framework. Later, Guttman [44] modified this segmentation into a watershed framework, still using the tag removal strategy. Montillo et al. [24] developed a bi-ventricular automated segmentation work, which is based on tag removal methods using grayscale morphological operations, and a 3D deformable model. The main disadvantage of morphological operations is that they are insensitive to the orientations and patterns of the tag structures, which may lead to filling up the interfaces between organs.

2.2.5 Strain Estimation

Strain estimation is the ultimate goal of tagged MR imaging. Many researchers have proposed 3D motion reconstruction approaches to calculate the strains. Park et al. [42] constructed a parametric superquadric model to estimate the detailed motion of LV, which is driven by the tag displacement using FEM. Declerck et al. [43] used a 3D B-spline model in modeling LV. Biventricular model has also been proposed in order to estimate the motion of both LV and RV. Haber et al. [41] developed a patient-specific FEM mesh to represent the ventricles. Park et al. [45, 46] proposed a superquadric

model that consists of three surface models and represents both LV and RV. Model (FEM) to estimate 3D ventricular deformation and strain. In this method, the cardiac boundary segmentation results are used to fit the generic FEM model into the real heart data. The tagging lines or grids are used as landmark points, which are registered to each FEM element. Then the tracking results of the tagging lines or grids are used to deform the FEM model. The 3D deformation and strain estimation can be obtained by solving the FEM, i.e., the model converging to the desired shape when the external forces diminish to zero and the residual motion is negligible. In [47, 48], cardiac stresses and fiber orientations are obtained from the strain estimations using an EM scheme.

For 2D strain calculation, tracking-based methods are commonly used to derive the myocardial strain. In [49], deformed tags are tracked and interpolated using a spline method to obtain the displacement map. Then the 2D Lagrangian strain is calculated from the horizontal and vertical displacement maps. HARP technique [36, 37] is also applied in strain estimation, where the tag is tracked implicitly by accumulating the phase changes in consecutive frames.

Chapter 3

Tag Extraction and Tracking

3.1 Image Preprocessing

3.1.1 Background

Intensity inhomogeneity is a common problem in MR images, which means different locations in the image have different intensity range. For example, as shown in Figure 3.1, the right top corner has much higher average intensity and contrast than the rest of the image. This inhomogeneity mainly comes from the non-uniform RF fields in MR imaging setting. Several general methods have been developed to suppress the intensity variation in MR images [19, 20, 21, 22, 23]. In [24, 25] more specific mthods for tagged MRI are developed. In [24] a histogram modification method was specially adapted for tagged cardiac MRI. The author claimed that this method can help suppress the effects of tag fading as well. We find that many of these methods are computationally demanding, e.g., in [21] their method requires about 1 minute for a 2D MR image. Since our data is fully 4D, which usually consists of more than 200 2D slices, these methods are computational infeasible.

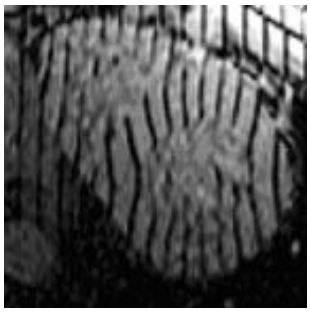

Figure 3.1: An example of intensity inhomogeneity in tagged cardiac MRI images.

3.1.2 Methodology

Here we adapted the simpler and faster inhomogeneity correction method in [25], whose results are not perfect but can greatly help the following tag segmentation and tracking.

For simplicity, we assume the MR image only consists of two layers: the foreground and the background. First the intensity values $I(x, y, z)$ of the input 4D image are linearly scaled to the range of $[0 - 127]$. Then its histogram H is calculated as:

$$H(i) = \sum_{x,y,z} h(x, y, z), \quad for \quad 0 \leq i \leq 127 \tag{3.1}$$

where,

$$h(x, y, z) = \begin{cases} 1, & when \quad i - 0.5 \leq I(x, y, z) < i + 0.5 \\ 0, & otherwise \end{cases} \tag{3.2}$$

As shown in Fig. 3.2, the bins around the first histogram peak i_p indicate the background intensities. From H's first derivative H', we find the first index i_0 such that $H'(i_0) > 0$ and $i_0 > i_p$ as the threshold value. For a voxel (x, y, z) in the MR image, if $I(x, y, z) > i_0$ then we classify it as a foreground voxel, otherwise we classify it as a background voxel.

For all the foreground voxels, we find their median intensity value M_f. Then we can construct a foreground image I_f by replacing all the intensity values of the background voxels by M_f:

$$I_f(x, y, z) = \begin{cases} M_f, & if \quad I(x, y, z) \in [0, i_0] \\ I(x, y, z), & otherwise \end{cases} \tag{3.3}$$

The foreground image I_f is blurred to I_b by convolving with a 4D Gaussian kernel, whose standard deviation σ in the $X - Y$ plane is empirically set to two times of the tagging line spacing in a single 2D slice. For example, for an image set with tag spacing equalling 10 pixels, we set $\sigma_{x,y} = 20$ pixels. In the Z direction, the standard deviation is set to

$$\sigma_z = \frac{\sigma_{x,y} \cdot R_z}{R_{x,y}} \tag{3.4}$$

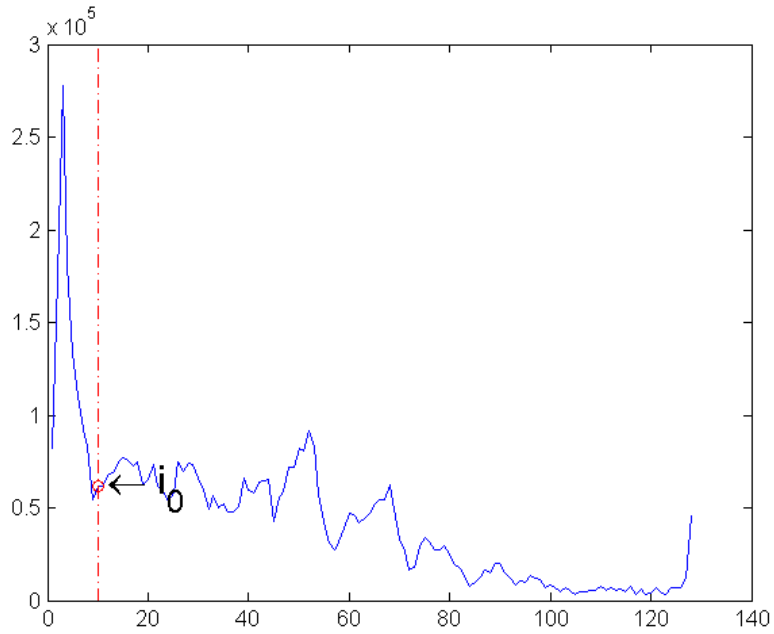

Figure 3.2: The histogram of the input 4D tagged MR image. i_0 is the intensity threshold to determine whether a voxel belongs to the foreground or the background.

where R is the spatial resolution in each coordinate. In the temporal direction, we empirically set $\sigma_t = \sigma_z$. Furthermore, the blurring process does not require a high resolution input. We down-sample the input 4D image in the $X - Y$ coordinates to achieve faster implementation. In experiments, we choose the down-sampling rate of 4 to 1. Then the inhomogeneity corrected image I_c is derived by normalizing the input I with the blurred foreground I_b:

$$I_c(x, y, z) = I(x, y, z)/I_b(x, y, z) \tag{3.5}$$

3.1.3 Experimental Results

We preprocess the tagged MRI as a routine before all the following image analysis procedures. As shown in Fig. 3.3, the intensity homogenized image has a better readability, and therefore is easier to process and analysis.

The computation of this MR image inhomogeneity correction method is fast. We implemented this method on a P4 2.8G Hz workstation using MatLab 6.5. For a

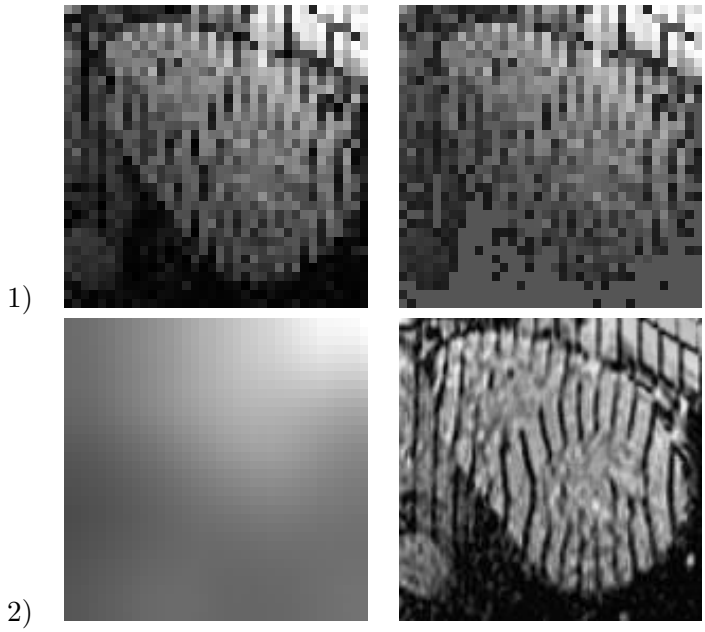

Figure 3.3: (1a) is the down-sampled 2D slice of a 4D input image set. The original image can be found in 3.1; (1b) is the foreground image I_f. (2a) is the Gaussian blurred foreground image; (2b) is the inhomogeneity corrected image I_b. Image (1a), (1b) and (2a) are down-sampled to achieve faster implementation.

$256 \times 256 \times 7 \times 20$-sized 4D image, it takes less than 10s.

3.1.4 Other Applications

Although the image analysis methods developed or implemented in this dissertation are mainly designed for the cardiac tMRI applications, many of them are generic methods, which are suitable for a large range of applications. We find that this intensity homogenization method is suitable for conventional MR images as well. For example, we applied this method in 3D abdominal MRI. The experimental settings are similar to the previous tMRI case, except for the standard deviation in the $X-Y$ plane, which is much larger in abdominal MRI than in cardiac tMRI. See an example of the intensity homogeneity correction of abdominal MRI in Fig. 3.4.

By observing the result in Fig. 3.4, we find that the image readability is much improved, especially in the top and bottom areas. The intensity of the colon lumen, including the rectal area, becomes more consistent. This will greatly help with region

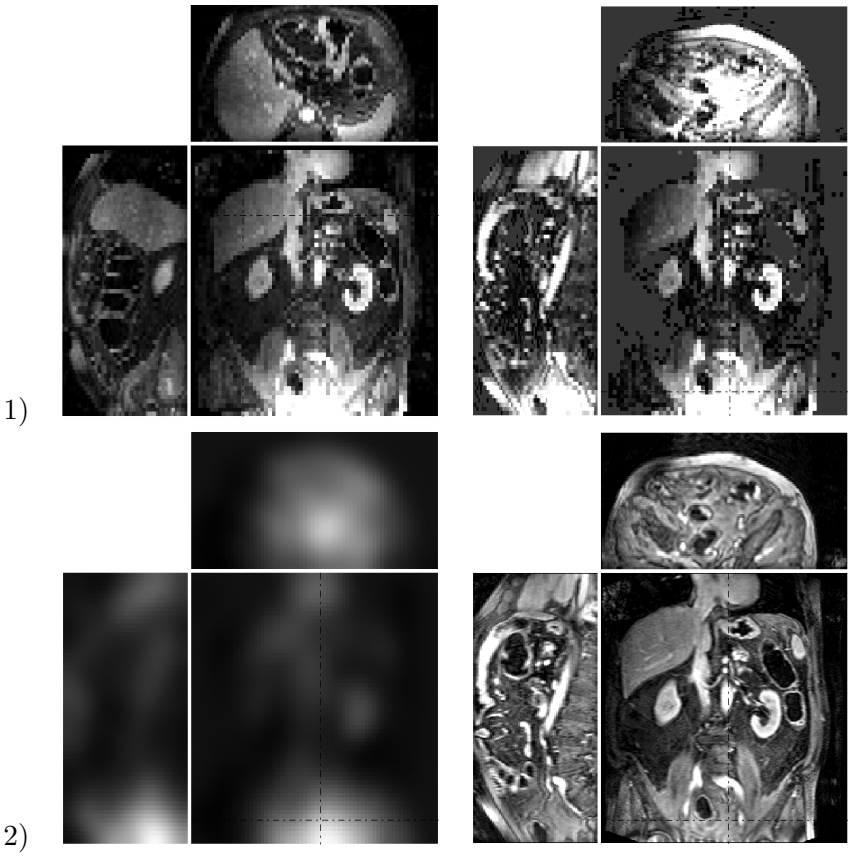

Figure 3.4: (1a) is the 3D view of a down-sampled 3D abdominal MRI set; (1b) is the 3D view of the foreground image I_f. (2a) is the 3D view of the Gaussian blurred foreground image; (2b) is the 3D view of the inhomogeneity corrected image I_b. Image (1a), (1b) and (2a) are down-sampled to achieve faster implementation.

intensity-based colon segmentation method.

3.2 2D Tagging Lines Enhancement and Tracking Using Gabor Filter Bank

3.2.1 Background

The tagging lines fade over time because the myocardial tissue starts to lose its altered magnetization in less than 0.5 seconds. The effects of tag fading lead to blurred image edges and valleys. When we try to track the tagging lines in tag faded images, this may cause tagging lines mis-tracking. Therefore, we need a method to enhance the tagging lines and suppress the fading effects, so as to facilitate the tracking process. At the same time, it is desirable to automate this enhancement procedure and segment the tagging lines.

There have been many methods developed for the tag extraction and motion extraction problem. For example, HARP [50], which was developed in John Hopkins University, is a technique that has been developed for rapid motion analysis of tagged MR images. It generates phase angle images that roughly resemble the original tag pattern. Tagged MR images have a regular tagging lines pattern, which leads to relatively isolated peaks in their spectral domain. HARP is basically a bandpass filter that selectively filters those isolated spectral peaks. Although it provides a good avenue towards the automated tagging line segmentation, HARP has its limitations. Even with the addition of a Gaussian roll-off outside [51], HARP's bandpass filter is still a global transform in the spatial domain (as shown in Figure 3.5), i.e., HARP's spatial local transform is affected by regions far away. Also it is not obvious how to automatically design a bandpass filter that can simultaneously achieve good resolution in both the spatial and the frequency domains. When the first harmonic peak is not well concentrated, HARP has to increase the bandwidth of its bandpass filter. In this case, if the tagging lines deform a lot locally, it would not be robust to use such a wide bandpass filter, which cannot treat regions with and without tag deformations differently. Due to the phase-wrapping artifact [50], HARP is not suitable when large local deformations

occur. Another limitation of HARP is that the synthetic tag lines obtained from the phase angle are only an approximation to a tag line. Therefore it cannot represent the exact tagging line shape, thickness and deformation.

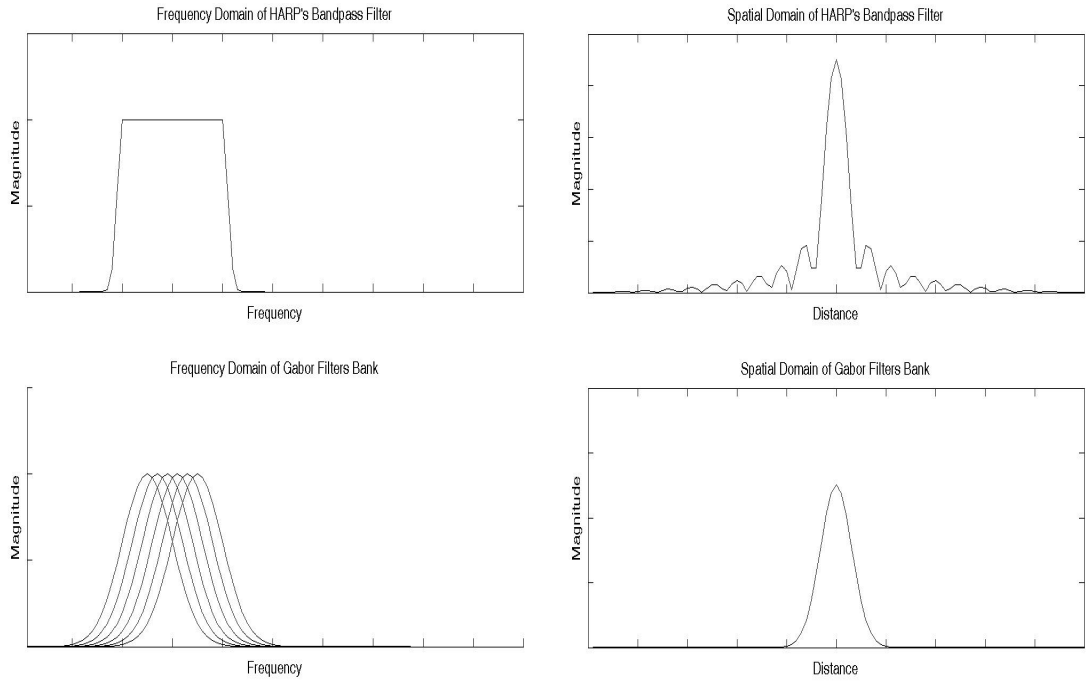

Figure 3.5: Simplified 1D model of HARP and Gabor filters in frequency domain (left) and spatial domain (right). Upper is HARP; lower is Gabor filter bank. A Gabor filter bank uses the combination of a group of Gabor filters to selectively cover the whole bandpass frequency range; each single filter can still get full constraints in its spatial domain, but HARP cannot.

3.2.2 Methodology

Instead of HARP, we developed a method for the segmentation and extraction of tagging lines based on 2D Gabor filters. Gabor filters have been widely used in image processing applications, such as texture segmentation [52, 53, 54] and edge detection [55]. A main advantage of Gabor filters, due to their Gaussian envelopes, is that they always achieve the minimum space-bandwidth product which is specified in the uncertainty principle [52]. This advantage helps Gabor filters to get full constraints in their spatial domains (as shown in Figure 3.5) as well as in their frequency domain. However, a

bandpass method like HARP cannot achieve this. Therefore Gabor filters are wavelet-like local filters in the spatial domain, which makes it possible to design adaptive filters with respect to different spatial patterns of different local regions. In this chapter we design a bank of Gabor filters with different frequencies, directions and shapes that are specified according to the tagging lines' pattern in the input image. We then convolve each Gabor filter in the filter bank with the input image, and derive our results by seeking the optimum filter for those pixels whose output is greater than a certain threshold. Therefore, our result is a combination of those outputs from several Gabor filters (as shown in the lower-left part in Figure 3.5). Our Gabor filter-based algorithm is adaptive because we specify the frequencies of interest locally, rather than using a mixture of arbitrary frequencies as in HARP.

Basic definitions

The 2D Gabor filter was first introduced by Daugman [56]. It is basically a 2D Gaussian multiplied by a complex 2D sinusoid [52], as shown below:

$$h(x,y) = g(x',y')s(x,y) \tag{3.6}$$

where $g(x',y')$ is a 2D Gaussian, and $s(x,y)$ is a complex 2D sinusoid function, i.e.,

$$g(x',y') = \frac{1}{2\pi\sigma_{x'}\sigma_{y'}} e^{-\frac{1}{2}[(\frac{x'}{\sigma_{x'}})^2+(\frac{y'}{\sigma_{y'}})^2]} \tag{3.7}$$

$$s(x,y) = \exp[-j2\pi(Ux+Vy)] \tag{3.8}$$

In Equation 3.7,

$$x' = xcos\theta + ysin\theta, y' = -xsin\theta + ycos\theta \tag{3.9}$$

are the spatial coordinates, which are rotated by an angle θ, and σ_x, σ_y gives the approximate spatial extent of the 2D Gaussian. The 2D Gaussian envelope need not be symmetric, i.e., σ_x and σ_y need not be equal. In Equation 3.8, (U,V) are the 2D

frequencies of the complex sinusoid, and its orientation is given by:

$$\phi = \arctan(V/U) \tag{3.10}$$

The Fourier transform $H(u, v)$ of $h(x, y)$ is given by:

$$H(u, v) = e^{-2\pi^2[(\sigma_x(u-U)')^2+(\sigma_y(v-V)')^2]} \tag{3.11}$$

Obviously, $H(u, v)$ is also a Gaussian whose center frequencies are (U, V) , and its frequency extent is determined by σ_x and σ_y. Thus, $H(u, v)$ actually works as a bandpass filter. If we simplify our model to a symmetric Gaussian envelope, then $\sigma_x = \sigma_y = \sigma$, and from Equation 3.11, we can get $H(u, v)$'s Gaussian standard deviation σ_H as $\sigma_H = 1/(2\pi\sigma_h)$. Thus:

$$\sigma_h \cdot \sigma_H = 1/2\pi \tag{3.12}$$

Therefore, the product of spatial resolution and frequency bandwidth achieves a minimum constant. This is why Gabor filters can simultaneously achieve optimal resolutions in both the spatial and the spatial-frequency domains [52]. This makes Gabor filters work better than HARP.

Gabor Filter Bank Design for Tagging Line Extraction

We use an ellipse-like 2D Gaussian envelope in our case (as shown in Figure 3.6), which is more adaptable to the complicated geometries of cardiac tissues. We define the σ's of the 2D Gaussian as follows:

$$\sigma_x = \frac{1}{\sqrt{(U^2 + V^2)}} \tag{3.13}$$

$$\sigma_y = \frac{1}{\sqrt{(U^2 + V^2)}} \cdot \frac{1}{4} \tag{3.14}$$

where (U, V) are the frequencies of the first harmonic of the Fourier transformed image. We obtain the (U, V) automatically by finding the coordinates of the first harmonic peaks in the spectral domain [51]. (As seen in Fig. 3.7)

The orientation angle θ of the Gaussian envelope is set equal to ϕ, as was specified in Equation 3.10.

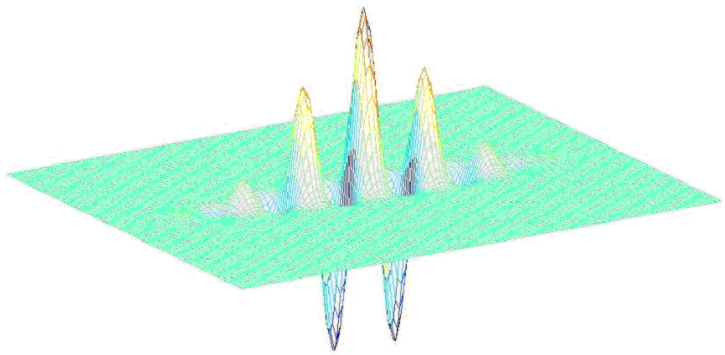

Figure 3.6: Real part of a Gabor filter in the spatial domain.

With all the parameters specified above, we could set up a Gabor filter based on Equation 3.6. Then we modifyparameters θ, U and V to generate a group of different Gabor filters based on the deformed tagging line pattern of the input image. The modified new θ' is set by $\theta' = \theta + \Delta\theta$, where $\Delta\theta$ varies from -30° to 30° to match different regions in the cardiac MRI (as shown in Fig. 3.8).

Because the images are acquired during a heart beat cycle, the spacings and orientations of the tagging lines change along with the underlying myocardium, and may no longer be parallel, as shown in Figure 3.1. These changes in the spatial domain lead to the corresponding changes in the frequency domain. The new U' and V' are specified as follows:

$$U' = \Re\{(U + i \cdot V) \cdot m \cdot \exp(i \cdot \Delta\phi)\} \tag{3.15}$$

$$V' = \Im\{(U + i \cdot V) \cdot m \cdot \exp(i \cdot \Delta\phi)\} \tag{3.16}$$

where m and $\Delta\phi$ are the magnitude and angle modulations respectively. We modulate m corresponding to the changes of tag spacings, and modulate $\Delta\phi$ corresponding to the changes of the tag lines' direction. For example, in Figure 3.1, we set m to the range of $[0.9, 1.2]$, because during systole, most tag lines get closer to each other in their

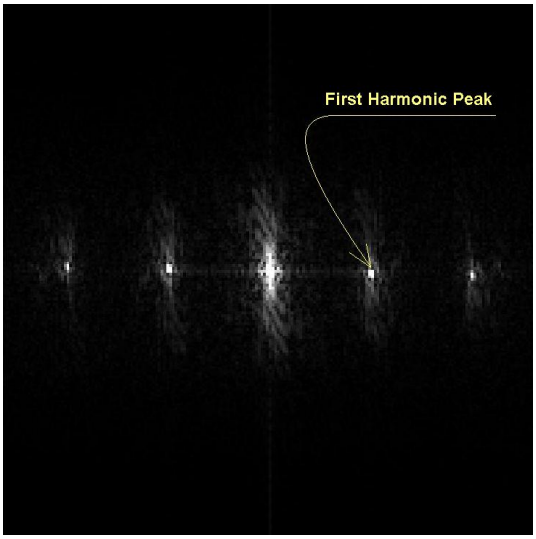

Figure 3.7: The indicated pixel is the first harmonic peak of the tagged image in the Fourier domain. By finding the location of this peak, (U, V) can be determined by its coordinates.

middle regions and farther in the two ends. And we set $\Delta\phi$ to vary from $-10°$ to $10°$ by our observation of the tag lines orientation changes. Gabor filters whose $\theta' \cdot \Delta\phi < 0$ are excluded, because they cannot cover enough tagging lines, and may generate errors.

As shown in Equation 3.6, a Gabor filter is a Gaussian modulated by a sinusoid. We find a sinusoidal modulation of the Gaussian would only be desirable for finding a sinusoidal tag pattern. However, real tagging lines are not exactly sinusoidal. As shown in Figure 3.1, the tagging lines are usually thinner than the spacing in between. This is also why there are second, third, or more harmonics in the frequency domain. We can modify the shape of the sinusoid by adding some higher harmonic components to it. Thus $s(x, y)$ is modified to:

$$s'(x,y) = \begin{cases} \frac{1}{p} e^{\frac{-j\pi(Ux+Vy)(1+p)}{p}}, & \frac{1}{4\pi(1+p)} < |Ux+Vy| \leq \frac{2p+1}{4\pi(1+p)} \\ e^{-j\pi(Ux+Vy)(1+p)}, & \frac{1}{4\pi(1+p)} \geq |Ux+Vy| \end{cases} \tag{3.17}$$

and $s'(x, y)$ is periodic with respect to $Ux + Vy$, whose period is $1/2\pi$.

We use p to control the sinusoid modification. p is the ratio of the sinusoid's negative

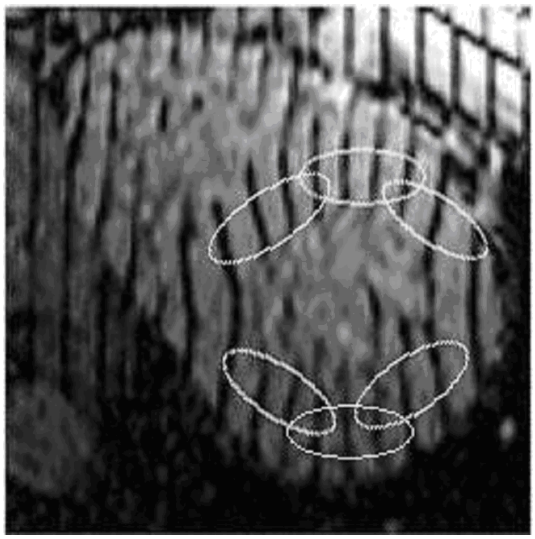

Figure 3.8: Different θ fits different cardiac region.

domain to the positive domain. We set p based on the tagging patterns: p experimentally equals two times the ratio of the tag spacing to the tag thickness. Therefore, with respect to Figure 3.1, we approximately set p to 3.

Normalization

The optimal thresholds for different Gabor filters vary. To determine the threshold of a certain Gabor filter, we must first do a normalization.

We assume that using different Gabor filters, the total number of pixels within the tag lines is a constant. First, the total number T of the pixels in the tag lines is estimated in a manual initialization step. Then, using different Gabor filters, for each filter, we pick out the $\alpha \cdot T$ number of pixels with the highest values. Experimentally we set $\alpha = 90\%$. The final result is a combination of all the results from each Gabor filter.

3.2.3 Experimental Results

Figure 3.10(a) shows three short-axis cardiac MRI images during systole. Figure 3.10(b) shows the segmentation results using our method, where we set $-30^\circ \leq \Delta\theta \leq 30^\circ$,

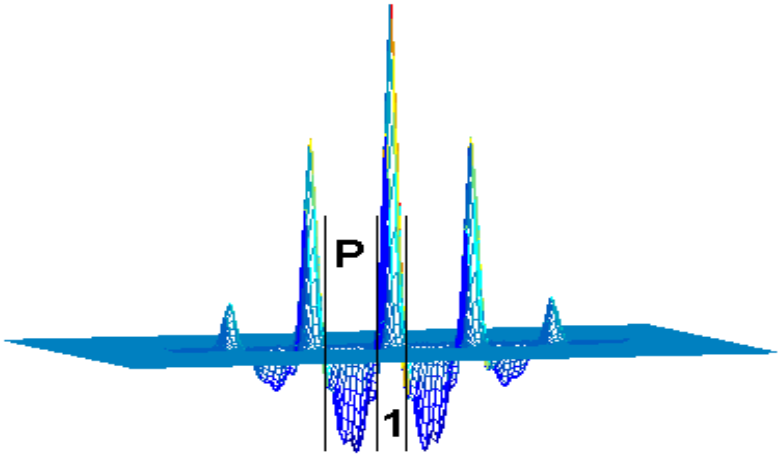

Figure 3.9: A shape modified Gabor filter with $p = 3$ that has a more similar appearance with the tagging line.

$\alpha = 90\%$, $p = 3$, and in (a1), $0.9 \leq m \leq 1.1$, $-10° \leq \Delta\phi \leq 10°$; in (a2), $0.9 \leq m \leq 1.2$, $-10° \leq \Delta\phi \leq 10°$; in (a3), $0.9 \leq m \leq 1.2$, $-10° \leq \Delta\phi \leq 10°$, based on the input images' tag patterns as described in section 3.2.2. This setting is easy and straightforward. The directions, spacing, thickness, and shape of the resulting tag lines fit those in the input image quite well. Figure 3.10(c) shows the results of HARP. The myocardium contours are added manually for better readability. HARP's results are obtained by the method described in [51]. Here we find that our result is visually better than that of HARP. The Gabor filter bank method can achieve higher resolution, and is more robust for large local deformations compared to HARP.

3.2.4 Tagging Lines Tracking

The purpose of the tag enhancement and segmentation is to facilitate tagging lines tracking. To avoid effects from the tag patterns off the myocardium, the tagging lines need to be tracked only within the heart wall. In Chapter 5, we will discuss the details of myocardial boundary segmentation. Here we assume that the images are segmented.

The tagging lines are modeled as a set of free-end 2D deformable models, *Snakes* [57]. Each *Snake* is represented by a set of ordered nodes:

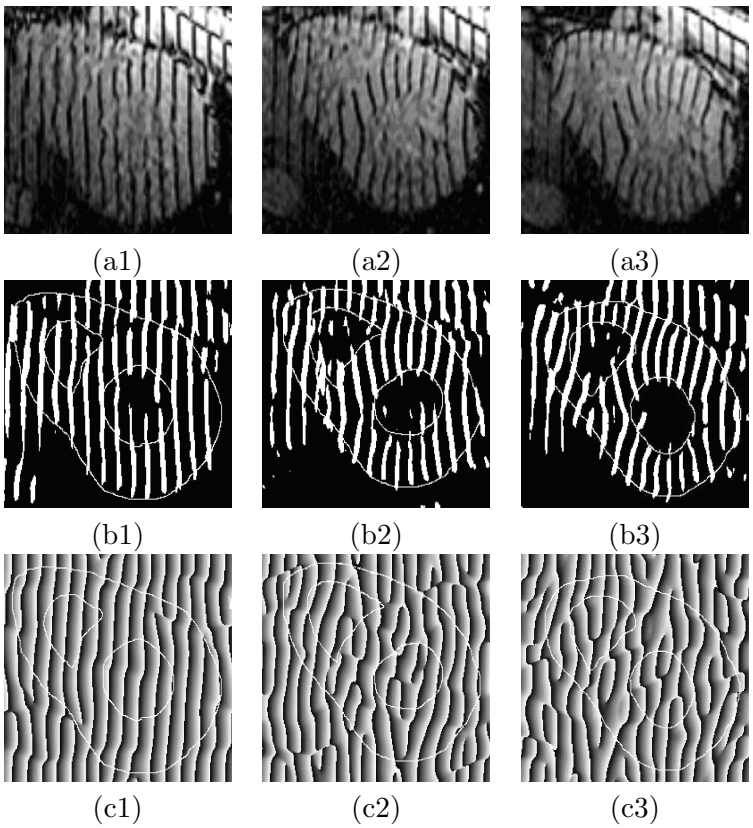

Figure 3.10: (a) Three tagged cardiac MR images in short axis. They are taken from an MRI sequence during systole. (b) The output results of our method. (c) HARP's phase angle result. The myocardium contours are drawn manually for better readability.

$$v(s) = (x(s), y(s))^T \tag{3.18}$$

where x and y are the coordinate functions and $s \in [0, 1]$ is the parametric domain.

As shown in Fig. 3.11, for images with horizontal tagging lines, we initialize the *Snakes* as a set of horizontal straight lines that are parallel and equally spaced with an interval of $1/\sqrt{(U^2 + V^2)}$, which is the initial spacing between the tagging lines. Although we only need to track the tagging lines within the myocardium contours, we add more *Snakes* outside the heart region. This is because the heart undergoes a 3D motion. Myocardial tissues (including the tagged tissues) may move in or out of the imaging plane. The extra *Snakes* serve as candidates. When new tagging lines appear in the myocardium, they can move into the myocardial area and start to track the

newly appeared tagging lines.

In order to find the initial position of the *Snake* set, in vertical direction, we move the set of *Snakes* up and down in a range of $1/2\sqrt{(U^2+V^2)}$, and calculate the mean of the pixel intensity values at the locations of the *Snakes*' nodes that are on the myocardium. We search for a minimum intensity mean to find the initial position in the vertical direction of the horizontal *Snake* set.

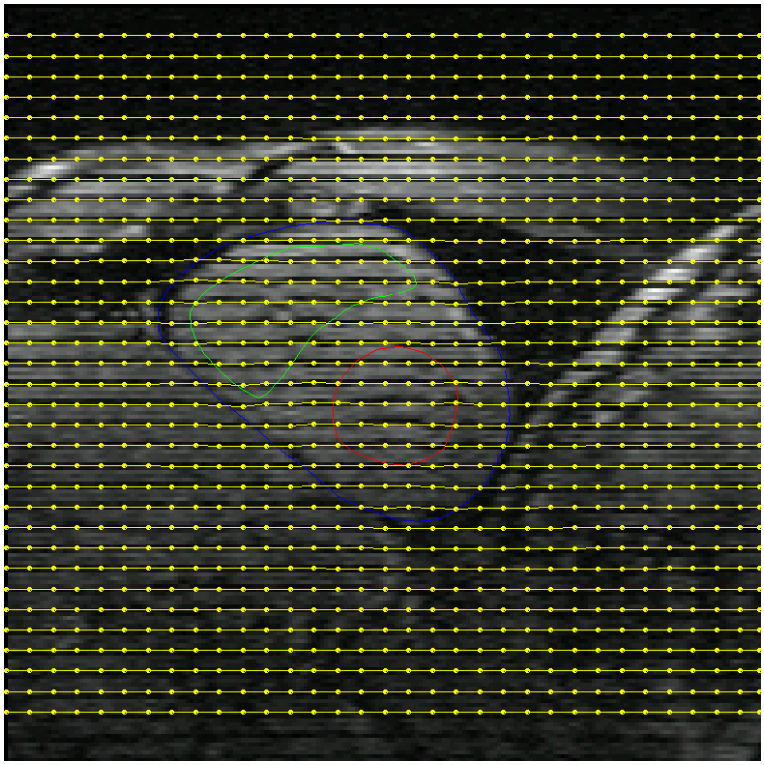

Figure 3.11: Initialization of the Snake set.

Starting from time 0, we track the tagging lines by deforming the *Snakes* to find the local maxima in the local vertical (in case of horizontal tagging lines) or horizontal (in case of vertical tagging lines) profiles at the *Snakes*' nodes in the tag enhanced images, and at the same time preserve certain geometrical constraints. Therefore, the external forces of *Snakes* push the *Snakes* nodes towards the high intensity pixels in the tag-enhanced images. The internal forces of *Snakes* are used to regulate the curvatures within each single Snake, and the distances between Snakes. The deformation of the *Snakes* can be formulated as process of energy minimization:

$$E(v) = E_i(v) + E_e(v) \tag{3.19}$$

As seen in Fig. 3.12, besides the conventional internal energy terms of *Snakes*, we add spring forces in between the neighboring *Snakes* to control their spacings. We define spacing change as Δd. Therefore, E_i can be formulated as:

$$E_i(v) = \int_0^1 (\alpha|\frac{\partial V}{\partial s}|^2 + \beta|\frac{\partial^2 V}{\partial s^2}|^2 + \gamma(\Delta d)^2)ds \tag{3.20}$$

At the same time, tracking is done only *within the myocardial contours*, which are obtained from boundary segmentation. As seen in Fig. 3.12, we have two kinds of nodes of the *Snakes*. Nodes on the myocardium are active, which means they get external forces from the underlying tag-enhanced image, and pull the rest of the nodes to move. Their motion is regulated by internal forces, which are only from active nodes themselves. Nodes off the myocardium are passive, which means they are pulled by the active nodes. Their motion is regulated by internal forces from both active and passive nodes. When tagging lines move in or out of the imaging plane, the nodes' labels of active or passive are inter-changeable.

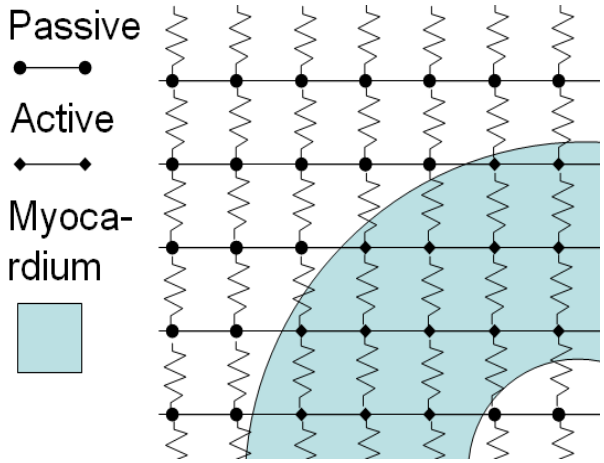

Figure 3.12: The model of our tagging lines tracking *Snakes*.

Tracking Results

The tracking process is limited by the fading effect of the tagging lines. Using different imaging settings, the trackable frame number varies. In a typical tMRI data set, we track the tagging lines from end-diastole to end-systole. In Fig. 3.13, we show one intermediate and one end-systolic tracking results. Manual correcting is optional during the tracking process, since in some local areas mis-tracking may occur.

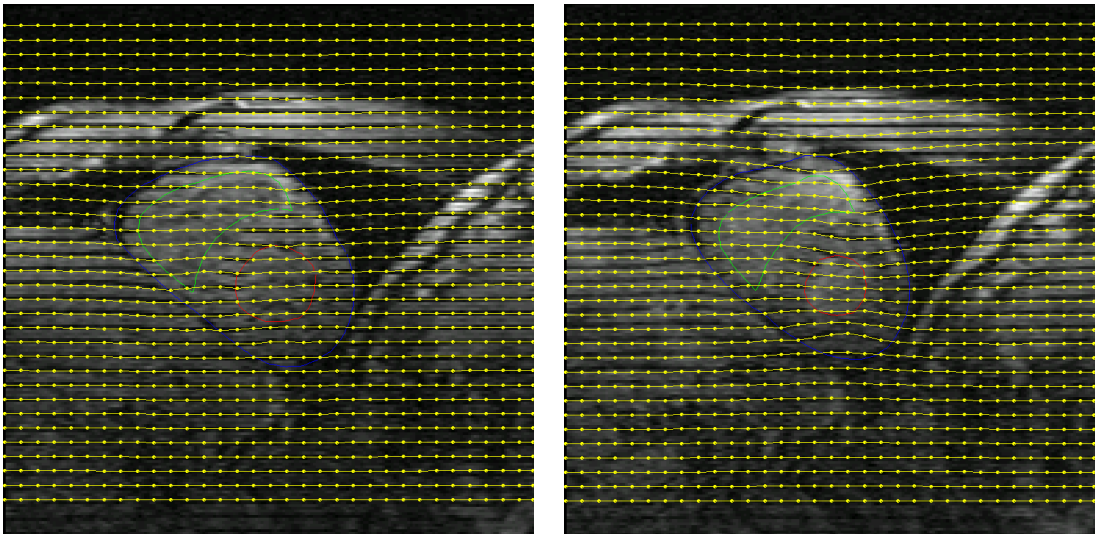

Figure 3.13: Tracking results at phases of mid-systole (lhs) and end-systole (rhs).

3.3 3D Gabor Extension and 3D Tagging Sheets Tracking

3.3.1 Background

In order to examine the function of the complete ventricle, i.e., from the ventricular base to the ventricular apex, 3D (spatially) tagged MR imaging is usually performed. For example, 3D tMRIs in the short axis (SA) are actually a stack of 2D SA cine slices taken at different positions along the central axis of the left ventricle. The imaging process in each position is gated by the ECG signals, so that the whole ventricle is imaged synchronously throughout a cardiac cycle. As stated in Chapter 2, tMRI generates a set of parallel saturated tagging planes within the myocardium as material markers at

end-diastole by spatial modulation of magnetization. As shown in Fig. 3.14, the imaging planes are perpendicular to the tagging planes, so that the tagging planes appear as a set of parallel dark stripes in the MR images and deform with the underlying myocardium. Intuitively, in order to segment or track the stripes in a 2D slice, the information of the corresponding stripes in their neighboring slices could be helpful, especially when the stripes in the current slice are unclear or corrupted.

Therefore, the 2D filtering approach in the previous section has limitations. It tracks the tagging lines' displacement only in a single spatial slice, and loses all the information from the neighboring slices.

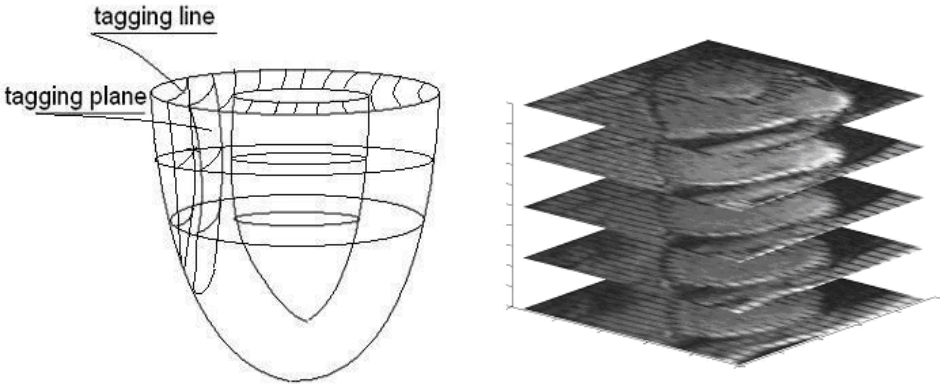

(a) (b)

Figure 3.14: (a) shows tagging lines are intersections of the tagging sheets and the imaging planes. (b) shows a 3D tagged MR image dataset.

Observation of the 3D tagging sheets' deformation could be more valuable in heart wall motion modeling and analysis. However, because of the motion of heart wall, the initial tagging planes are no longer true planes but turn to curved, bent or even twisted tagging sheets. Finding the tagging lines' correspondence across the imaging slices, i.e., which set of tagging lines belong to the same tagging sheet, is essential to recovering the deformed tagging sheets. A 3D tracking approach is necessary in finding this tagging line correspondence.

3.3.2 Methodology

We extend our 2D Gabor filter bank method to employ a 3D Gabor filter bank, in order to extract and track the deformed tagging sheets. The filter's scale, orientation, and shape are specified according to the geometric pattern of the tagging sheets. We convolve the 3D Gabor filter bank with the 3D tagged MRI data, which are in a time sequence. For each set of the 3D data, we extract the tagging sheets by combining the strong outputs from the filter bank at each voxel. Then we impose a deformable 3D mesh onto each of the tagging sheets to capture the tagging sheet deformation.

Basic Definitions: 3-D Gabor filter

We extend the 2D Gabor to 3D as following.

$$h(x, y, z) = g(x', y', z') \cdot s(x, y, z) \tag{3.21}$$

where $g(x', y', z')$ is a 3-D Gaussian envelope, and $s(x, y, z)$ is a complex sinusoid function, i.e.,

$$g(x', y', z') = \frac{1}{(2\pi)^{\frac{3}{2}}\sigma_{x'}\sigma_{y'}\sigma_{z'}} e^{-\frac{1}{2}[(\frac{x'}{\sigma_{x'}})^2+(\frac{y'}{\sigma_{y'}})^2+(\frac{z'}{\sigma_{z'}})^2]} \tag{3.22}$$

$$s(x, y, z) = \exp[-j2\pi(Ux + Vy + Wz)] \tag{3.23}$$

In Equation 3.22: $(x', y', z')^T = R \times (x, y, z)^T$ are the rotated spatial coordinates of the Gaussian envelope. R is a rotation matrix. Note that $\sigma_{x'}$, $\sigma_{y'}$ and $\sigma_{z'}$ need not be the same. Thus the shape of this Gaussian envelope can be an ellipsoid. In Equation 3.23, (x, y, z) is non-rotated spatial coordinates, which means the Gaussian envelope and the sinusoid could have different orientations. However, for normalization purposes, we set these two coordinates to the same value. (U, V, W) are the 3D frequencies of the complex sinusoid. They determine a Gabor filter's orientation and spacing in the spatial domain. As shown in Fig 2, a 3D Gabor filter has sets of iso-surfaces such that all those voxels on the same iso-surface have a constant value, for instance, in

Fig. 3.15(a), all the same colored voxels are on a same set of iso-surfaces; in Fig. 3.15(b), one set of the iso-surfaces is drawn as the yellow pancakes. The parallel iso-surfaces are geometrically similar with the 3D MR tagging sheets in the local regions. This makes it suitable for extraction and segmentation of tagging sheets. The normal of these iso-surfaces is a constant and set by:

$$\vec{N}_{isosurface} = (U, V, W) \tag{3.24}$$

At the same time, the spacing between two neighboring iso-surfaces is also a constant and set by:

$$S_{isosurface} = \frac{1}{\sqrt{U^2 + V^2 + W^2}} \tag{3.25}$$

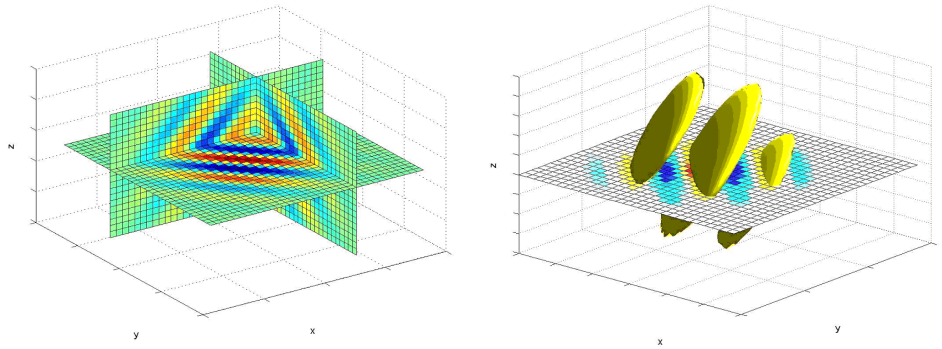

(a) (b)

Figure 3.15: (a) A slice view of a 3D Gabor filter. (b) An iso-surface view of a 3D Gabor filter. Here $\sigma_{x'} = \sigma_{y'} = \sigma_{z'}$, which makes the Gaussian envelope symmetric and the iso-surfaces in (b) circle-shaped; the normal of these iso-surfaces are (1,1,1), because $U = V = W$.

3D Gabor filters design

Tagging sheets are initialized and appear as a set of parallel and equally spaced dark planes in the myocardium at the end of diastole. During systole, tagging sheets deform with the underlying heart tissue so that the spacing and orientation of these tag sheets change over time. For short axis (SA) view, for instance, see Figure 3.16(a), a tag sheet T is initially perpendicular to the imaging plane I. For T, there are three possible

rotation angles, ϕ, ψ, and φ with respect to the three rotation axes. φ is the rotation angle w.r.t. the axis that is perpendicular to the tagging sheets. Thus φ measures the in-tagging-sheet rotation, which is not observable from the motion of the tagging sheet. So for SA images, we only consider the other two possible rotation angles: ϕ is the rotation angle w.r.t. the z axis, and ψ is for the rotation w.r.t. the intersection line of the tagging sheet and the imaging plane.

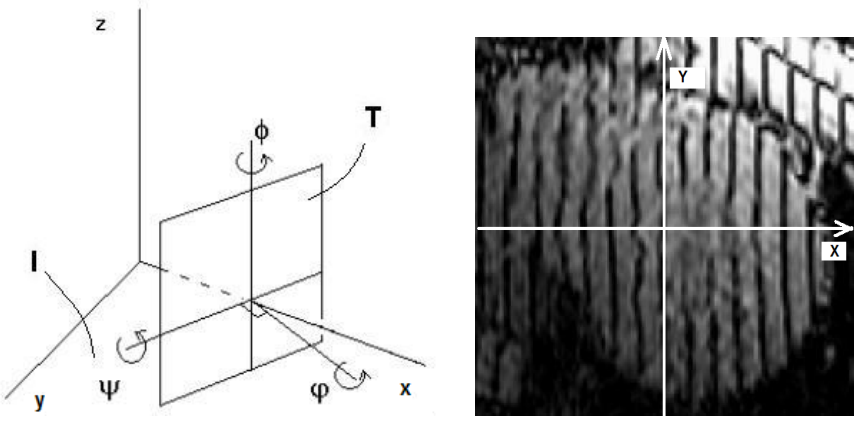

(a) (b)

Figure 3.16: (a) Tagging sheet's rotation has three possible orientations. But only ϕ, ψ are observable. The in-plane rotation φ is ignored. (b) The y axis is set to be parallel to the initial tagging lines.

Since the initial tagging planes are perpendicular to the imaging planes, we set the $x-y$ plane parallel to the imaging planes, i.e., the 2D image slices. In the $x-y$ coordinates, we rotate the 2D image so that the y axis is parallel to the initial tagging lines. See Figure 3.16(b).

In Equation 3.23, the Gabor sinusoid is specified by (U, V, W). However, when we design the Gabor filter to extract the tagging sheets, we are more interested in certain meaningful parameters, such as the spacing S between the tagging sheets, and the sheets' observable orientations ϕ and ψ. From Equation 3.24 and 3.25, we are able to use S, ϕ, and ψ to represent (U, V, W):

$$V = \frac{S}{\sqrt{(1+\tan^2(\phi)) \cdot (1+\tan^2(\psi))}} \tag{3.26}$$

$$U = V \cdot \tan(\phi) \tag{3.27}$$

$$W = \tan(\psi) \cdot \sqrt{U^2 + V^2} \tag{3.28}$$

In Equation 3.22, we use an ellipsoid-shaped 3D Gaussian envelope, which is more adaptable to the myocardial geometries and the tag patterns. The long axis of the 3D Gaussian is set to be the same as the x axis so that it can cover more tag patterns. We empirically define the σ's in Equation 3.22 as follows.

$$\sigma_x = \frac{1}{S}, \sigma_y = \frac{1}{4S}, \sigma_z = \frac{1}{4S} \tag{3.29}$$

The rotation matrix of the Gaussian envelope is given by:

$$\begin{aligned} R &= R_z \times R_{xy} \\ &= \begin{bmatrix} 1 & 0 & 0 \\ 0 & cos(\phi) & -sin(\phi) \\ 0 & sin(\phi) & cos(\phi) \end{bmatrix} \times \begin{bmatrix} cos(\psi) & -sin(\psi) & 0 \\ sin(\psi) & cos(\psi) & 0 \\ 0 & 0 & 1 \end{bmatrix} \end{aligned} \tag{3.30}$$

This rotation step is to make the Gaussian envelope have the same orientation as the complex sinusoid, which is important for normalization purposes.

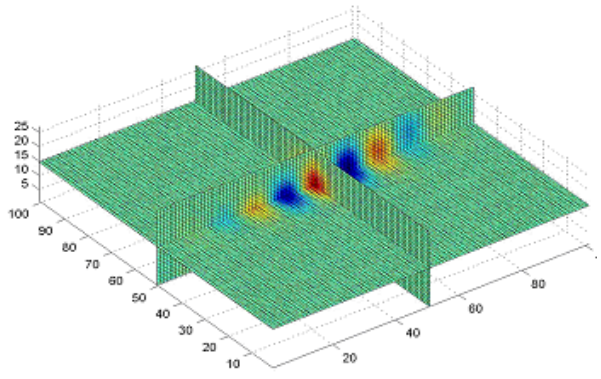

Figure 3.17: A Slice view of a 3D Gabor Filter used in our experiment.

Interpolation and Parameter Tuning

Usually, the 3D MRI data have different sampling rates in each coordinate. For instance, in one data set that we used, in the x and y coordinates, the pixel size equals 1.3 mm, while in the z coordinate, the spacing between two neighboring slices is 5.2 mm. This means the in-plane sampling rate is about 3 times higher than the inter-plane rate. To solve this discrepancy, we consider our 3D image as a 3D volume that is contracted by 4 times in the z direction. Thus contraction in the spatial domain will lead to an expansion in the Fourier domain. We set the new $W' = W \times 4$, which represents that the frequency in z direction is expanded by 4 times. At the same time, the Gaussian envelope is also contracted in the z direction. We set the new $\sigma'_z = \sigma_z/4$ and the new $\psi' = arctan(\tan(\psi) \times 4)$, which is the new rotation angle for the Gaussian. See Figure 3.17 for an example of the Gabor filter in this case.

The tunable parameters of the 3D Gabor filter bank are ϕ, ψ and S. The initial ϕ_0 and S_0 are obtained by solving the inverse of the Equations 3.26 and 3.27. The (U, V) are obtained by finding the frequencies of the fundamental harmonic of a 2D image slice at the beginning of the systole from the 3D dataset [58]. The initial ψ_0 is set to zero, since the initial tagging sheets are perpendicular to the imaging plane. In our experiments, we modulate the parameters ϕ, ψ and S based on the possible deformations of the myocardium. For example, the spacing between two tagging sheets may likely increase to up to double width or decrease to half width during myocardial deformation, thus we tune S so that $S_0/2 \leq S \leq 2S_0$. The bank of Gabor filters is made up of a sample of all possible filters whose parameters are in the tuning range.

3.3.3 Experimental Results

We tried our method on four 4D datasets, whose resolution are 96x96x18 pixels and consist of 6 time sequences, i.e., each dataset contains 108 2D images. All our experiments were coded in Matlab on a P4 1.5GHz desktop computer. The analysis of each dataset took approximately 15mins. Figure 3.18(a) shows an extraction result at time

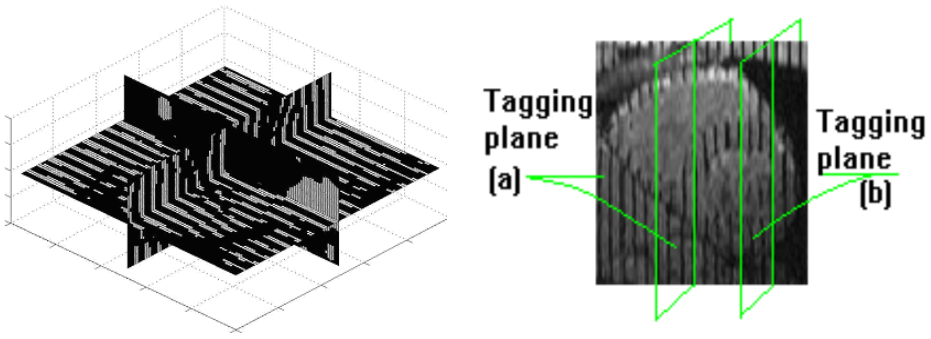

(a) (b)

Figure 3.18: a) A slice view of the 3D Segmentation result. b) The two tagging sheets that are tracked along time sequences. Tracking results of the sheets are shown in Fig 3.20.

6. This result is a combination of all the responses of the Gabor filter bank. The combination and normalization method is as follows: we assume that using Gabor filters, the total number of voxels within the tag sheets is a constant. First, this total number is estimated in an initialization step. Then using different Gabor filters, we pick out for each filter the 90% number of pixels with the highest values. The final result is a combination of all the results from each Gabor filter. As shown in Figure 3.18(a) it is a binary image cube where the extracted tagging sheets have the value of one and the else places are zero.

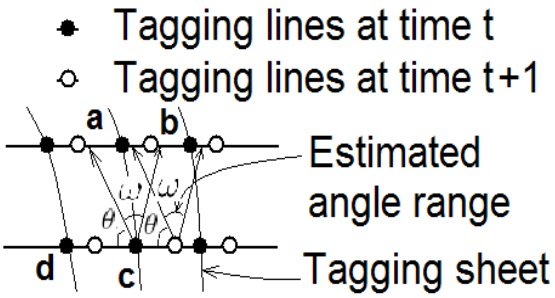

Figure 3.19: The rotation angle ψ at time $t+1$ is constrained by the angle ω and θ at time t, which prevents tagging sheets aliasing.

The binary image does not give the tagging lines' correspondences across the image slices. In the tracking step, we impose a set of deformable meshes onto the initial

tagging planes and let them deform according to the extracted tagging sheet results over time. The above binary image cube gives the possible locations where the tagging sheets may move to. As in Figure 3.19, the range of ψ at time $t+1$ is constrained by the angles ω and θ, which equal $\angle acb$ and $\angle acd$, where a and b are the middle points between the current tagging line and its neighboring tagging lines in the same image slice at time t, c is the neighboring tagging line which is in the same tagging sheet as the current tagging line at time t, and d is the left hand side tagging lines on the neighboring slice. The deformable mesh is also smoothed with an internal spring force.

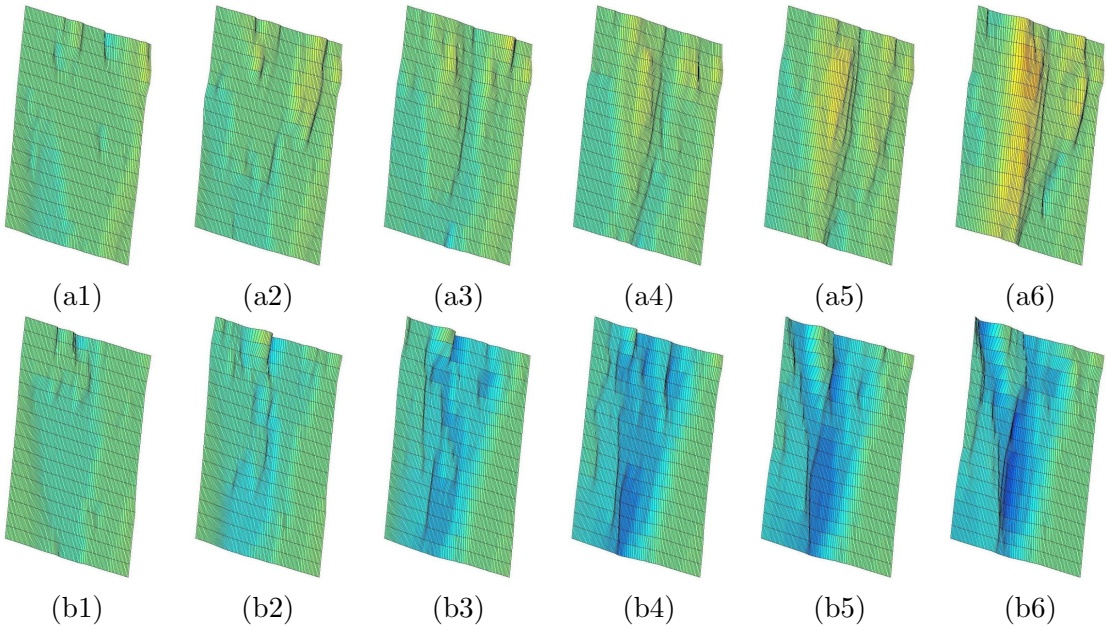

Figure 3.20: Tracking results for two tagging sheets at different locations (from time 1 to time 6). The warm color in (a) represents the tagging sheet motion out of the plane and away from the viewer, and the cold color in (b) represents the tagging sheet motion out of the plane and towards the viewer. A deformable mesh is imposed onto each tagging sheet at time 1, and captures the deformation over time.

Figure 3.20 shows the results of tracking the tagging sheets. Groups (a) and (b) depict the tracking results of two different tagging sheets. The tag sheet in (a) is located near the RV and the tag sheet in (b) is located near the LV (See Figure 3.18(b)). The tagging sheets cover the whole heart, from the atria to the ventricle apex. The lower parts of the both tagging sheets are relatively smooth and of big displacement. This is because these two areas correspond to the left ventricle, which is thicker and deforms

more than the right ventricles and the atria. From the right hand side portion of the result images in (a) we observe a thin layer whose displacement is relatively big. This corresponds to the right ventricle. Between the right ventricle and the left ventricle we observe the mesh relatively smooth and of small displacement. This is because the tagging sheets are flushed out in the blood pool soon after the systole begins, thus the mesh deforms passively in this region. We also observe relatively irregular meshes in the top portion of both tagging sheets, which is because the atria are very thin and the tagging sheets are not observable. We find visual observation of the two tracking results fits very well with the cardiac anatomy.

3.4 Conclusion

In this chapter, we presented a set of image precessing methods for tagged MRI, including image preparation, tag extraction, and tag tracking in both 2D and 3D. The fundamental method behind the extraction and tracking applications is the tunable Gabor filter bank, which is a spatially localized filtering method that is more adaptive to the tag pattern's large local deformations. We find that the Gabor filter bank can enhance and extract the tag patterns in both 2D and 3D tagged MR data, and helps with the subsequent tag tracking.

The tag tracking method is based on a set of deformable models, either *Snakes* or 3D spring meshes. The tracking must be confined in the myocardial contours, so that we are only tracking the tags on the myocardium.

Chapter 4

Tag Removal

In tagged MRI, magnetically pre-saturated lines or grids are applied to the patient's whole thoracic area, including the heart and its neighboring organs, such as chest wall and liver. As shown in Fig. 4.1, the anatomical structures in MR image are covered by dark tag patterns, which will bring challenges to the following image processing and analysis tasks, such as cardiac boundary segmentation. This is because most boundary segmentation methods are based on information of intensity gradient (edges) and/or intensity homogeneity (regions). However, in tagged MRI, intensity gradient at organ boundaries, and intensity homogeneity within a single tissue, are corrupted in the presence of tagging lines or grids.

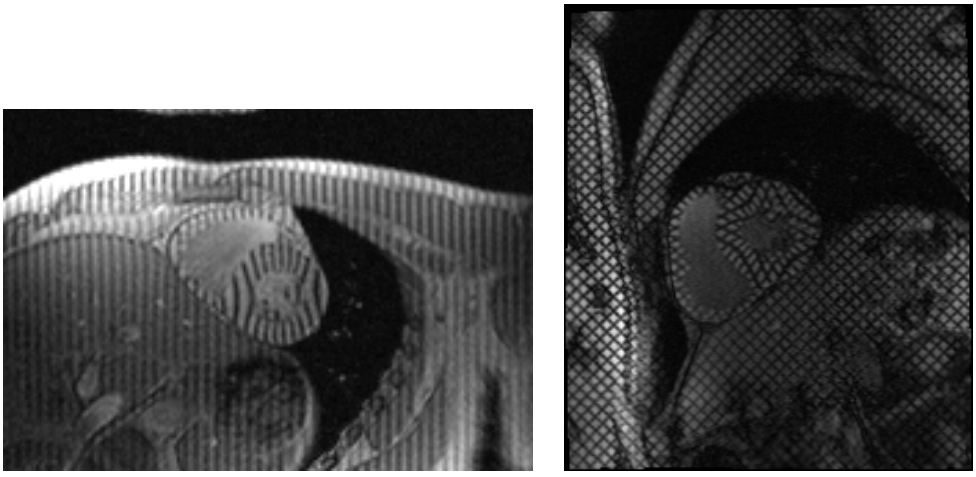

(a) (b)

Figure 4.1: Tagged cardiac MR sample images in the short axis view. The heart is located at the center of the image with deformed tag patterns. (a) is an example of line pattern, and (b) is an example of grid pattern. Both tag patterns are routinely used in research and clinical environments.

To address the difficulty added by tagging lines, several researchers have proposed image preprocessing methods to remove or suppress the tagging lines. In [27, 38] the

authors implemented gray-scale morphological operations to fill up the dark tagging lines. In [36] the author developed a filtering method to enhance the tag-patterned region and increase the blood-to-myocardium contrast.

In this chapter, we develop two tag removal methods to deal with tagged MRI with different imaging settings. The first one is based on an extension of the previous Gabor filter bank technique. The second one is based on a band-stop filtering technique. Utilizing these two methods, we build up a system for tag removal tasks that works well from the very first end-diastole frame to the end-systole frame in both tagging line or grid image.

4.1 Gabor-based Tag Removal

4.1.1 Background

The Gabor-based tag removal method [39, 59] is based on the observation that after the initial tagging modulation, the tag patterns in the blood pool are flushed out very soon. As shown in Fig. 4.1, it is intuitive to utilize the texture pattern of the tags to separate the myocardium from the blood pool and the surrounding lungs. This Gabor-based method removes tagging line or grids by actually enhancing the tag-patterned region and suppressing the non-tagged region. Thus the contrast between the myocardium and its surrounding non-tagged organs is increased, which can be used to help with the myocardial segmentation.

4.1.2 Methodology

As stated in the previous chapter, a 2D Gabor filter is defined as:

$$h(x, y) = g(x', y')s(x, y) \tag{4.1}$$

where $s(x, y)$ is a complex 2D sinusoid function. In the previous chapter, only the real part of the Gabor filter is used, because we only need to enhance the tagging lines. The comparison of the real part and the imaginary part can be found in Fig. 4.2. The 2D sinusoid of the imaginary part is shifted by $\pi/2$ comparing with the 2D sinusoid

of the real part, which means its enhancing area is also shifted by $\pi/2$. Utilizing the imaginary part, we can enhance the region at the edges between the dark strip and the brighter un-tagged tissue.

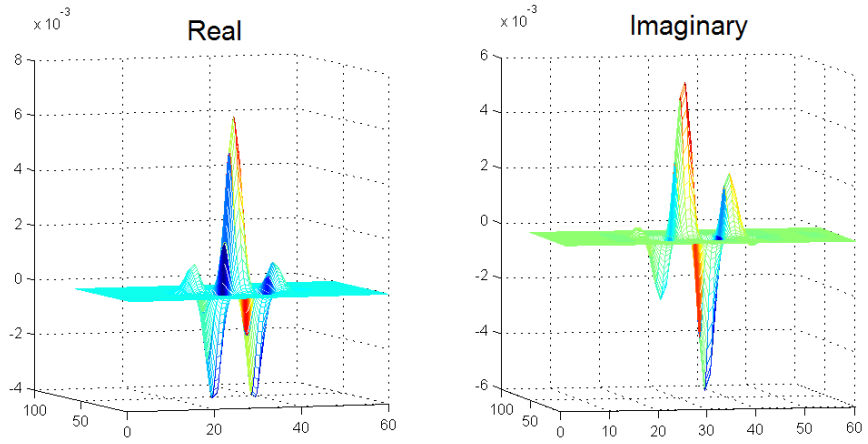

Figure 4.2: The real and imaginary parts of a 2D complex Gabor filter. We can see the 2D sinusoid of the imaginary part is shifted by $\pi/2$ from that of the real part.

If the tagging pattern is a perfect 2D sinusoid, then we can get a smoothly distributed tag removed image by calculating the magnitude of the complex filter response, as shown in Equation 4.2. As stated before, the imaginary part is actually a phase shifted variation of the real part, so Equation 4.2 is actually using the combination of the real part of Gabor filtering responses with phase shifts 0 and $\pi/2$.

$$I_{tag\_removed} = |I * h| = \sqrt{(I * \Re(h))^2 + (I * \Im(h))^2} \tag{4.2}$$

However, in many real cases, tagging lines are not a perfect sinusoid. In their spectral domain, there are higher order harmonics that affect $I_{tag\_removed}$. In order to get a more smoothly distributed $I_{tag\_removed}$, we introduce a phase modulation parameter ω. We extend the Equations 3.15 and 3.16 to the following equations by adding the phase modulation parameter ω, which represents the relative position of the current pixel with respect to the nearby tagging line. Therefore, tuning ω makes the enhancement shift away from the tagging lines.

$$U' = \Re\{(U + i \cdot V) \cdot m \cdot \exp(i \cdot \Delta\phi + \omega)\} \tag{4.3}$$

$$V' = \Im\{(U + i \cdot V) \cdot m \cdot \exp(i \cdot \Delta\phi + \omega)\} \tag{4.4}$$

We are still only using the real part of the Gabor filter. By sampling a range of discretized ω from 0 to π, we can specifically enhance every small region on and off the tagging lines.

As stated in the previous chapters, tagging lines deform with the underlying myocardium. The spacings and orientations of the tagging lines change over time. In Equations 4.3 4.4, m and $\Delta\phi$ are parameters being tuned to adapt to the local tag spacing and orientation change. By tuning all the three parameters, m, $\Delta\phi$, and ω, of the Gabor filter, we get high responses from Gabor filtering not only in those variously deformed tagging lines, but also in the regions between or near these tagging lines. By combining the enhancing results from each filter in the "*all-three-parameter-tunable*" Gabor filter bank, we can fill in the areas that are between or near the deformed tagging lines, i.e., the tagging lines are removed and the tag-patterned areas are enhanced.

$$I_{tag\_removed} = \int_m \int_{\Delta\phi} \int_{\omega=-\pi}^{\pi} I * h_{m,\Delta\phi,\omega} dm d\Delta\phi d\omega \tag{4.5}$$

Practically, the convolution step is computed as an operation in the Fourier domain for faster implementation:

$$I * h = \mathcal{F}^{-1}\{\mathcal{F}\{I\} \cdot \mathcal{F}\{h\}\} \tag{4.6}$$

4.1.3 Preprocessing for Grid Tagging Data

Grid tagging data have two sets of perpendicular tagging lines that track horizontal and vertical motions at the same time, which avoids the registration difficulty between the images of horizontal and vertical tagging lines. However Gabor filter-based method cannot handle the grid data.

We developed a preprocessing method to separate the grid tagging data into horizontal and vertical tagging lines. This method is based on a 2D low-pass filtering technique. As seen in Fig. 4.3, the initial tagging grids are rotated to be parallel to the $X - Y$ coordinates. The grid tagging image has four first harmonic peaks and other

higher order harmonic peaks in its spectral domain. The harmonic peaks in the yellow circles stand for the component of the horizontal lines, and the harmonic peaks in the red circles stand for the vertical lines.

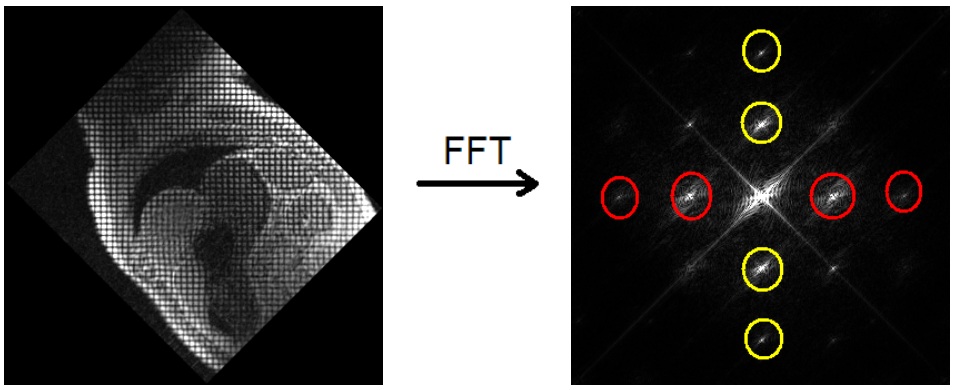

Figure 4.3: After Fourier transform, the grid tagging image has four first harmonic peaks and other higher order harmonic peaks in its spectral domain.

We denote that the first harmonic peaks in the yellow and red circles have 2D frequencies $(0, \pm f_{horizontal})$ and $(\pm f_{vertical}, 0)$, respectively. Then we can implement a low-pass filtering precess to attenuate frequency energies of tagging lines in one direction, so as to extract the others. The low-pass filter $F_{horizontal}$ is designed as:

$$F_{horizontal}(x, y) = \begin{cases} 0, \ y > \frac{f_{horizontal}}{2} \\ 1, \quad elsewhere \end{cases} \tag{4.7}$$

The low-pass filter $F_{vertical}$ is designed as:

$$F_{horizontal}(x, y) = \begin{cases} 0, \ x > \frac{f_{vertical}}{2} \\ 1, \ \ elsewhere \end{cases} \tag{4.8}$$

In order to make the low-pass filter more spatially localized, we add a roll-off edge by convolving F with a 2D Gaussian whose σ is empirically set to a small value, e.g., 3. Suppose A is the Fourier transformed spectral image of input image I: $A = FFT(I)$. Thus the filtered spectrum image A' is defined as the entry-by-entry product of F and A:

$$A' = F \times A \tag{4.9}$$

We take the inverse Fourier transformation of A' to get the tagging lines separated results. Fig. 4.4 shows the whole framework.

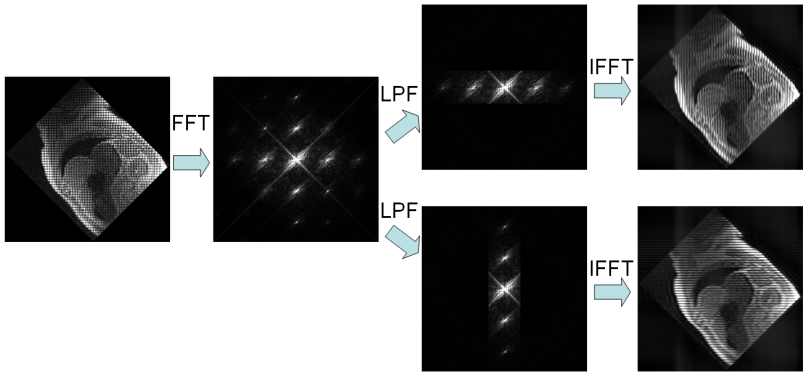

Figure 4.4: The framework of the low-pass filtering method used to separate the grids data into two sets of tagging lines.

Fig. 4.5 shows the representative results of the grid data separating method. The tag removal process will be applied on these results. And the final tag removed image from the grid data is a combination of the results from the tag removed images of the two sets of tagging lines.

4.1.4 Experimental Results

Since this Gabor filter-based tag removal method enhances the areas with patten of tagging lines, it works best on tMR images that are a few frames after the initial presaturated lines or grids are administrated. It can enhance the blood-to-myocardium contrast and facilitate myocardium segmentation. As shown in Figure 4.6, the de-tagged images in mid-systolic phase make the boundary segmentation tasks easier.

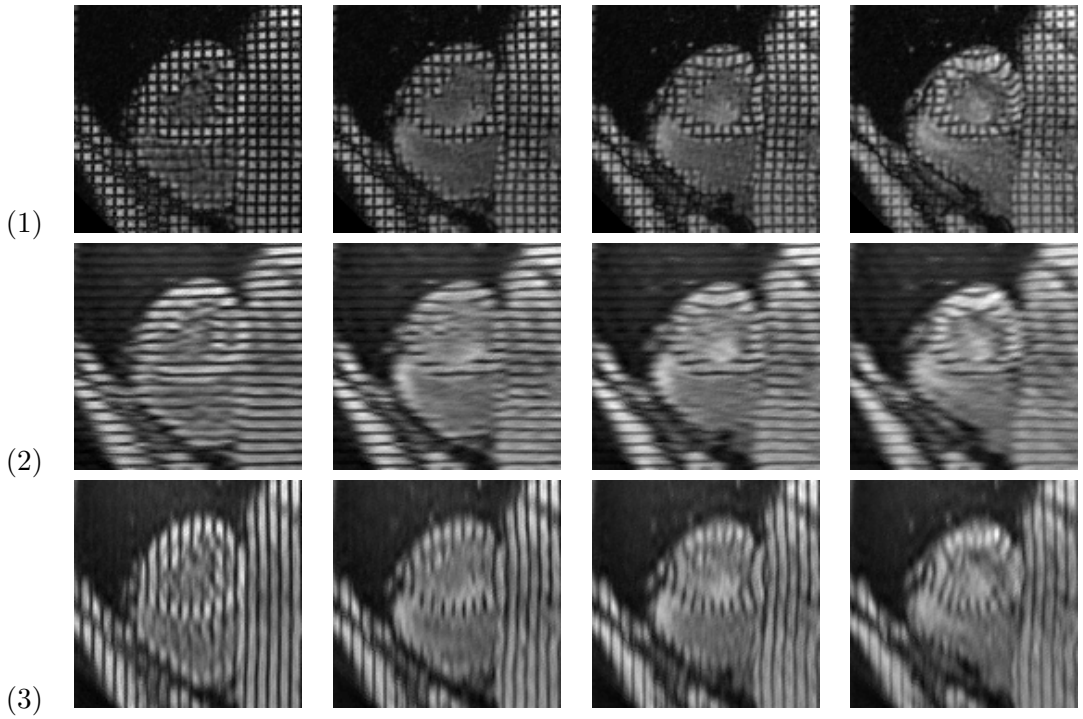

Figure 4.5: The results of the tagging lines image derived from the grid data. Row 1 is the input grid data. Row 2 is the derived image with horizontal tagging lines. Row 3 is the derived image with vertical tagging lines.

4.2 Band-Stop Filtering-Based Tag Removal

4.2.1 Background

In the previous section, we developed a tag removal method based on Gabor filtering. This method works best on frames in the mid-systole, when the tags in blood pool are flushed away completely and the tags in myocardium still remain clear. Therefore, it has a limitation in dealing with images taken at the beginning of the tagged MR imaging process, when the tag patterns in the blood pool are not flushed away yet, which makes it difficult to differentiate the blood pool and myocardium using the pattern information. Another main limitation of the Gabor-based method is that the band-pass filtering process severely blurs the boundaries of the tagged regions. It is difficult to restore the detailed structures, such as of the papillary muscles, from the tag removed images.

MESSFP tMRI is a recently developed imaging technique that achieves excellent

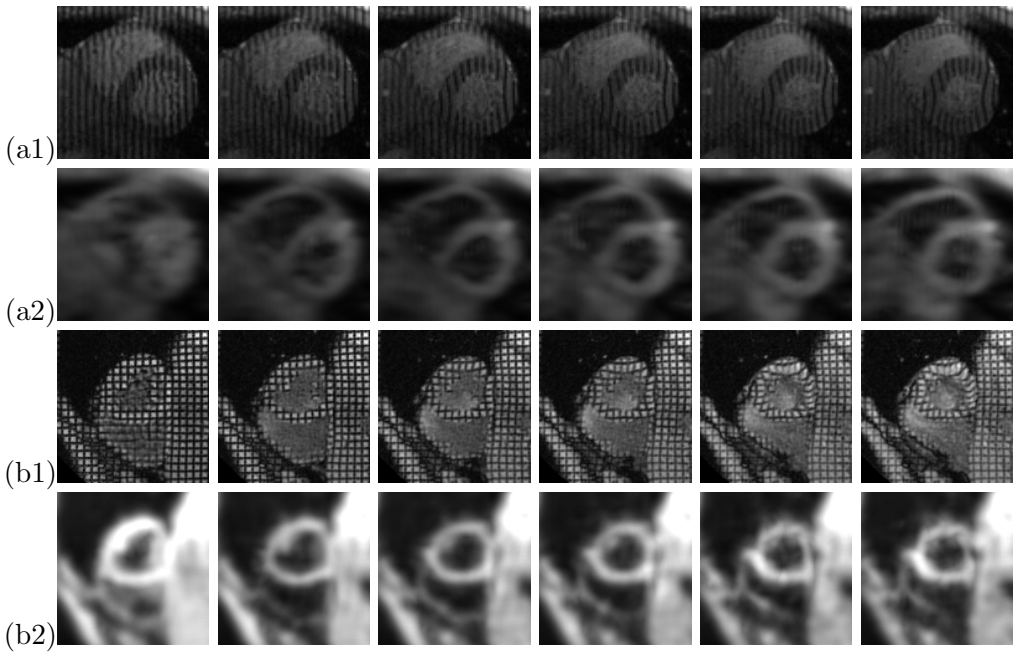

Figure 4.6: Tag removal results. Examples of original images (a1 and b1) with their tag removed images (a2 and b2). Notice that the first image in (a1) is taken right after the initial tagging administration, and the tagging lines in the blood pool are not flushed way yet, which leads to an unsatisfactory tag removal results

contrast between myocardium and blood pool. It is a good practice to keep improving the available methods in accordance with the advancing of the imaging techniques. While the previously stated Gabor-based tag removal method still works, we develop a novel tag removal method based on 2D band-stop filtering, which is operated in the image's 2D spatial-frequency domain. This method preserves the appearance of the original images with high resolution.

As seen in Fig. 4.7, the tagging lines in the spatial domain appear as quasi-2D sinusoid waves (but not perfect 2D sinusoid waves), therefore in the frequency domain of the MRI, in addition to the low frequency peak at the origin, there are several harmonic energy peaks placed symmetrically around the low frequency peak, including the first and the higher order harmonics.

The purpose of the band-stop filtering is to attenuate these harmonic energies in the 2D frequency domain that are introduced by the spatial tag patterns, so that after the 2D inverse Fourier transform, the spatial pattern of the tagging lines can be removed.

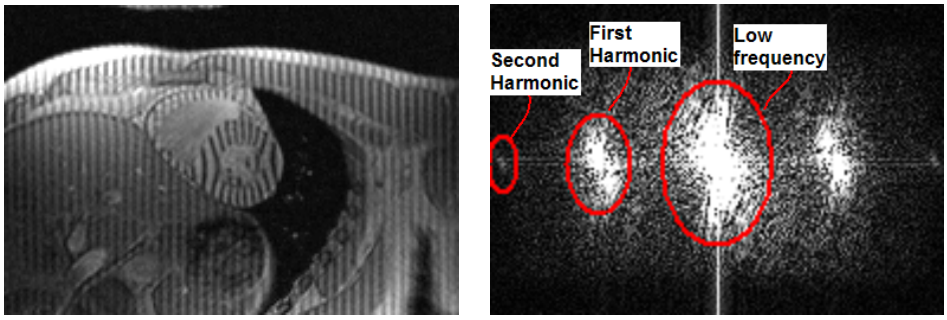

(a) (b)

Figure 4.7: (a) A tagged cardiac MR sample image in the short axis view. The heart is located at the center of the image with deformed tagging lines. (b) The magnitude spectrum image of (a). This image is symmetric w.r.t. the center origin. Besides the low frequency region, it has four visible harmonic peaks, two first harmonics and two second harmonics.

To design an optimal band-stop filter, we have two major concerns. First, in order to remove the tag patterns, the harmonic frequency regions should be effectively suppressed. Second, the other frequency components, such as the low frequencies and the other high frequencies, should be preserved as much as possible, so that the filtered image will not lose image details or be over smoothed. Therefore, the most important task is to precisely delineate the harmonic regions from the power spectrum image. However, as shown in Fig. 4.7(b), the harmonic regions are usually scattered over a large range of frequencies around the harmonic peaks, and heavily mixed with each other or with the low frequency region, which makes the delineation a hard task.

4.2.2 Methodology

In this section, we developed two techniques to solve the delineation task. First we developed a Mean Shift-based [60, 61] clustering method to automatically partition the spectrum image into regions that each contain a single dominant energy peak. Then, for regions containing harmonic peaks, we implemented a Principal Component Analysis-based multivariate fitting procedure to find an optimal sized 2D asymmetric Gaussian to model this harmonic region.

We have implemented this band-stop filtering based tag removal method on more

than 150 real tagged cardiac MR images acquired with different imaging settings. Compared to the Gabor filtering based tag removal methods in the previous section, the results of this method are more consistent with the original image appearances, and can recover more detailed structures, such as the papillary muscles. This method is also able to work on more frames, which are taken at the beginning of end-systole. Conventional region based segmentation method [62] performs better on the tag removed images by using the new tag removal method than by using the the previous [39, 59] method. We also find this tag removal method makes the segmentation of the papillary muscles in tagged MRI possible. To the best of our knowledge, there is no previous work that achieved papillary muscle segmentation in tagged MRI.

Our tag removal framework is outlined by the flowchart in Fig. 4.8. As shown in the flowchart, the input image first needs to be Flourier transformed to its frequency domain, because the following steps are all operated on its spectrum image. However, since raw MRI data are complex spectrum images before data parsing, our method can directly be applied on raw MRI data and avoid the first 2D Flourier transform step.

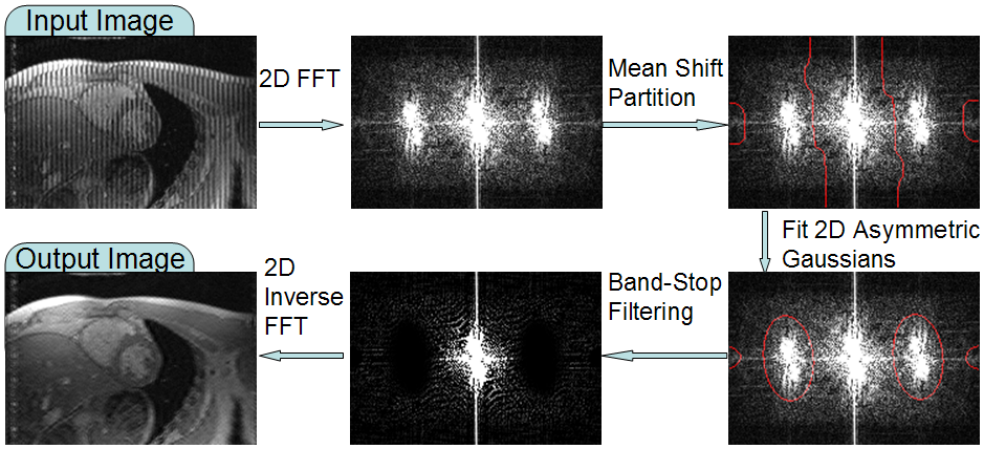

Figure 4.8: The flowchart of our proposed framework. First the input image is transformed to the frequency domain. Then the spectrum image is divided into regions based on the spectral energy peaks. Third, for regions containing a harmonic peak (there are the first and the second harmonic peaks in the image), we fit a 2D Gaussian to model it. Finally the band-stop filters are designed to attenuate the 2D Gaussian regions. The output image is from the inverse Fourier transform of the filtered spectrum image.

Partition The Spectrum Image Via Mean Shift

Mean shift is a well known cluster analysis technique [63, 60, 61]. It has a wide range of applications in image processing and analysis, such as image segmentation [61] and object tracking [64]. In this section, in order to segment the harmonic regions from the magnitude spectrum image, we adapted the mean shift method to find the energy peaks and partition the magnitude spectrum image into several regions so that each region contains only one energy peak. Mean shift method usually works as a mode seeking procedure. However, for the magnitude spectrum image, the data points, i.e., the pixels, are evenly placed in the 2D Cartesian coordinates. Thus we add a weight function in the formula which equals the intensity value I of the magnitude spectrum image. Note that since I is symmetric w.r.t. the origin, the mean shift algorithm only needs to be applied on half of the image. Let S denote the set of 2D coordinates of the image pixels in the 2D Euclidean space X. Then at $x \in X$, the mean shift is defined as:

$$m(x) = \frac{\sum_{s \in S} e^{-\frac{\|x-s\|^2}{2\sigma^2}} I(s)s}{\sum_{s \in S} e^{-\frac{\|x-s\|^2}{2\sigma^2}} I(s)} - x \tag{4.10}$$

where σ is the standard deviation of a 2D symmetric Gaussian kernel.

Starting from a pixel $x = s$, the mean shift vector $m(x)$ is calculated iteratively and moves the data point until convergence. It is like a hill climbing procedure until it finds the nearby dominant energy peak in the power spectrum image. See Fig. 4.9(a) for an example. Every pixel in the magnitude spectrum image undergoes the mean shift process. The pixels that converge to the same peak are partitioned into the same region.

In the mean shift algorithm, σ is the only parameter that needs to be tuned. Here σ is automatically adjusted by the partition results. If the number of the partitioned regions is too big, e.g., in the case that the second harmonics partially or fully appear in the frequency image, and the partition number is greater than 5 (as shown in Fig. 4.9(b)), we need to increase the value of σ. On the other hand, if the number is less

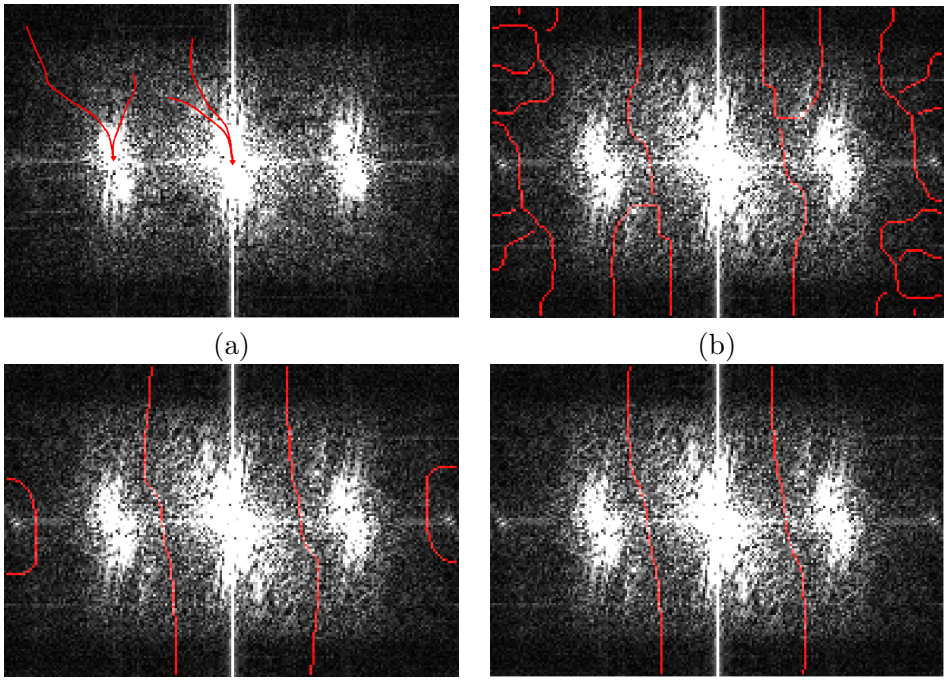

Figure 4.9: (a) shows the mean shift tracks starting from four pixels, two of which converge to the first harmonic peak, and the other two converge to the low frequency. (b-d) are the partition results using $\sigma = 3$, 4, and 5.5 respectively.

than 5 (as shown in Fig. 4.9(d)), we will need to decrease the value of σ. For a 200×200 pixel-sized image, we initially set $\sigma = 6$. As seen in Fig. 4.9(b-d), the partition number varies with σ's value. In the case that the second harmonic is not separable from the first one, we partition them with a center line in between.

Model Harmonic Peaks Via PCA Analysis

From the previous mean shift process, each partitioned harmonic region has only one dominant energy peak. However, all the pixels in the region don't necessarily belong to the region's scattered harmonic. If we band-stop filter the whole region, we may lose the informative frequency components and over-smooth the image. Therefore, in order to keep the image's details as much as possible, we model the harmonic energy peak as a 2D asymmetric Gaussian, and the band-stop filtering process is only applied in the ranges constrained by the set of 2D Gaussians.

We let S_i denote the set of 2D coordinates, which are denoted by $s_k = (x_k, y_k), k \in$

$[1, N]$, of the image pixels within a partitioned region R_i. Let s_0 denote the coordinate of the dominant spectrum power peak within R_i, so that $s_0 = \text{argmax}_{s_k \in S_i} I(s_k)$. Then we define the covariance matrix C as:

$$C = \frac{1}{\sum_{s_k \in S_i} I(s_k)} \cdot B \cdot \begin{bmatrix} I(s_1) & 0 & \dots \\ 0 & \ddots & 0 \\ \vdots & 0 & I(s_N) \end{bmatrix} \cdot B^T \tag{4.11}$$

where,

$$B = \begin{bmatrix} x_1 - x_0 & \dots & x_k - x_0 & \dots & x_N - x_0 \\ y_1 - y_0 & \dots & y_k - y_0 & \dots & y_N - y_0 \end{bmatrix} \tag{4.12}$$

Note that the dimension of C is 2×2. We apply principal component analysis on C and get the eigenvectors v_1 and v_2, and the eigenvalues λ_1 and λ_2. Thus the 2D Gaussian's orientation ϕ is determined by v_1:

$$\phi = \arctan \frac{v_1(2)}{v_1(1)} \tag{4.13}$$

and its standard deviations in v_1 and v_2 directions are set as $\sqrt{\lambda_1}$ and $\sqrt{\lambda_2}$. Thus the 2D Gaussian is defined by:

$$g(x, y) = \frac{1}{2\pi\sqrt{\lambda_1 \lambda_2}} \exp\{-\frac{1}{2}[\frac{(x')^2}{\lambda_1} + \frac{(y')^2}{\lambda_2}]\} \tag{4.14}$$

where,

$$\begin{bmatrix} x' \\ y' \end{bmatrix} = \begin{bmatrix} \cos(\phi) & \sin(\phi) \\ -\sin(\phi) & \cos(\phi) \end{bmatrix} \cdot \begin{bmatrix} x - x_0 \\ y - y_0 \end{bmatrix} \tag{4.15}$$

The band-stop filter F_i for the partitioned harmonic region R_i is designed to attenuate the frequencies in the range of the 2D Gaussian:

$$F_i(x, y) = \begin{cases} 0, \ g(x, y) > t \\ 1, \ elsewhere \end{cases} \tag{4.16}$$

where t is a threshold value, which can be determined by the 2D Gaussian's value on the crossing point (x_c, y_c) of the partition edge and the center axis that links the low

frequency peak and the harmonic peaks. For the first harmonic, we use the partition edge between the low frequency region and the first harmonic. For the second harmonic, we use the partition edge between the first and the second harmonics. Therefore $t = g(x_c, y_c)$. See the image on the lower right corner of Fig. 4.8 for an example. The red circles represent the band-stop regions.

In order to make the band-stop filter more spatially localized, we add a roll-off edge by convolving F_i with a 2D Gaussian whose σ is experimentally set to a small value, e.g., 3. Suppose the original spectrum image is A (Note that A is complex). Thus the filtered spectrum image A' is defined by:

$$A' = \prod_i F_i \times A \tag{4.17}$$

The tag-removed image can be achieved by inverse Fourier transforming A'.

4.2.3 Experimental Results and Applications

We have run our fully automatic tag removal algorithm on a set of tagged cardiac MR images with different imaging settings, which includes 20 sequences that each contain 7 to 10 time frames. From the experimental results, we find this new method is robust and very helpful for the following image segmentation tasks. As shown in Fig. 4.10, comparing with the previous Gabor filtering based tag removal methods, this method can work on more time frames and recover more image details. The computational load is modest. Our implementation was coded in Matlab 7 on a PC with a P4 3.0GHz CPU. The tag removal process takes less than 10 seconds for a 200×200 image on average.

To test how conventional segmentation methods perform on the tag removed images, we applied a hybrid segmentation method [62], which integrates the deformable model and the Markov random field method, to segment the left ventricular (LV) endocardium on the tag-removed images. As shown in the comparison work in Fig. 4.10, our new method outperforms the previous Gabor filtering based one.

The shape and motion of the papillary muscles are critical to the cardiac function.

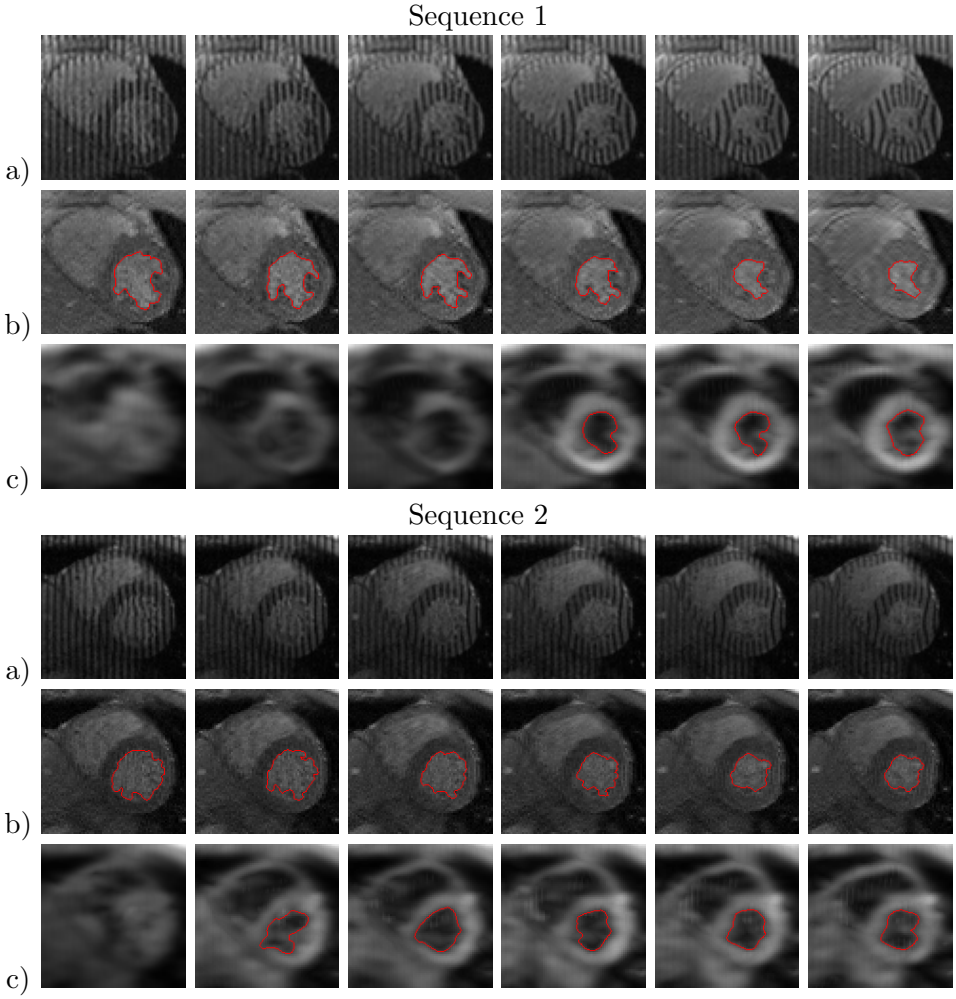

Figure 4.10: We compare our new method with the previous Gabor-based method. Here we listed two time sequences. Rows (a) show the input tagged MR images. Rows (b) show the tag removed results from our new method. Rows (c) are results from the previous Gabor-based method. The red curves are the segmentation results. Note that for the first few frames in a time sequence, the previous method cannot help with the segmentation, because the tag pattern still remains in the blood pool.

However in tagged MRI, due to the relatively small size of the papillary muscle and the complexity added by the tagging lines, segmentation of the papillary muscles remains a tough task even for human experts. The tag removal process facilitates the segmentations. Here we assume the LV endocardium has a circle shape. As shown in Fig. 4.11, based on the segmentation results in Fig. 4.10, we can easily segment the papillary muscles. To the best of our knowledge, this is the first work that achieves papillary muscle segmentation in tagged MRI.

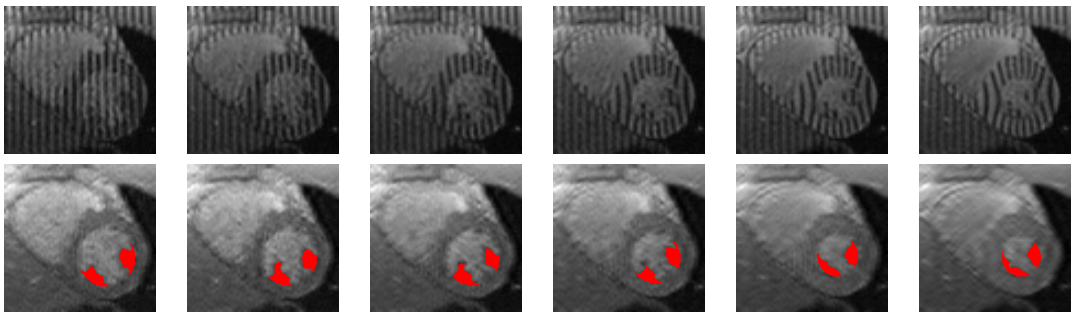

Figure 4.11: An example of the papillary muscle segmentation on the tag removed images. The first row is the input image sequence. The papillary muscles are drawn in red in the second row.

For grid tagging data, however, the MESSFP tMRI technique has not been successfully applied to grid tagging data. The myocardium and blood pool are not differentiable even if the tagging pattern is removed by the band-stop filtering method. We find that this is the main limitation of this band-stop filtering method. See Fig. 4.12 for an unsuccessful example.

4.3 Conclusion

In this chapter, we have developed two tag removal methods for tagged cardiac MRI, whose outputs improve the image readability and greatly facilitate the following cardiac segmentation.

The Gabor filtering based method essentially enhances regions with tag pattens. It can differentiate myocardium from blood pool once the tagging patterns in the blood pool are flushed away. A main advantage of this Gabor-based method is that it can successfully deal with grid tagging data. The limitations of this method are: first, it

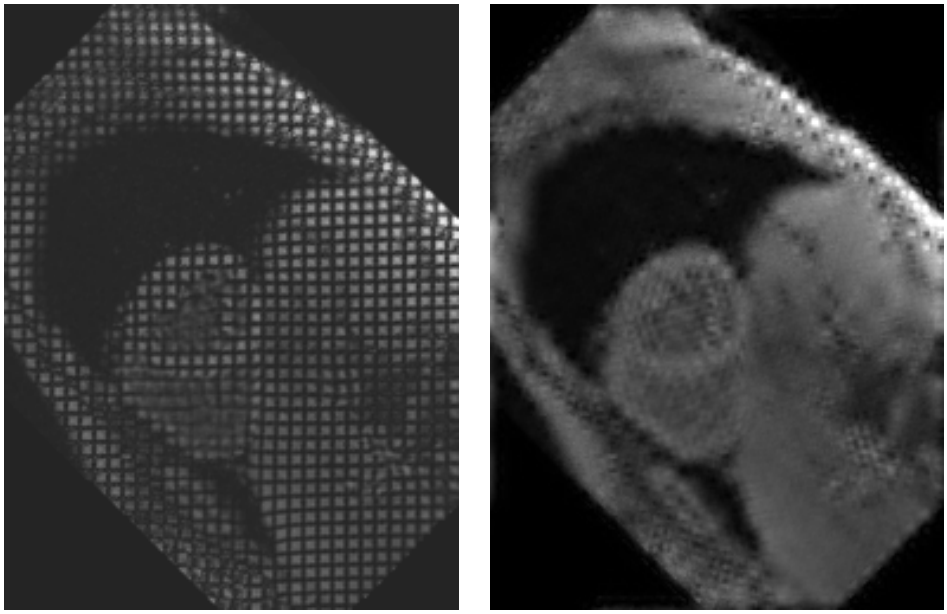

Figure 4.12: An unsuccessful example of the band-stop filtering method applied on grid tagging data. The contrast between the myocardium and blood pool is so low that it is difficult to differentiate them even if the tagging grids are removed.

is not able to deal with the first few image frames of a tMRI series. Second, the tag removed image has a very blurry appearance.

Using the band-stop filtering based method, the tag removed image has an appearance consistent with the original image, except for the tag patterns. A main advantage of this method is that it can recover very detailed cardiac structures, even the papillary muscles. We have successfully segmented the LV endocardium and LV papillary muscles on the new tag removed images. A main limitation of this method is that it can only work on images taken with the MESSFP technique, which do not include grid tagging data at this moment.

Both methods can be used as an image preprocessing routine before further image segmentation and tracking tasks. Experimental results show they are helpful for semi-automatic segmentation with possible manual corrections.

Chapter 5

Boundary Segmentation

Myocardial boundary segmentation is an essential step in tagged MRI analysis. For example, in order to accurately track the tagging lines or grids on the myocardium, we have to constrain the tag tracking to only within the heart wall, and avoid effects from the boundary edges and the tag patterns off the myocardium. This requires accurate segmentation results. For many other image analysis tasks, such as 3D heart modeling, ventricular shape analysis, and ventricular strain analysis, accurate boundary segmentation also serves as a critical image preprocessing step.

However, it has been noted by several researchers that the rate-limiting step which prevents tagged MR from clinical use is the robust segmentation of the myocardial boundary. Although there have been many research efforts on automated contour segmentation, it remains a very difficult task due to the common presence of cluttered objects, complex object textures, image noise, intensity inhomogeneity, and especially the complexities added by the tagging lines.

In this chapter, we develop two myocardial boundary segmentation methods. The first is a semi-automatic approach with an efficient computer-user interface. It integrates tag removal, Metamorph segmentation and myocardial tracking techniques to alleviate user's workload and speed up the whole segmentation process. Based on this method, we developed a prototype software system, the "Rutgers Heart Demo", which has been used to process a large amount of data in our group. The second method is a fully automatic approach that is based on machine learning. Using the results from the prototype system as the training input, we learned the shape priors, boundary criteria, and motion patterns to achieve automatic, accurate and robust segmentation. This automatic segmentation method is further extended into a non-parametric tracking

framework.

5.1 Boundary Segmentation via Tag removal and 4D Spatio-temporal Propagation

5.1.1 Background

To address the difficulty added by tagging lines, before the segmentation process, the Gabor based tag removal technique stated in the previous chapter is applied to remove the tagging lines and enhance the tag-patterned region. Because the tag patterns in the blood are flushed out very soon after the initial tagging modulation, this de-tagging technique actually enhances the blood-myocardium contrast and facilitates the subsequent segmentation of the myocardium from the blood pool.

Our segmentation framework is based on a newly proposed deformable model, which we call "MetaMorphs" [65]. The key advantage of the MetaMorphs model is that it integrates both shape and interior texture and its dynamics are derived coherently from both boundary and region information in a common variational framework. These properties of MetaMorphs make it more robust to image noise and artifacts than traditional shape-only deformable models.

A full set of conventional spatio-temporal(4D) tagged MRI consists of more than one thousand images. Segmenting every image individually is a time-consuming process that is not clinically feasible. We propose a new myocardium tracking technique which enables temporal propagation of the heart wall boundaries over the heart beat cycle. Through this propagation, we only need to do myocardium segmentation at one time, then it will be propagated both spatially and temporally to segment the whole set efficiently. This method is based on implementing a tunable Gabor filter bank to observe the deformations of the tagging lines over time [66]. This is possible because we can approximate the displacements (or deformations) of the tagging patterns by estimating the changes in parameter values of the Gabor filters that maximize the Gabor response over time. The motion of the tagging lines indicates the underlying motion of the myocardium, and therefore, the motion of the heart wall boundaries. Spatial

propagation of the heart wall boundaries is more difficult due to the complex heart geometry and the topological changes of the boundaries at different positions of the heart. Our solution is segmenting a few key slices first, which represent the topologies of the rest of the slices. Then we let the key frames propagate to the remaining slices.

A prototype system was developed allowing us to efficiently process a large amount of 4D tagged MRI data.

5.1.2 Methodology

MetaMorphs Segmentation on Tag Removed Image

The implementation details of the Gabor-based tag removal method can be found in Chapter 4. The theoretical and implemental details of the MetaMorphs segmentation method can be found in [67]. In the following, a brief introduction of MetaMorphs segmentation on tag-removed image is presented.

In the MetaMorphs framework, the shape of an evolving model is implicitly embedded as the zero level set of a higher dimensional distance function using the Euclidean distance transform [68].

The model deformations are efficiently parameterized using a space warping technique, the cubic B-spline based Free Form Deformations (FFD)[69, 70]. The essence of FFD is to deform an object by manipulating a regular control lattice F overlaid on its volumetric embedding space. In this paper, we consider an Incremental Free Form Deformations (IFFD) formulation using the cubic B-spline basis [67].

The interior intensity statistics of the models are captured using nonparametric kernel-based approximations, which can represent complex multi-modal distributions. Using this nonparametric approximation, the intensity distribution of the model interior gets updated automatically while the model deforms.

When finding object boundaries in images, the dynamics of the MetaMorphs models are derived from an energy functional consisting of both edge/boundary energy terms and intensity/region energy terms.

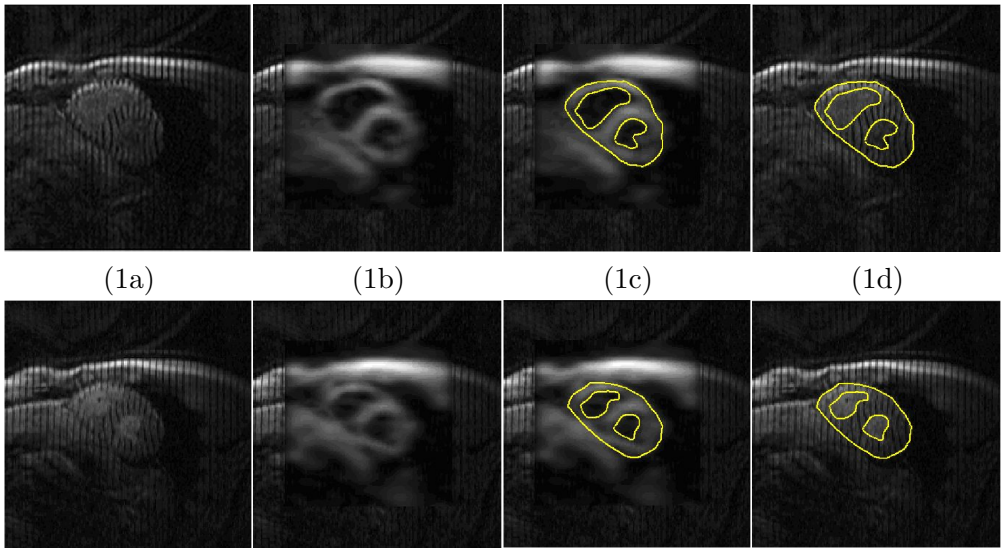

Figure 5.1: MetaMorphs segmentation on de-tagged images. (1) segmentation at time 7, slice position 7. (2) segmentation at time 7, slice position 10. (a) original image. (b) image with tags removed by gabor filtering. (c) cardiac contours segmented by MetaMorphs on de-tagged image. (d) contours projected on the original image.

In Fig. 5.1, we show the Left Ventricle, Right Ventricle, and Epicardium segmentation using MetaMorphs on de-tagged MR images. By having the tagging lines removed using Gabor filtering, a MetaMorphs model can get close to the heart wall boundary more rapidly. Then the model can be further refined on the original tagged image.

The MetaMorphs model evolution is computationally efficient, due to our use of the nonparametric texture representation and FFD parameterization of the model deformations. For all the examples shown, the segmentation process takes less than $200ms$ to converge on a 2GHz PC station.

Myocardial tracking

Recall in Equations 4.3 and 4.4, the Gabor filter is modulated by tuning the parameters m, $\Delta\phi$, and ω, and makes up a Gabor filter bank.

$$U' = \Re\{(U + i \cdot V) \cdot m \cdot \exp(i \cdot \Delta\phi + \omega)\} \tag{5.1}$$

$$V' = \Im\{(U + i \cdot V) \cdot m \cdot \exp(i \cdot \Delta\phi + \omega)\} \tag{5.2}$$

The modulated Gabor filter is formulated as:

$$h(x,y) = g(x,y) \times \exp[-j2\pi(U'x + V'y)] \tag{5.3}$$

At each pixel in the input image, we apply the tunable Gabor filter bank and find out a set of optimal filter parameters, m, $\Delta\phi$, and ω, that maximize the Gabor filter response. The optimal parameter values at each pixel make up three parameter maps that provide the region properties around the certain pixel. Figure 5.2 are the parameter maps that consist of those optimal parameter values. The tagging lines' spacing, orientations and the relative positions of each pixel are clearly illustrated. At the same time, a threshold is applied based on the value of the maximum response of the Gabor filter bank. When there are no tagging lines in a certain area, the Gabor response becomes very weak and thus below a certain threshold, then this area will be wiped out and we won't consider it (as the green area shown in Figure 5.2).

From the m map and the ω map, we can learn the tissue's relative distance with respect to the nearby tagging lines, i.e., at a certain pixel, the distance between this pixel and the nearby tagging line is determined by:

$$D = D_{original} \cdot \omega/(2\pi \cdot m) \tag{5.4}$$

where $D_{original}$ is the original spacing between two un-deformed tagging lines. If the deformation of a certain material point in 2 intermediate time sequential MRI is not bigger than a half of the spacing between two nearby tagging lines, which is true in most of our tagging MRI images because of the high imaging speed and the relatively slow heart deformation, the change of the ω maps coupled with the m maps can approximately tell the displacement of the underlying tissue by:

$$\begin{aligned} \Delta D &= D_{original} \cdot \Delta\omega/(2\pi \cdot m) \\ &= D_{x\_original} \cdot \Delta\vec{\omega}_x/(2\pi \cdot m_x) + D_{y\_original} \cdot \Delta\vec{\omega}_y/(2\pi \cdot m_y) \end{aligned} \tag{5.5}$$

For conventional short axis(SA) tagged MRI sequences, we have two sets of data

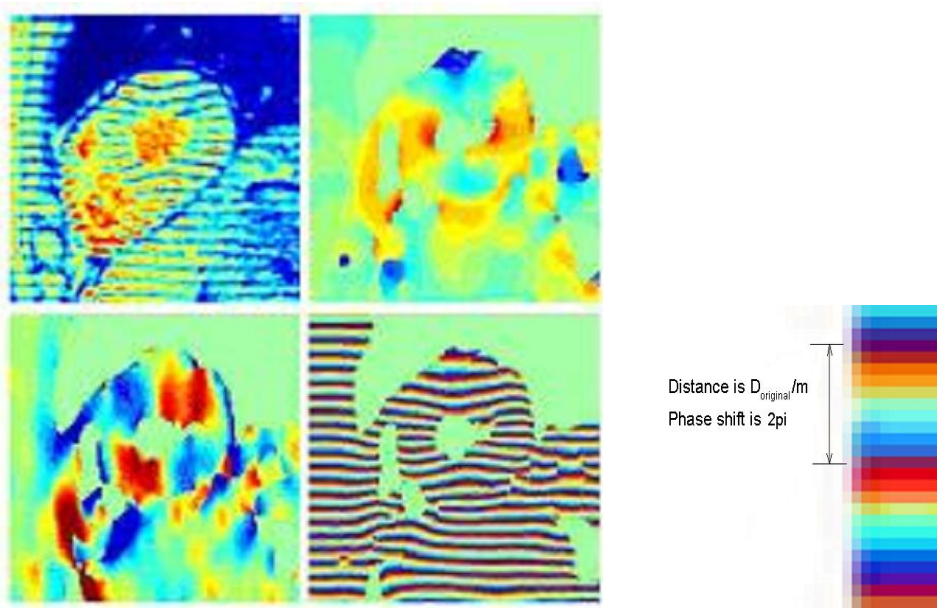

(a) (b)

Figure 5.2: (a) The upper left image is the original input MR image. The upper right one is the spacing m map. The warm color indicates the spacing between tagging lines is smaller, and the cold color indicates the spacing is bigger. The lower left image is the orientation $\Delta\phi$ map. The warm color means the orientation of the tagging lines is from lower left to upper right; the cold color means the orientation is from lower right to upper left. The lower right image is the phase ω map. The color varying from dark to bright means the phase angles vary from $-\pi$ to $+\pi$. The gray areas in the maps mean the parameters are not changed or there is no tagging lines. (b) illustrates the relationship between tag spacing and the phase shift.

whose tagging lines are initially perpendicular to each other. Thus we can use Equation 5.5 to calculate the deformations in two different orientations at each pixel in the time sequence. When we combine the horizontal and vertical deformations from the two data sets, we get the deformation of the myocardium.

According to the deformations of the tagging lines, the modulation ranges of the Gabor filter bank parameters are empirically set by:

$$\begin{aligned} m &\in [0.85, 1.3] \\ \Delta\phi &\in [-\pi/12, \pi/12] \\ \omega &\in [-\pi, \pi] \end{aligned} \tag{5.6}$$

In Figure 5.3 we show a set of myocardium tracking results from time 0 to time

9. We manually impose a 2D grid mesh onto the myocardium area and let it deform with the underlying tissue. There are some irregular deformations in some local regions because the tracking depends on the tag texture pattern alone, and MR images usually have high level noise. However the overall movement matches the underlying tissue motion properly. After smoothing, it is good enough for further tasks such as boundary tracking and motion analysis.

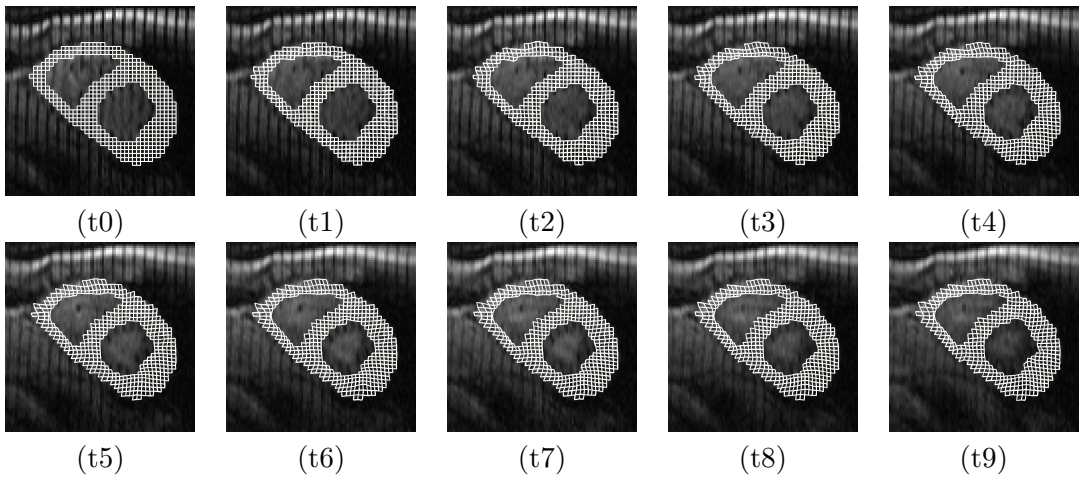

Figure 5.3: A mesh is imposed on the myocardium area and deforms along time. We can find the mesh contracts properly overall as the underlying heart tissue contracts. But in local regions, the mesh deformation results are not accurate enough. This is because our model is wholly based on the tag texture feature, which may very likely be corrupted by the neighboring boundaries and the high level noise.

Integration and the Prototype System

We integrate the MetaMorphs segmentation with the myocardial tracking method to construct our 4D spatio-temporal integrated MR analysis system. By using the two techniques in a complementary manner, exploiting specific domain knowledge about the heart anatomy and temporal characteristics of the tagged MR images, we can achieve efficient, robust segmentation with minimal user interaction. The algorithm consists of the following main steps. (The illustration of the spatio-temporal propagation can be found in Figure 5.4).

1. Tag removal for images at the mid-systolic phase. Given a 4D spatio-temporal

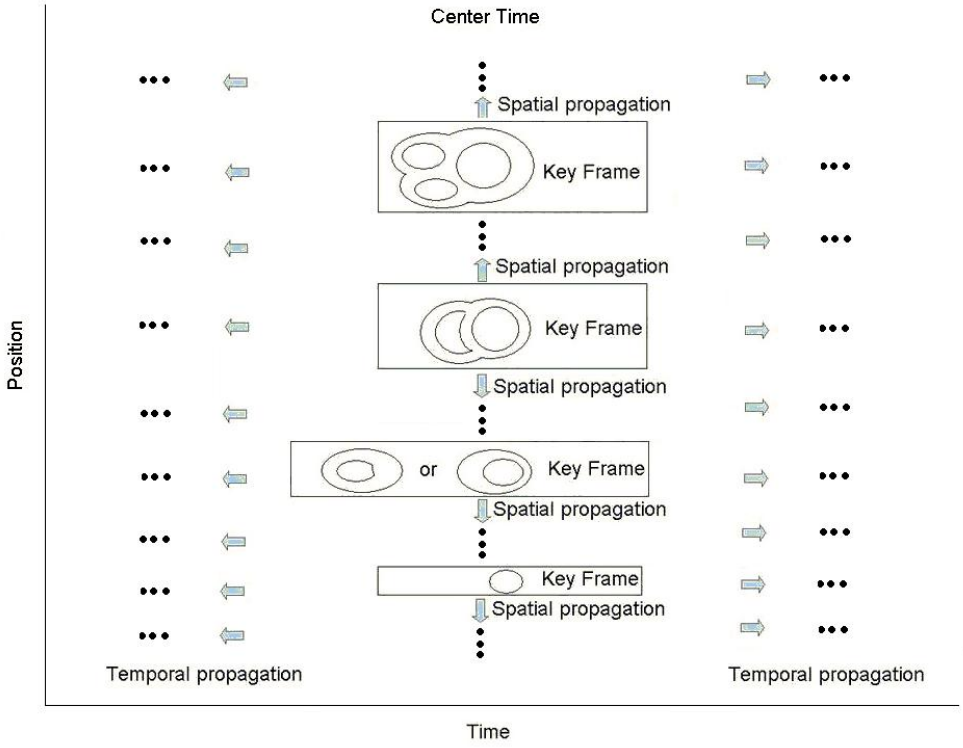

Figure 5.4: The framework of our automated segmentation in 4D spatio-temporal MRI-tagged images. We start at a center time when the tag lines are flushed away in the blood area while they remain clear in the myocardium. Boundary segmentation is done in several key frames on the de-tagged images before the boundary contours are spatially propagated to the other positions. Then at each position, the boundaries are temporally propagated to other times.

tagged MR image dataset of the heart, we start by filtering using a tunable Gabor filter bank on images of a 3D volume that corresponds to a particular time in the middle of the systolic phase, which we term *'center time'*. For a typical dataset in which the systolic phase is divided into 13 time intervals, we apply the Gabor filtering on images at time 7, when tag patterns in the endocardium are flushed out by blood but tag lines in the myocardium are clearly visible.

2. MetaMorphs segmentation using the de-tagged images. Given the de-tagged Gabor response images at time 7, we use MetaMorphs to segment the cardiac contours including the epicardium, the LV and RV endocardium. Since the formulation of MetaMorphs naturally integrates both shape and interior texture, and the model deformations are derived from both boundary and region information, the MetaMorphs

models can be initialized far away from the object boundary and efficiently converge to an optimal solution. For each image, we first segment the LV and RV endocardium. To do this, the user initializes a circular model by clicking one point (the seed point) inside the object of interest, then the surrounding region intensity statistics and the gradient information automatically drive the model to converge to the endocardium boundaries. We then automatically initialize a metamophs model for the epicardial contour by merging the endocardial contours and expanding the interior volume according to myocardium thickness statistics. The model is then allowed to evolve and converge to the epicardium boundary.

3. Spatial propagation at the mid-systolic center time. At the mid-systolic phase, we do the segmentation at several key frames which represent the topologies of the rest of the frames, then let the segmented contours propagate to their nearby frames. In short axis cardiac MR images, from the apex to the base, the topology of the boundaries goes through the following variations: 1. one epicardium; 2. one epicardium and one LV endocardium (in some cases of the RV hypertrophy patients, one epicardium and one RV endocardium are also possible); 3. one epicardium, one LV endocardium and one RV endocardium; 4. one epicardium, one LV endocardium and two RV endocardium. The key frames consist of one center frame of the third topology and three transition frames. This spatial propagation actually provides a quick initialization method (rather than manually clicking the seed points as mentioned in step 2) for the rest of the non-key frames from the key frames.

4. Boundary tracking using the Gabor-based myocardial tracking over time. Once we have segmented the cardiac contours at time 7, we keep tracking the motion of the myocardium and the segmented contours over time. This temporal propagation of the cardiac contours significantly reduces computation time, since it enables us to do supervised segmentation at only one time, then fully automated segmentation of the complete 4D dataset can be achieved. It also improves segmentation accuracy because we capture the overall trend in heart deformation more accurately by taking into account the temporal connection between segmented boundaries.

5. Boundary refinement using MetaMorphs. In practice, we provide the option to

further refine the boundaries using MetaMorphs deformable models, which are automatically initialized using the tracked contours. We also provide a manual correction option to doctors during the whole segmentation process to ensure satisfactory results.

6. Tagging lines tracking within the heart wall. Tagging lines are straight lines at time 0. They are equally spaced at an interval of $1/\sqrt{(U^2+V^2)}$. Starting from time 0, we keep tracking the tagging lines only *within the heart wall* from the results of the boundary segmentation and boundary tracking steps above. The tagging lines' model is basically a set of *Snakes* whose external forces are from the original intensity images and the tag-enhanced images.

5.1.3 Experimental Results

The prototype of our 4D segmentation system is developed in a Matlab 6.5 GUI environment. The user needs to load in the raw MRI data of the short axis and long axis volumes first (Figure 5.5(1a)). Then the user is allowed to examine the whole data sets, which consist of two short axes and one long axis, and determine the slice index of the center time (Figure 5.5(1b,1c,2a)). The tag removal step is done on the 3D volume at the center time Figure 5.5(2b). Then the user has a option to determine the indices of the key frames and do MetaMorphs segmentation on these key frames (Figure 5.5(2c,3a,3b,3c)). The segmented contours are propagated spatially (optional) and then temporally (Figure 5.5(4a,4b)). Practically, the spatial propagation step is optional because for most clinical analysis one typical slice is enough, unless a fully 4D model is required. Manual interaction is always available during the whole segmentation and propagation process to make corrections as needed. Figure 5.5(4c) shows a segmentation result after manual correction.

5.1.4 Discussion

Several novel aspects of our proposed integration contribute to the effective nature of our approach. First, we are the first to propose and evaluate the feasibility to use deformable shape and texture models on tag-removed images for segmenting cardiac objects. Second, we designed our algorithm based on our belief that, to achieve robust

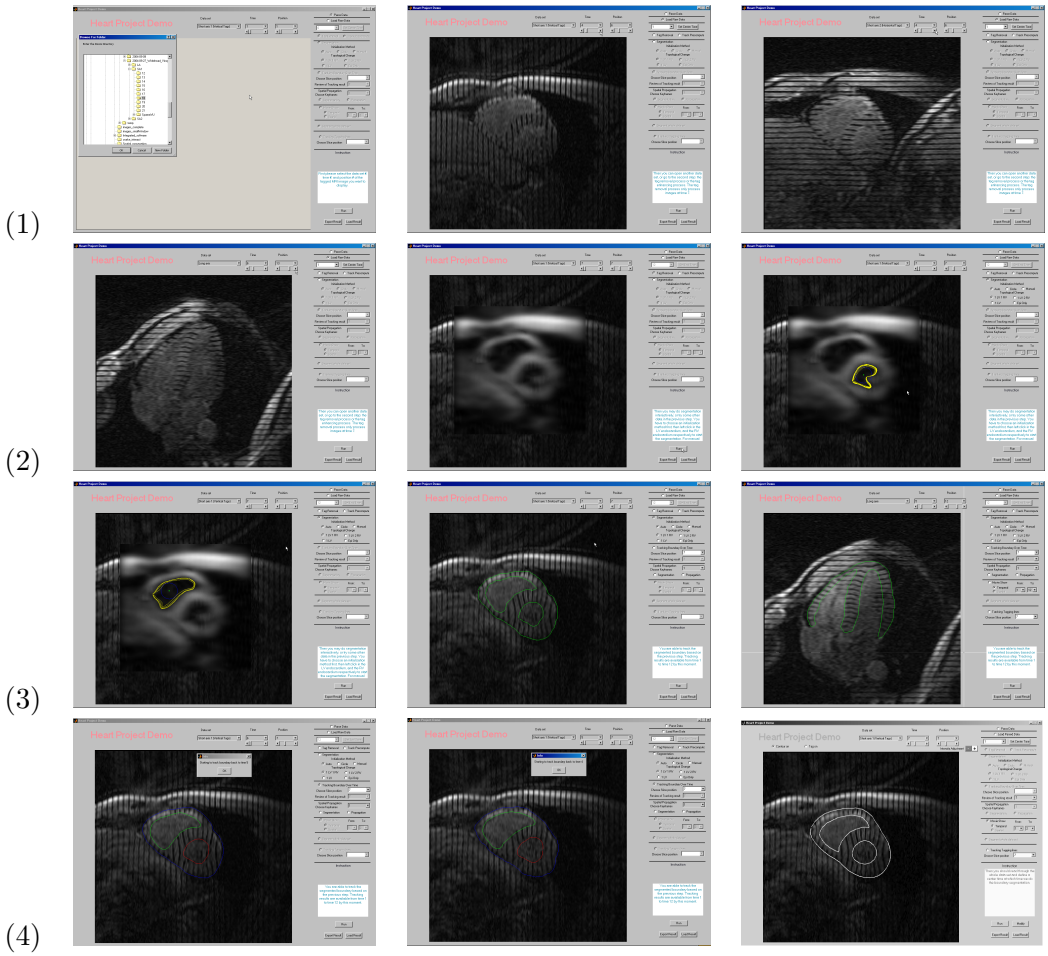

Figure 5.5: Screen snapshots of our segmentation and tracking system. (1a) read in the SA and LA volumes. (1b,1c,2a) examine the data sets. (2b) de-tagged image at the center time. (2c,3a) MetaMorphs segmentation based on de-tagged images. (3b,3c) segmentation results. The papillary muscle is excluded from the myocardium by manual interaction. (4a,4b) temporal propagation. (4c) a segmentation result after manual correction.

and automated segmentation in 4-D, we have to use information from 4D. Hence the temporal tracking and spatial segmentation are tightly coupled in our approach. The deformable model-based segmentation at a mid-systolic phase provides initialization for the tracking process, while the contour tracking returns close and reliable initialization for deformable model-based segmentation at all other times. Third, the basis techniques we use, i.e., the tunable Gabor filter bank and deformable shape and texture models (MetaMorphs), are both cutting-edge techniques that have been recently developed and recognized by the research community. Applying these techniques to the difficult tagged-MR cardiac segmentation problem has posed new challenges to the techniques themselves and in turn supported their improvements. The integration of tunable Gabor filter bank and deformable shape and texture models has enabled us to develop a generic, efficient framework for segmenting 4D spatial-temporal tagged MR images. The software that resulted from this work requires minimal user interaction, and is robust and accurate enough for clinical evaluation. Using this software, we have processed a large amount of tagged MR data, which were used as training data in the following learning based methods.

5.2 Learning-based Segmentation Approach

5.2.1 Background

The segmentation method described in the previous section has limitations. First, the Gabor filtering step removes the tagging lines, but, at the same time, blurs the boundaries, especially for the epicardial boundaries, which leads to inaccurate segmentation. Second, the method consists of several independent contour segmentations, but not a concrete shape, which likely leads to shape irregularity. Third, the method is semi-automatic, which needs human interactions throughout the whole segmentation process. For instance, during boundary tracking, the user has to make manual correction at each time. This makes this method still time consuming. Ideally we need a fully automatic method.

Automatic segmentation in tagged MRI is difficult for several reasons. First, the

myocardial boundaries are often obscured or corrupted by tagging lines, which makes the conventional edge-based segmentation method infeasible. Although the Gabor-based tag removal method enhances the contrast between myocardium and blood pool, the filtering process makes the boundary severely blurred. Second, the intensity of the tagging lines, the myocardium and the blood vary during the cardiac cycle, because of the magnetic relaxation and the tag fading effect. It is thus difficult to come up with a general edge or region based segmentation method. The last and the most important reason is that, from the clinicians' point of view, or for the purpose of 3D modeling, *accurate* segmentation based solely on the MR image is usually not possible. For instance, for conventional clinical practice, the endocardial boundary should exclude the papillary muscles for the purpose of easier analysis. However, in the MR images, the papillary muscles are often apparently connected with the endocardium and cannot be separated if only the image information is used. Thus prior shape knowledge is needed to improve the results of automated segmentation.

5.2.2 Methodology

In order to address the difficulties stated above, we proposed a novel and fully automatic segmentation method based on three learning frameworks: 1. An active shape model (ASM) is used as the prior heart shape model. 2. A set of confidence-rated local boundary criteria are learned by Adaboost, a popular learning scheme (see 5.2.2), at landmark points of the shape model, using the appearance features in the nearby local regions. These criteria give the probability of the local region's center point being on the boundary, and force their corresponding landmark points to move toward the direction of the highest probability regions. 3. An Adaboost detection method is used to initialize the segmentation's location, orientation and scale. The second component is the most essential contribution of our method. We abandon the usual edge or region-based methods because of the complicated boundary and region appearance in the tagged MRI. It is not feasible to designate one or a few edge or region rules to solve the complicated segmentation task. Instead, we try to use all possible information, such as the edges, the ridges, and the breaking points of tagging lines, to form a *complex*

rule. It is apparent that at different locations on the heart boundary, this *complex rule* must be different, and our confidence in the *complex rule* varies too. It is impractical to manually set up each of these *complex rules* and weight their confidence ratings. Therefore, we implement Adaboost to learn a set of rules and confidence ratings at each landmark point on the shape model. The first and the second frameworks are tightly coupled. The shape model deforms under the forces from Framework 2 while controlled and smoothed by Framework 1. To achieve fully automatic segmentation, in Framework 3 the detection method automatically provides an approximate position and size of the heart to initialize the segmentation step.

ASM Shape Modeling

There has been some previous research on ASM segmentation methods based on local features modeling. In [71], a statistical analysis was performed, which used sequential feature forward and backward selection to find the set of optimal local features. In [72], an EM algorithm was used to select Gabor wavelet-based local features. These two methods tried to select a small number of features, which is impractical for representation of complicated local textures such as in tagged MRI. In [73], a simple Adaboost learning method was proposed to find the optimal edge features. This method didn't make full use of the local textures, and didn't differentiate each landmark point's confidence level. In our method, similarly using Adaboost, our main contributions are: the ASM deforms based on a more *complex* and robust rule, which is learned from the local appearance, not only of the edges, but also of ridges and tagging line breakpoints. In this way we get a better representation of the local appearance of the tagged MRI. At the same time, we derive the confidence rating of each landmark point from their Adaboost testing error rates, and use these confidence ratings to weight the image forces on each landmark point. In this way the global shape is affected more by the *more confident* points and we eliminate the possible error forces generated from the *less confident* points.

Since the shape of the mid portion of the heart in short axis (SA) images is consistent and topologically fixed (one left ventricle (LV) and one right ventricle (RV)), it is

reasonable to implement an active shape model [74] to represent the desired boundary contours.

The training data sets were acquired from several normal subjects using slightly different imaging techniques. The data sets were acquired in the short axis plane. There are two sets of tagging line orientations (0° and 90°, or −45° and 45°) and slightly different tag spacings. Each data set included images acquired at phases through systole into early diastole, and at positions along the axis of the LV, from near the apex to near the base, but without topological changes. An expert was asked to segment the epicardium (Epi), the left ventricle (LV) endocardium and the right ventricle (RV) endocardium from the datasets. In total, we obtained 220 sets (each set includes one LV, one RV, and one Epi) of segmented contours to use as the training data.

Segmented contours were centered and scaled to a uniform size. Landmark points were placed automatically by finding key points with specific geometric characteristics. As shown in Figure 5.6(a), the black points are the key points, which were determined by the curvatures and positions along the contours. For instance, $P1$ and $P2$ are the highest curvature points of the RV; $P7$ and $P8$ are on opposite sides of the center axis of the LV. Then, fixed numbers of other points are equally placed in between. In this way, the landmark points were registered to the corresponding locations on the contours. Here, we used 50 points to represent the shape.

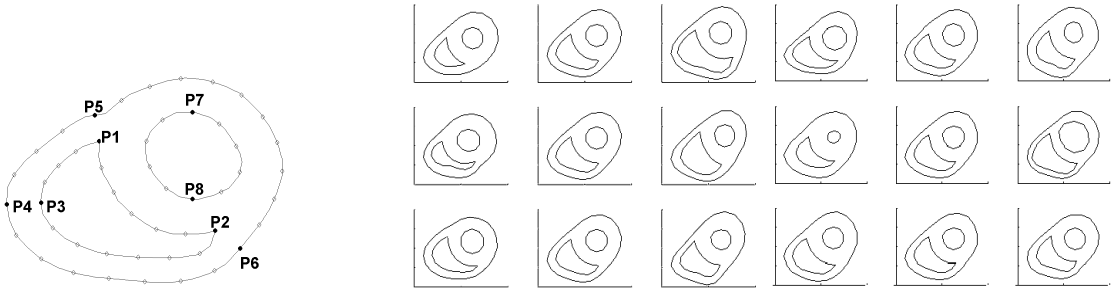

(a) (b)

Figure 5.6: (a) Here we used 50 points to represent one set of contours. (b) shows the the shape variations by the first six principle components. The 2^{nd} and 5^{th} columns are the mean shapes. The shapes to the left and right sides of the mean shapes are the variate shapes produced by adding or minus a certain amount of a principal component.

For each set of contours, the 50 landmark points (x_i, y_i) were reshaped to form a shape vector $X = (x_1, x_2, ..., x_{50}, y_1, y_2, ..., y_{50})^T$. Then Principal Component Analysis was applied and the modes of shape variation were found. Any heart shape can be approximately modeled by $X = \bar{X} + Pb$, where $\bar{X}$ is the mean shape vector, P is the matrix of shape variations, and b is the vector of shape parameters weighting the shape variations. In Figure 5.6(b), the linear shape variations from PCA analysis are illustrated.

After we find the image forces at each landmark point, as in Section 5.2.2, the active shape model evolves iteratively. In each iteration, the model deforms under the influence of the image forces to a new location; the image forces are then calculated at the new locations before the next iteration.

Learning Boundary Criteria Using Adaboost

To capture the local appearance characteristics, we designed three different kinds of steerable filters. We use the derivatives of a 2D Gaussian to capture the edges, we use the second order derivatives of a 2D Gaussian to capture the ridges, and we use half-reversed 2D Gabor filters [56] to capture the tagging line breakpoints.

Assume $G = G((x-x_0)\cos(\theta), (y-y_0)\sin(\theta), \sigma_x, \sigma_y)$ is an asymmetric 2D Gaussian, with effective widths σ_x and σ_y, a translation of (x_0, y_0) and a rotation of θ. We set the derivative of G to have the same orientation as G:

$$G' = G_x \cos(\theta) + G_y \sin(\theta) \tag{5.7}$$

The second derivative of a Gaussian can be approximated as the difference of two Gaussians with different σ. We fix σ_x as the long axis of the 2D Gaussians, and set $\sigma_{y2} > \sigma_{y1}$. Thus:

$$G'' = G(\sigma_{y1}) - G(\sigma_{y2}) \tag{5.8}$$

In the previous two equations, we set $x_0 = 0$, and tune y_0, θ, σ_x, σ_y, σ_{y1} and σ_{y2} to generate the desired filters.

The half-reversed 2D Gabor filters are defined as a 2D sine wave multiplied with the 2D derivative of a Gaussian:

$$F = G'(x, y) \cdot \mathbb{R}\{e^{-j[\phi+2\pi(Ux+Vy)]}\} \tag{5.9}$$

where G' is the derivative of a 2D Gaussian. U and V are the frequencies of the 2D sine wave, $\psi = arctan(V/U)$ is the orientation angle of the sine wave, and ϕ is the phase shift. We set:

$$\begin{aligned} x_0 &= 0, \\ \sigma_x &= \sigma_y = \sigma, \\ -45^\circ &\leq \psi - \theta \leq 45^\circ \end{aligned} \tag{5.10}$$

and tune y_0, θ, σ, ϕ, U and V to generate the desired filters.

For a 15x15 sized window, we designed 1840 filters in total. See Figure 5.7(a-c) for some sample filters.

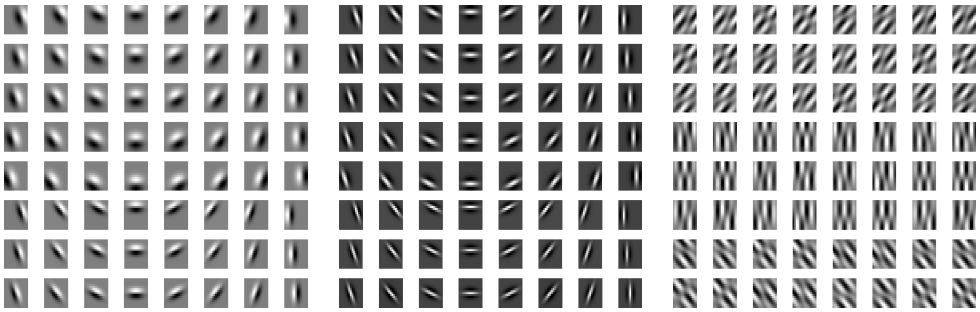

(a) (b) (c)

Figure 5.7: Sample sets of feature filters: (a) are the derivatives of Gaussian used for edge detection, (b) are the second derivatives of Gaussian used for ridge detection, and (c) are the half-reversed Gabor filters used for tag line breakpoint detection.

In the learning section, each training image is scaled proportionally to the scaling of its contours. At each landmark point of the contours, a small window (15x15) around it is cut out as a positive appearance training sample for this particular landmark point. Then along the normal of the contour, on each side of the point, we cut out two 15x15-sized windows as negative appearance training samples for this particular landmark point. Thus for each training image, at a particular landmark point, we get

one positive sample and four negative samples (shown in Figure 5.8) We also randomly select a few common negative samples outside the heart or inside the blood area, which are suitable for every landmark point. For image contrast consistency, every sample is histogram equalized.

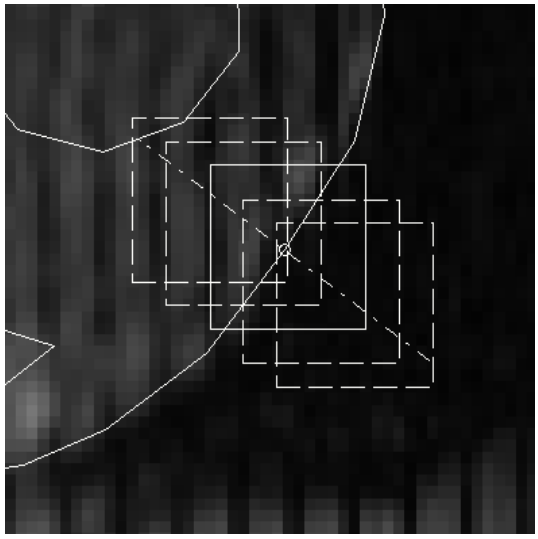

Figure 5.8: The illustration of the method to set the training data. The solid box is the positive sample around the landmark points. The four dashed line boxes along the normal are the negative samples. This way of setting the negative samples is chosen to make the classifier more adaptive to the particular landmark position.

The function of the Adaboost algorithm [75, 76] is to classify the positive training samples from the negative ones by selecting a small number of important features from a huge potential feature set and creating a weighted combination of them to use as an accurate strong classifier. During the boosting process, each iteration selects one feature from the total potential features pool, and combines it (with an appropriate weight) with the existing classifier that was obtained in the previous iterations. After many iterations, the weighted combination of the selected important features can become a strong classifier with high accuracy. The output of the strong classifier is the weighted summation of the outputs of each of its each selected features, or, the weak classifiers:

$$F = \Sigma_t \alpha_t h_t(x) \tag{5.11}$$

where α are the weights of weak classifiers, and h are the outputs of the weak classifiers.

We call F the boundary criterion. When $F > 0$, Adaboost classifies the point as being on the boundary. When $F < 0$, the point is classified as off the boundary. Even when the strong classifier consists of a large number of individual features, Adaboost encounters relatively few overfitting problems [77]. We divided the whole sample set into one training set and one testing set. The function of the testing set is critical. It gives a performance measure and a confidence level that tells us how much we should trust its classification result. Figure 5.9 shows the learning error curve versus the boosting iteration numbers at two selected landmark points. Note that every landmark point i has its own α, h and F_i.

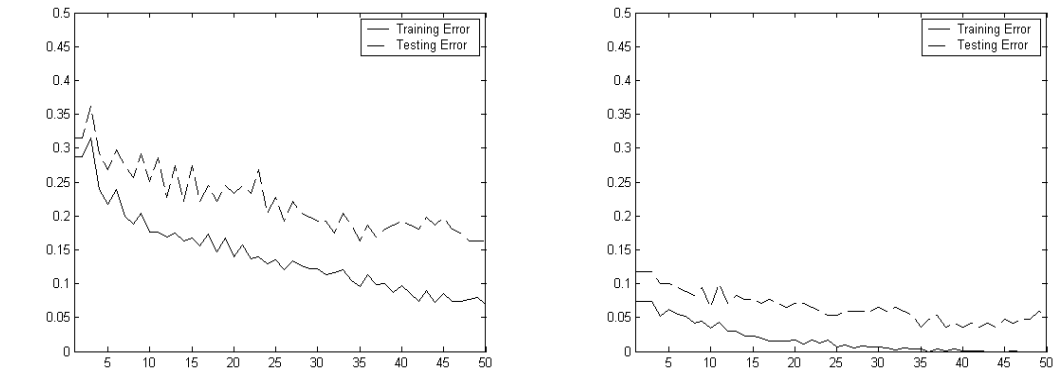

(a) (b)

Figure 5.9: (a) and (b) show the training error (solid lines) and testing error (dash lines) of two landmark points versus Adaboost iteration times. (a) is a point on the LV, (b) is a point on the Epi. Note how the training and testing error decrease as Adaboost iterates. Also note the testing error of (a) is higher than (b): we are more confident of landmark point (b)'s classification result.

Segmentation Based On Confidence Ratings

In the segmentation stage, we first select an initial location and scale, and then overlay the mean shape $\bar{X}$, which is obtained from ASM, onto the task image. In section 5.2.3 we describe an automatic initialization method.

At a selected landmark point i on the shape model, we select several equally spaced points along the normal of the contour on both sides of i, and use their F values to examine the corresponding windows centered on these points. In [77], a logistic function was suggested to estimate the relative boundary probabilities:

$$Pr(y = +1|x) = \frac{e^{F(x)}}{e^{F(x)} + e^{-F(x)}} \tag{5.12}$$

We find a point j whose test window has the highest probability of being on the heart boundary. Thus an image force $\vec{f}$ should push the current landmark point i toward j. Recall that, as discussed in the previous subsection, Adaboost gives the errors of the testing data e_i. We define the confidence rating as:

$$c_i = \ln \frac{1}{e_i}; \tag{5.13}$$

Intuitively, when c_i is big, we trust its classification and increase the image force $\vec{f}$, and conversely. Thus, we define the image force at landmark point i as:

$$\vec{f} = \mu \cdot \frac{[\vec{x}(j) - \vec{x}(i)] \cdot c(i)}{||\vec{x}(j) - \vec{x}(i)||_2} \tag{5.14}$$

where μ is the step size that equals a small number.

The detailed algorithm to update the parameters of the ASM model with the image force $\vec{f}$ can be found in [74].

5.2.3 Automatic Initialization: Heart Detection

Detection of the organ of interest in a medical image is often the first step of many medical image processing tasks. When we are dealing with medical image processing tasks, such as segmentation, registration, and tracking, first of all, we need to know where the organ of interest is located and how much area the organ covers. Usually this detection task is done manually by human experts clicking on the organ location or cropping out the region of interest.

To achieve automatic initialization for the following segmentation, our goal is to automatically detect the heart in the tagged MRI images. A closely related problem is

face detection. We find the face detection problem shares many similarities with our heart detection task. Usually there are a lot of variations among different faces, which come from different facial appearance, lighting, expression, etc, while in heart detection, we also have the same challenges: the heart has different tag pattern, shape, position, rotation, phase, etc. We can adopt the ideas from the face detection techniques.

There are many existing face-detecting works. [78, 79] were using correlation-templates-based methods. [80] used view-based eigenspaces to reduce the high dimensional vector space of all possible face patterns to a low dimensional linear subspace. [81] modeled a deformable templates. Sung, at el [82] generated two distribution models of 'face-pattern' and 'non-face-pattern' from a set of training examples. The classifier is based on the difference feature vector which is computed between the local image pattern and the distribution-based model. Papageorgiou [83] set up an over-completed Haar wavelet representation of the object class. Then they reduced the dimension and selected the most important features. They trained a support vector machine as the final classifier. Viola and Jones [84] used Adaboost method on over-completed Haar-like features to generate an accurate strong classifier from a set of weak classifiers. They also implemented a cascade detection method to achieve high computation speed. Here we adopted Viola and Jones's Adaboost learning framework, because a human's prior knowledge tends to add bias constraints on the detection model, and we hope the algorithm will totally learn its rules from the training data without any *a priori*. Furthermore, their implementation is accurate and relatively fast.

As mentioned in the previous section, Adaboost algorithm [75] selects a small number of important features from a huge feature set and generates an accurate strong classifier. During the boosting process, each iteration selects one feature from the total potential features, and weighted combines it with the existing classifier that obtained in the previous iterations. After many iterations, the weighted combination of the selected important features turns to be a strong classifier with high accuracy.

Feature Design

The similar Haar wavelet functions in Viola's paper are used as features of the weak classifiers, as seen in Fig. 5.10. The filtered result of a feature is found by convolving the input image with the feature window. These rectangle features have many advantages. First, they are able to encode ad-hoc domain knowledge that is difficult to learn using pixel-based features. Second, they can be computed very fast using *Integral Image*, which is much faster than convolution.

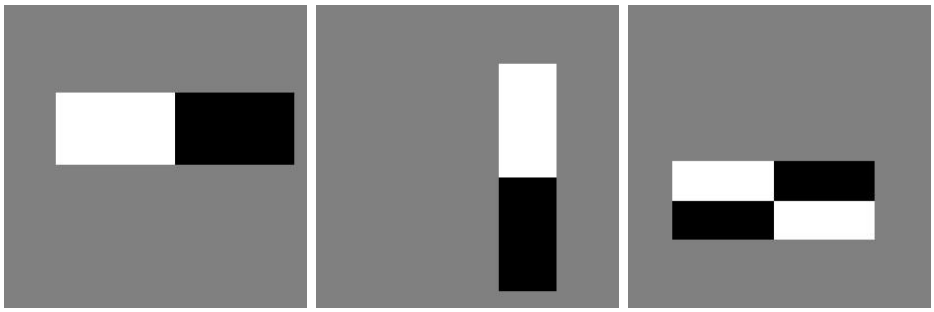

Figure 5.10: Example features. They are two-rectangle and four-rectangle features with different orientations. The white-colored pixels equal 1, the black-colored pixels equal -1, and the gray equal 0. In total there are 62208 features in a (24x24) sized image.

The Integral Image at pixel x, y is the summation of the pixels above and to the left of x, y, including x, y itself in the original input image, as seen in Fig. 5.11, 5.12:

$$ii(x, y) = \sum_{x' \leq x, y' \leq y} i(x', y'), \tag{5.15}$$

Where ii is the integral image and i is the original image.

The Attentional Cascade Detection

In the detection process, the input image is divided into a huge number of sub-images, *e.g.*, a 192x192 sized image is divided into more than 120,000 sub-images. If each sub-image goes through the strong classifier, which consists of hundreds or thousands of weak classifiers, the computation is expensive. Alternatively, I used the attentional cascade technique. This technique is based on three facts: 1st, the first few features in the strong classifier have relatively lower classifying error; 2nd, we can lower the

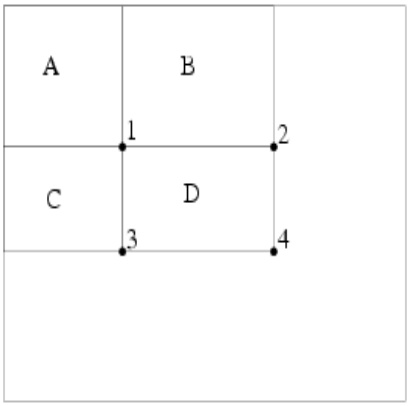

Figure 5.11: An illustration of integral image. Sum within rectangle $D = ii_4 + ii_1 - ii_2 - ii_3$.

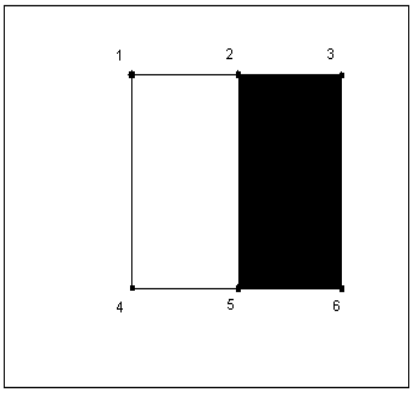

Figure 5.12: A feature example, whose filtered result $= ii_5 + ii_1 - ii_2 - ii_4 - (ii_6 + ii_2 - ii_3 - ii_5)$.

threshold of the weak classifier to achieve a very low false negative rate at the expense of an increased false positive rate; 3rd, most of the sub-images don't contain any heart. (Actually there should be only one optimal detection). Thus by using the first few weak classifiers, we can reject most of the sub-images, which saves a lot of time. Figure 5.13 is an example of the attentional cascade algorithm.

Detection Experiments and Results

In the experiment, the training data consist of 297 heart images and 459 non-heart images; the testing data consist of 41 heart images and 321 non-heart images. All

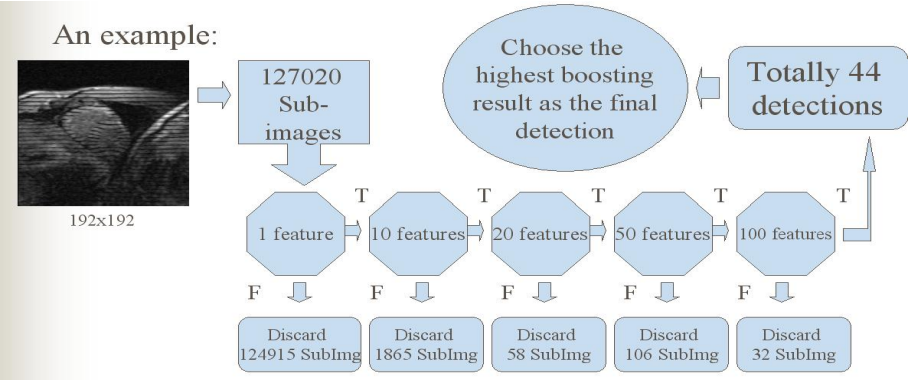

Figure 5.13: Five cascade stages with a total number of 100 features are used. At the first stage which consists of only one feature, 124915 out of 127020 candidate sub-images are rejected. At the second stage, 1865 sub-images are rejected, and so on. Finally in a certain image we have total 44 detections. The highest boosting result is chosen as the final detection. We can see during the first two stages, most sub-images are rejected, which makes the computation faster.

images are resized to 24x24 pixels and rotated to the same angle. Image intensities and contrasts are normalized. Figure 5.14 is a random sample from the heart training set.

The first few features Adaboost chooses are meaningful and easy to interpret. As shown in figure 5.15, the first five features mostly represent the boundary information of the heart, because the intensity inside the heart region varies too much and has no obvious patterns. Figure 5.16, 5.17 and 5.18 are a comparison of the error of the weak classifier, and the error of the strong classifier performing on the training data and the testing data.

After the final stage of the attentional cascade, the final detector usually produces a number of detections, because this strong classifier is insensitive to small changes in translation and scale. However, as we know, there can be only one heart in a image. So in the case of multiple detections, we have to discard most of the detections and keep only one that we are most confident in. We select the detection with the highest boosting result, which means it has the maximum margin and Adaboost is most confident that it is a heart. If we rotate the task image by a set of discrete angles before the detection procedure, and compare the probabilities across the discrete angles, we are also able to detect hearts in rotated images (see Fig. 5.19).

This heart detection algorithm using Adaboost works quite well. For the (41 positive

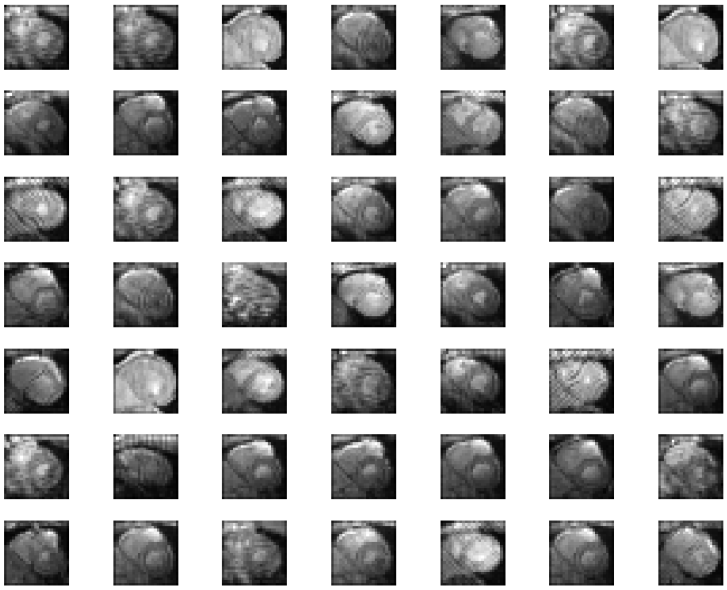

Figure 5.14: A random sample of the heart training set.

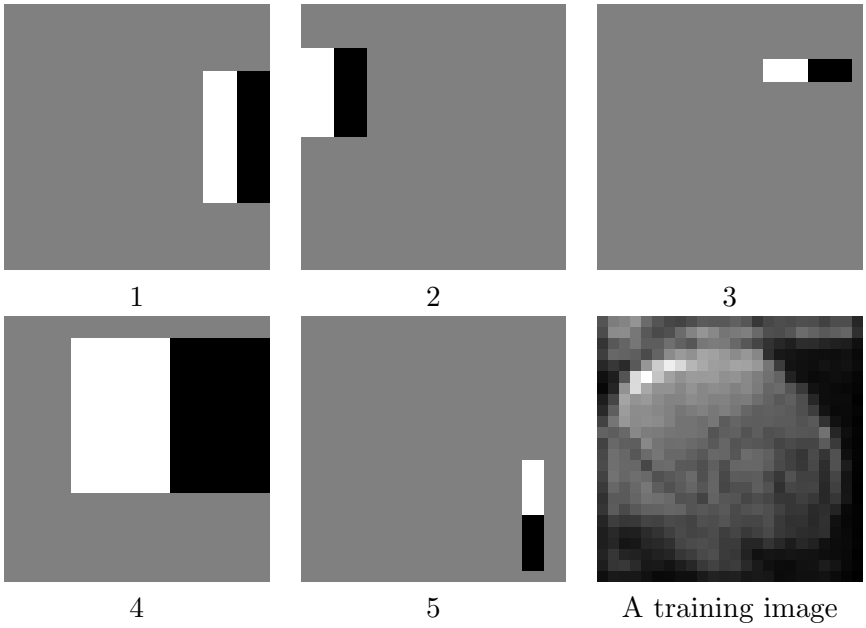

Figure 5.15: The first five features Adaboost selects compared with a training image.

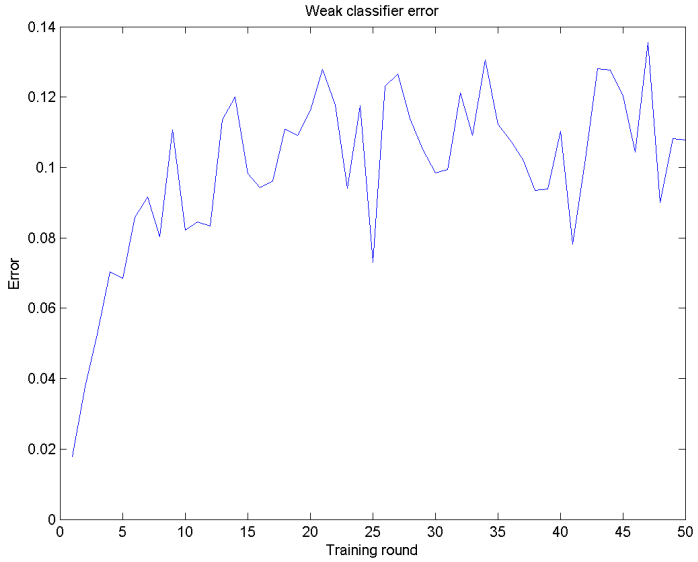

Figure 5.16: This figure shows the error of the weak classifier that Adaboost selects at each boosting round. The error increases non-monotonously as the distribution of the training examples becomes more difficult to classify.

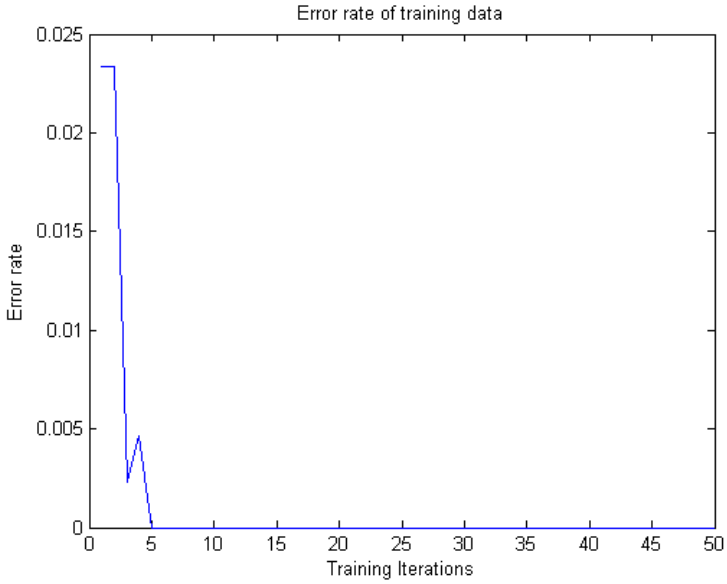

Figure 5.17: This figure shows the error of the strong classifier on the training data. The error drops to zero after five rounds.

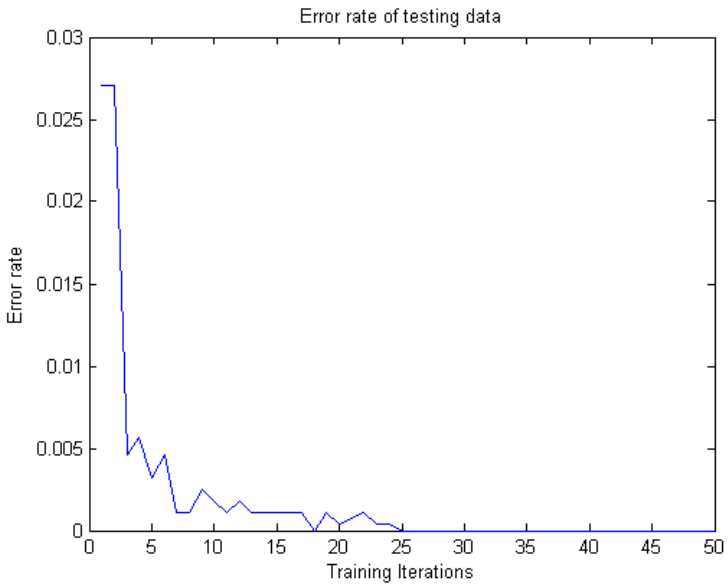

Figure 5.18: This figure shows the error of the strong classifier on the testing data. The testing error continues to decrease after the training error approaches zero, which means more iterations leads to larger margin and higher accuracy.

+ 321 negative)-sized testing data, our detector achieves a zero error rate.

5.2.4 Experimental Results and Validation

We applied our segmentation method to three data sets, one from the same subject and with the same imaging settings as the training data (but excluding the training data), and the other two novel data sets from two different subjects and with slightly different imaging settings. Respectively, the three data sets each contained 32, 48 and 96 tagged MRI images, with different phases, positions and tagging orientations. Each task image was rotated and scaled to contain a 80x80-pixel-sized chest-on-top heart, using the detection method before the segmentation. Each segmentation took 30 iterations to converge. Our experiment was coded in Matlab 6.5 and run on a PC with dual Xeon 3.0GHz CPUs and 2G memory. The whole learning process took about 20 hours. The segmentation process of one heart took 120 seconds on average. See Figure 5.20 for representative results.

For validation, we used the manual segmentation contours as the ground truth for the first and second data sets. For the third data set, because we don't have independent

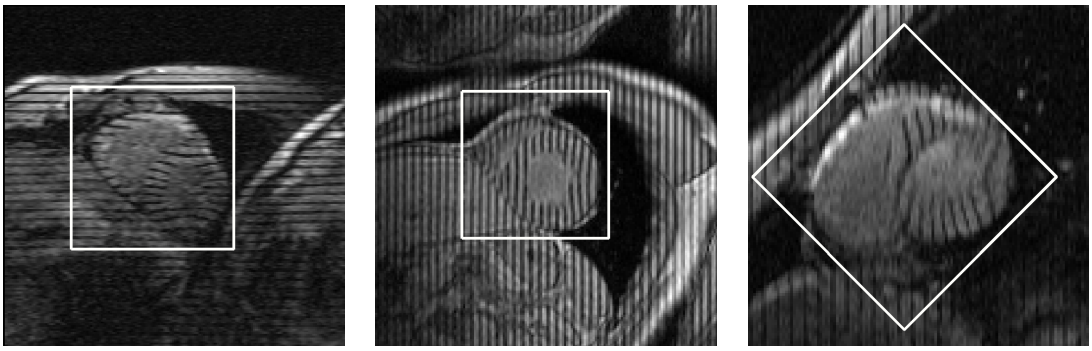

(a) (b) (c)

Figure 5.19: Three representative detection results. For image (c), the image was rotated by a set of discrete angles before the detection, and the final detection is of the highest probability among all the discrete angles tested.

manual contours, we used cross validation, since we know that at the same position and phase, the heart shapes in the vertical-tagged and horizontal-tagged images should be similar. We denote the ground truth contours as T and our segmentation contours as S. We defined the average error distance as:

$$\bar{D}_{error} = mean_{s_i \in S}(min||T - s_i||_2) \tag{5.16}$$

Similarly the cross distance is defined as

$$\bar{D}_{cross} = mean_{s_i^{vertical} \in S^{vertical}}(min||S^{horizontal} - s_i^{vertical}||_2) \tag{5.17}$$

In a 80x80 pixel-sized heart, the average error distances between the automatically segmented contours and the contours manually segmented by the expert of the first and second data set can be found in Table 5.1.

Table 5.1: Average error distances.

	LV (pixel)	RV (pixel)	Epicardium (pixel)
$\bar{D}_{error}$ (data set 1)	1.12	1.11	0.98
$\bar{D}_{error}$ (data set 2)	1.74	2.05	1.33

In the third data set, the cross distances can be found in Table 5.2.

Table 5.2: Average cross distances

	LV (pixel)	RV (pixel)	Epicardium (pixel)
$\bar{D}_{cross}$ (data set 1)	2.39	1.40	1.94

The larger distance in the cross validation arises in part from underlying misregistration between the (separately acquired) horizontal and vertical images. Thus, the true discrepancy due to the segmentation should be smaller. From the above quantitative results, we find that for a normal-sized adult human heart, the accuracy of our segmentation method achieves an average error distance of less than 2mm. The cross validation results of the third data set suggest that our method is very robust as well.

5.2.5 Discussion

In this section, we have proposed a learning scheme for fully automatic and accurate segmentation of cardiac tagged MRI data. First we developed a semi-automatic system to achieve efficient segmentation with minimal user interaction. Then the learning based framework has three steps. In the first step we learn an ASM shape model as the prior shape constraint. Second, we learn a confidence-rated complex boundary criterion from the local appearance features to use to direct the detected contour to move under the influence of image forces. Third, we also learn a classifier to detect the heart. This learning approach achieves higher accuracy and robustness than other previously available methods. Since our method is entirely based on learning, the way of choosing the training data is critical. We find that if the segmentation method is applied to images at phases or positions that are not represented in the training data, the segmentation process tends to get stuck in local minima. Thus the training data need to be of sufficient size and range to cover all possible variations that may be encountered in practice.

An interesting property of our method is that it is not very sensitive to the initialization conditions. As shown in Fig. 5.20, even if the initial contours are far away from the target position, it can still eventually converge to the right position after a few iterations. This property makes automatic initialization feasible. The detection method

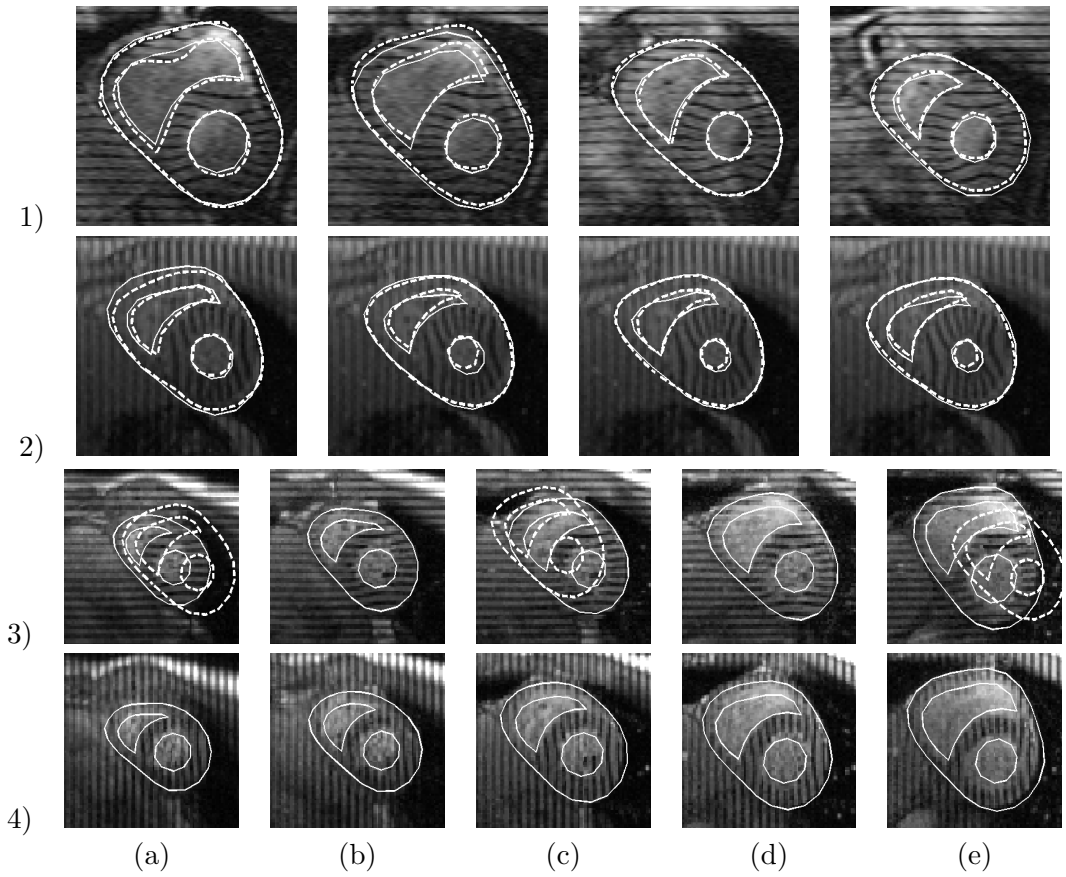

Figure 5.20: The first and second rows of images come from the the first and second dataset, respectively. For better representation, the images in the first row vary in position and remain at the same phase, while the images in the second row vary in phase but remain at the same position. The solid contours are from our automatic segmentation method; the dashed contours are manual. Notice that the papillary muscles in LV are excluded from the endocardium. The third and fourth rows are from the third dataset. Manual contours are not available for this dataset, so we compare our segmentation results between the the horizontal and vertical tagged images that are at same position and phase. Qualitatively, the contours are quite consistent, allowing for possible misregistration between the nominally corresponding image sets. In (3a), (3c) and (3e) the dashed contours are testing examples of poor initializations, while the final contours are solid. Although the initialization is far away from the target, the shape model moves and converges well to the target.

gives only a rough approximation of the heart's location and size, but it is good enough for our segmentation purposes.

5.3 Boosting and Nonparametric Based Boundary Tracking

5.3.1 Background

In this section, we will extend the previous section and formulate boundary segmentation as a tracking framework by adding the temporal information. It has been noted by several researchers that incorporating temporal information would greatly help the segmentation. When a human expert manually delineates the contours, it is common practice to watch the MRI images as a *movie* and use other frames and their motion to segment the current frame. Using this observation, in this section we propose a dynamic segmentation approach. Several methods in the MRI literature have used temporal information to help segmentation. Sun *et al.* [85] proposed a segmentation and tracking method for the left ventricle by learning the ventricle dynamics. In [86], tracking of the myocardium is embedded in a nonrigid image registration framework. More myocardial boundary tracking methods can be found in the echocardiography literature. Comaniciu *et al.* [87, 88] proposed a multi-model information fusion framework to achieve robust myocardial boundary tracking. In [89, 90] shape-space based or contour-matching based approaches are proposed.

In this section, we introduce a new framework for boundary tracking of short axis (SA) tagged MRI sequences, including the boundary contours of the endocardium of the left ventricle (LV), the endocardium of the right ventricle (RV) and the epicardium. In this framework, in order to find strong image features, instead of visually tracking the contour points via profile matching or optical flow related methods, we learn a more complex boundary criterion using AdaBoost. Contour profile consistency between two consecutive frames (the motion feature) is an important feature in tracking, but it has limitations in handling the inherent appearance changes due to tag fading and myocardial deformation, especially the boundary's tangential movement (such as rotation and sliding, see Fig. 5.22b) and myocardial motion through the imaging plane. Using

the boosting algorithm, we demonstrate that for more accurate boundary feature extraction, the local boundary appearances in the current frame (the static feature) are also important. The AdaBoost algorithm gives a natural way to combine both features and generate better boundary criteria. Furthermore, through boosting error analysis, we find the confidence ratings of each criterion and calculate the posterior probability density function of the shape model. In order to lower the dimensionality and constrain the shape variations, we project the shape into a Principal Component Analysis (PCA) subspace [74], and update the PCA parameters instead of the contour points' positions. Since the heart motion has a cyclic contraction and expansion pattern, which exists in both normal and diseased hearts, we treat the systole and diastole separately and find two motion prediction matrices and error covariance matrices via multivariate linear regression. We embed the shape tracking into a nonparametric-based sequential particle filtering framework [91] for its ability of contour tracking through heavy clutter.

Our overall learning and tracking framework is outlined by the flow-chart in Fig. 5.21. Our experimental results show the accuracy and effectiveness of the proposed algorithm.

5.3.2 Methodology

Shape Modeling and Boosting The Boundary Criteria

The shape model is the same as described in the previous section. It is a PCA linear model that is represented by 50 ordered landmark points. Any heart shape can be approximately modeled by $X = \bar{X} + Pb$, where $\bar{X}$ is the mean shape vector, P is the matrix of shape modes, and b is the vector of shape parameters weighting the shape variations.

To reliably and accurately track the myocardial boundary, we try to use all possible image cues, including the static features and the motion features, to make a strong boundary criterion. This cue-integration is performed by Adaboost. Adaboost is a well known classification algorithm [75] that incrementally selects a small number of important features from a huge potential feature set and creates a linear combination of them as an accurate strong classifier. In the learning stage, given training data

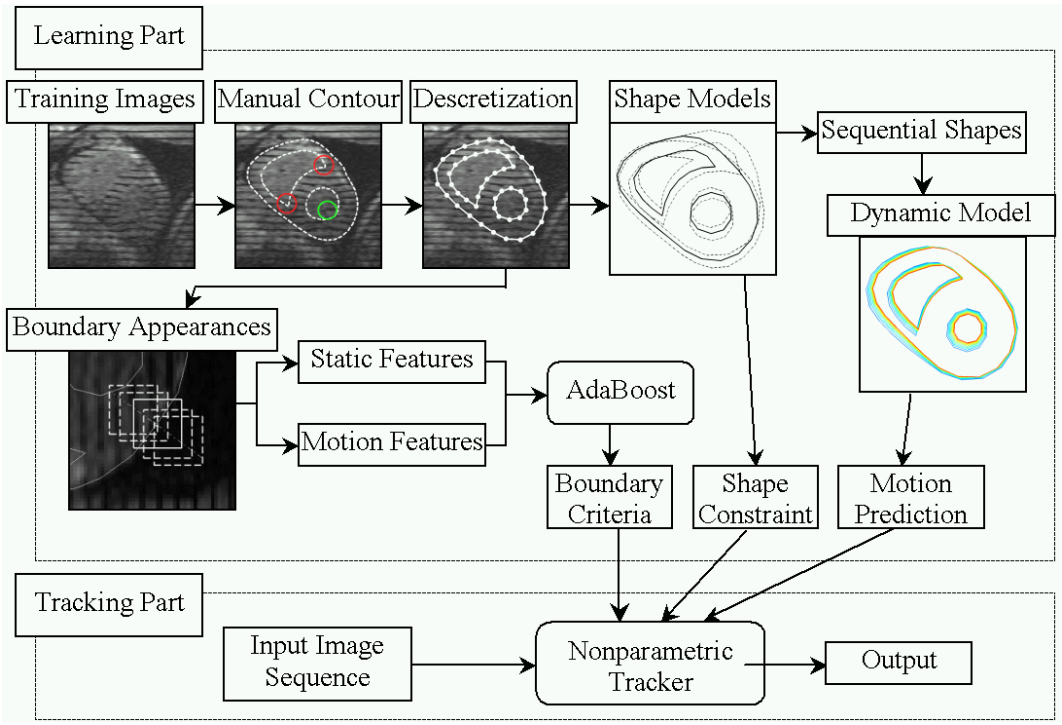

Figure 5.21: The flow chart of our proposed framework illustrates the learning and tracking processes. In the manual contour block, the red circles indicate the cusp points between the septum and the RV endocardium. The green circle indicates the location of papillary muscle. In the dynamic block, cooler color turning into warmer color indicates the dynamic model's evolution during systole.

$(x_1, y_1)...(x_m, y_m)$, where $x_i \in X$, $y_i \in \{0, +1\}$, during the boosting process, each iteration selects one feature, i.e., a weak classifier, h_t from the total potential features pool, and combines it (with an appropriate weight α_t) with the existing classifier that was obtained in the previous iterations.

$$h_t : X \rightarrow \{0, +1\} \tag{5.18}$$

$$F = \Sigma_t \alpha_t h_t(x) \tag{5.19}$$

After t iterations, the linear combination of the selected important features F makes a stronger classifier $H(x)$ with higher accuracy. We denote $\Gamma = \Sigma_t \alpha_t / 2$ as the threshold value for F. For a new input data x to be classified, if $F > \Gamma$, H classifies x as positive,

and vice versa.

$$H(x) = \frac{Sign(F - \Sigma_t \alpha_t / 2)}{2} + \frac{1}{2} \tag{5.20}$$

We perform Adaboost boundary learning at each landmark point on the shape model. Thus the boundary criteria vary according to each model point's location. In order to embed the Adaboost $\{0, 1\}$ classifier into the sampling-based tracking framework, we need to extend it to a probability representation. Influenced by [77], we use a logistic function to estimate the probability of a point x_k, along with its local appearance patch, being on the boundary at the location of landmark point k, with a normalization term Γ_k the same as the threshold value:

$$Pr(y_k = +1|x_k) = \frac{e^{F_k(x_k)/\Gamma_k}}{e^{F_k(x_k)/\Gamma_k} + e^{-F_k(x_k)/\Gamma_k}} \tag{5.21}$$

After the training process, Adaboost provides the error rates e_k on the testing data. We define the confidence rating of the boundary criterion at point k as:

$$c_k = \ln \frac{1}{e_k}; \tag{5.22}$$

Intuitively, when c_k is big, we trust its probability prediction $Pr(y_k = +1|x_k)$ more. We incorporate the confidence rating into the probability $Pr(y_k = +1|x_k)$ as a posteriori knowledge. Then the probability density function of the shape model is estimated by:

$$p(Y = +1|X) \propto \prod_k \frac{e^{F_k(x_k)c_k/\Gamma_k}}{e^{F_k(x_k)c_k/\Gamma_k} + e^{-F_k(x_k)c_k/\Gamma_k}} \tag{5.23}$$

The boosting algorithm investigates a large number of weak feature candidates. At each landmark point on the shape contour, the local appearance features are captured by filtering methods in both static and motion cases.

To capture the static local appearance features, we design three different kinds of steerable filters. We use the derivatives of a 2D Gaussian to capture the edges, we use the second order derivatives of a 2D Gaussian to capture the ridges, and we use half-reversed 2D Gabor filters to capture the tagging line breakpoints.

The half-reversed 2D Gabor filters are defined as a 2D sine wave multiplied with the one directional derivative of a 2D Gaussian:

$$F = G'(x, y) \cdot \mathbb{R}\{e^{-j[\phi+2\pi(Ux+Vy)]}\} \tag{5.24}$$

where G' is the derivative of a 2D Gaussian. U and V are the frequencies of the 2D sine wave, and ϕ is the phase shift.

To capture the motion local appearance features, we measure the intensity consistency between two consecutive frames. In order to avoid the effect of boundary tangential motion, before comparison, a set of Gaussian filters are designed to blur the boundary local patch in a certain orientation and scale (See Fig. 5.22(b).

For a 15x15 sized filter patch, by tuning the filters' scale, orientation and frequency, we designed 1840 static filters and 121 motion filters in total. See Figure 5.22(a) for some sample static filters.

In the manually segmented images, at each landmark point of the contours, a small image patch around it is cut out as a positive appearance training sample for this particular landmark point. Then, along the normal of the contour, on each side of the point, we cut out another two patches as the negative appearance training samples for this particular landmark point. (See boundary appearance box in Fig. 5.21) For motion features, the consistencies are measured between the current frame sample with the positive sample in the previous frame.

After the training process, the classification error rates on the testing data give the measurement of the boosting performance. After 50 Adaboost iterations, we find that the error rates using both static and motion features are much lower than using either static or motion features alone. See Figure 5.23. This comparison validates our boundary tracking scheme based on both motion and static features.

Nonparametric Shape Tracking

Sampling-based tracking algorithms have the ability to handle contour tracking problems with non-Gaussian probability density functions (pdfs). Our tracking method is

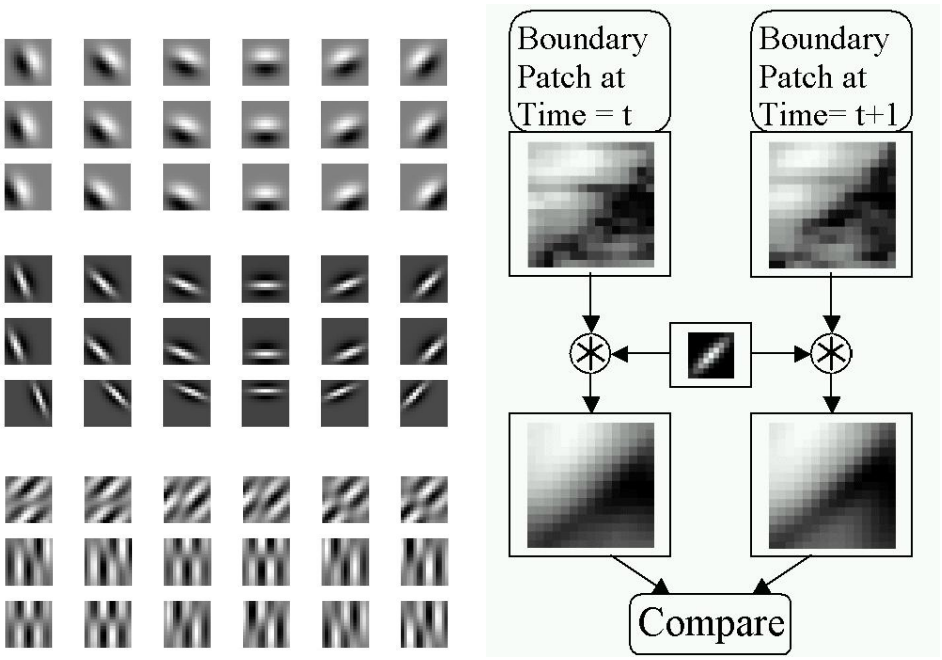

(a) (b)

Figure 5.22: (a) shows 3 sample sets of static feature filters, from top to bottom, the derivatives of Gaussian used for edge detection, the second derivatives of Gaussian used for ridge detection, and the half-reversed Gabor filters used for tag line breakpoint detection. (b) illustrates the function of the motion feature filter, which helps remove the tangential motion.

based on a nonparametric particle filtering approach [91], where the pdf is represented by factored sampled particles.

During myocardial wall tracking, we use a state vector s to represent the shape model. $s = [c, \theta, t_x, t_y, b]$, where c is a scaling factor, θ is the orientation angle, (t_x, t_y) is translation, and b is a 12-D variation vector of the PCA shape modes. The myocardial wall tracking algorithm based on particle filtering is as in Table 5.3.

There are two main difficulties in implementing the algorithm. The first one is how to find a proper dynamic model. The second is how to decide the sampling size N.

The motion pattern differs greatly among human hearts, especially between the normal and the diseased. Our strategy is to find a common dynamic model whose constraint is loose but can help in decreasing the sampling range. Since the tagged MRI sequences are acquired with an ECG trigger, we are able to locate the end systolic

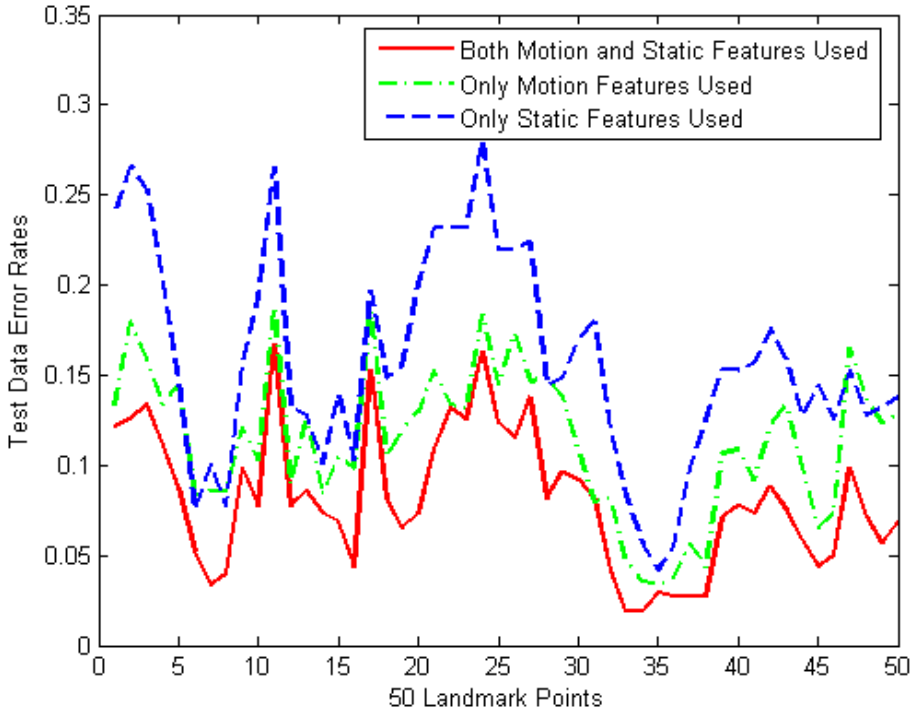

Figure 5.23: The testing error rates of the boundary criteria boosting. The red curve which integrates both motion and static features has lower error rates than the other two.

(ES) frame. We train the dynamic model based on systole and diastole separately. For a given state vector $s^{(t)} = [s_1^{(t)}, s_2^{(t)}, ..., s_n^{(t)}]'$ at time t, we make an assumption that it can be approximated by a linear transform of $s^{(t-1)}$.

$$s_i^{(t)} = a_0 + a_1 s_1^{(t-1)} + a_2 s_2^{(t-1)} + ... + a_n s_n^{(t-1)} + N(0, r_i^2) \tag{5.25}$$

This is a multivariate linear regression problem. We solve it to get $A_i = [a_0, a_1, ..., a_n]$ as the prediction vector of s_i and r_i^2 as the error variance. Then the conditional probability of the prediction dynamic model is:

$$p(s_i^{(t)}|s^{(t-1)}) = \frac{1}{\sqrt{2\pi} r_i} \exp\{-(s_i^{(t)} - A_i \cdot s^{(t-1)})^2 / 2r_i^2\} \tag{5.26}$$

The sampling size N is empirically set. For 12 sequences of the testing data, we find the tracking typically stops improving after $N \geq 1000$. Thus we set $N = 1000$.

Table 5.3: Myocardial wall tracking algorithm

1. Suppose the total sample number is N, total time frame number is T. At $time = 1$, $s_1^{(n)}$ is initialized as the manual contour shape at the first frame. Weights $\pi_i^{(n)} = \frac{1}{N}$.
2. For $time = 2 : T$,
   Factored draw samples $s'^{(n)}_t$ from s_{t-1} based on the weights $\pi_{t-1}^{(n)}$.
   Predict new $s_t^{(n)}$ by sampling from a dynamic model $p(x_t|x_{t-1}) = s'^{(n)}_t$.
   Measure and weight the new shape in term of the measurement y_t by Eq. 5.23. $\pi_t^{(n)} \propto p(Y_t|X_t = s_t^{(n)})$, and $\sum_n \pi_t^{(n)} = 1$
   Estimate the solution via the strongest local mode.
   End for

5.3.3 Experimental Settings and Results

We acquired 50 time sequences of short-axis tagged MR images from 5 normal subjects and 3 patients. Each sequence contains 12 to 18 frames (images). In total, we collected 776 images. The spatial positions of these SA images vary from near the ventricle apex to near the ventricle base, but their topologies, only one LV and one RV, are consistent. The tagging line orientations are either 0°, 90° or ±45°. An expert was asked to segment the epicardium, the LV endocardium and the RV endocardium from the images. The manual segmentations were used as the training data, as well as the ground truth in validation based on a leave-6-out scheme, in which each time 44 sequences were grouped as the training data while the other 6 were used for testing. If two sequences were taken from the same subject and at the same spatial position, but with different tag orientations, we grouped them in the same training or testing set. In this way, we strictly separated the training and testing data.

Each training image is rotated and scaled to contain a 80x80-pixel image of the heart with the interior chest wall on top. The size of the boundary appearance patches is set to 15x15 pixels. In the tracking process, the initial contour is set semi-automatically [92], allowing manual correction. Our algorithm implementation is coded in Matlab 6.5 and runs on a 3GHz PC workstation. For a tracker with a sampling size of 1000, it takes 60 seconds to track a frame on average.

See Fig. 5.24 for some representative tracking results. Since the resulting contours are represented by 50 landmark points, we measure the tracking error by calculating the

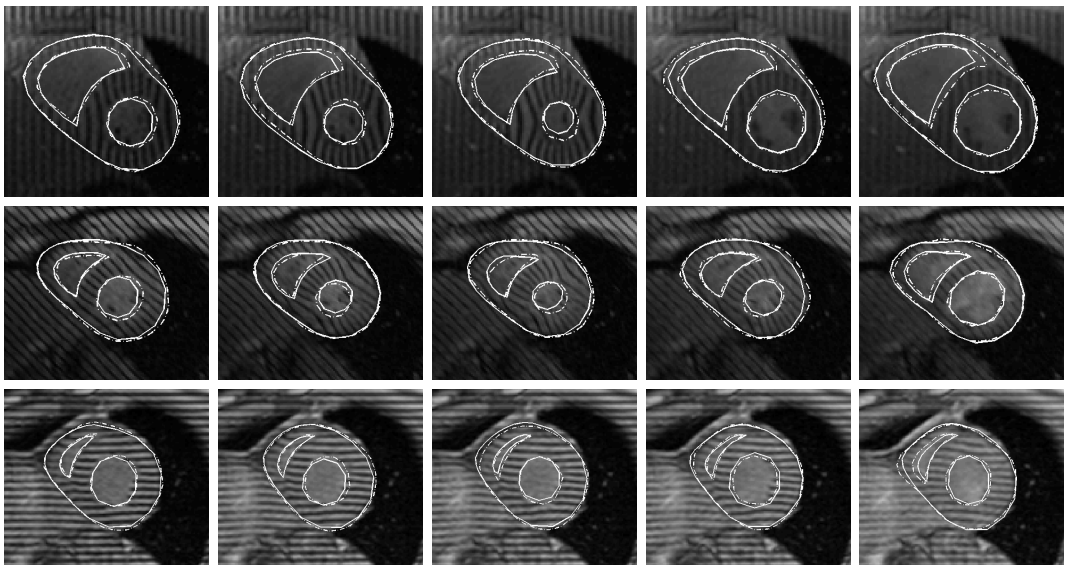

Figure 5.24: Snapshots from three example sequences of our experimental results. The solid contours are from our tracking method, while the dashed are from manual segmentations. The first 2 rows are data from 2 normal subjects. The last row is from a patient with heart failure. Note that our tracking method can exclude the papillary muscle from the ventricle endocardium, and always keep the cusp points at the RV-LV junctions.

distances from the landmark points s_i to the expert's manual contour C: $error(s_i, C) = min_{c_i \in C} \parallel s_i - c_i \parallel$. Fig. 5.25 shows the mean error in pixels for each time sequence; the mean error for the LV. RV and epicardium are also drawn. In Table 5.4 some error analysis are performed in millimeters.

5.3.4 Discussion

In this section, we have proposed a tracking framework for tagged MRI. Our method integrates the boundary appearance (both static and motion), the shape constraints and the dynamic model naturally in a boosting and nonparametric tracking framework. We strictly test the algorithm on data that are excluded in the training set. The experimental results show the accuracy. With the error analysis shown in Table 5.4, we find that in general we have achieved sub-millimeter accuracy while MRI resolution is approximately $1mm$. Our method works slightly better on the mid-ventricle slices and on normal hearts. In the future we will train more shape and motion models for

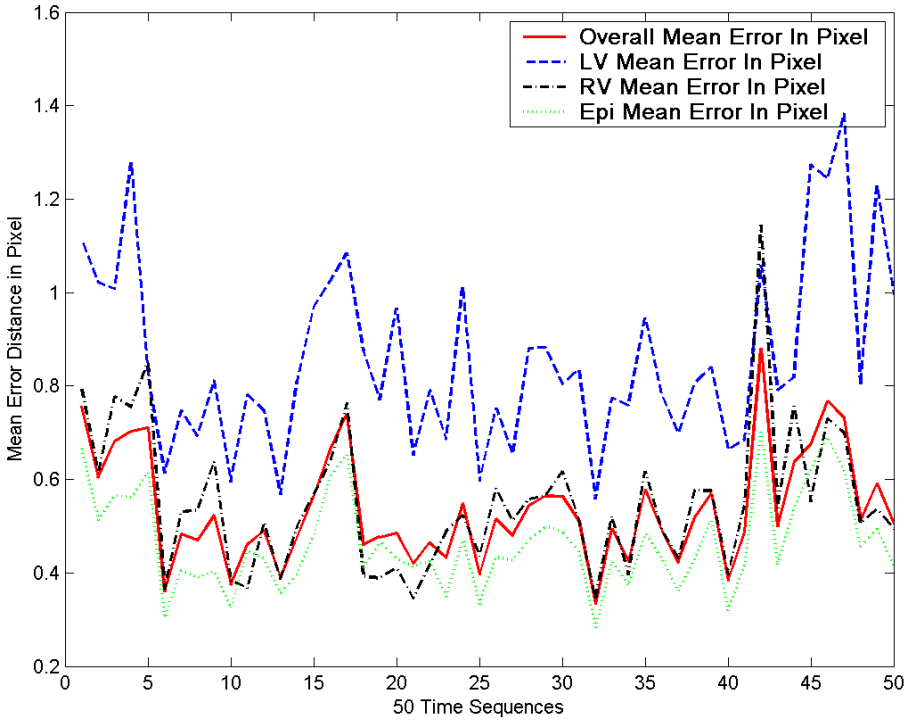

Figure 5.25: The mean error for each time sequence measured in pixel. The red solid curve represents the overall error. The blue dashed, black dash-dot and green dotted curves represent the mean error distances in the LV, RV endocardium and epicardium respectively.

different slice positions and extend up to the valve region, where the RV separates into distinct inflow and outflow regions. We will also extend the method by training on different diseases, where the shape and motion of the patient data can be very different from the normal (see the last row of Fig. 5.24, which is from a patient with heart failure).

5.4 Conclusion

In this chapter, we presented two boundary segmentation frameworks for tagged MRI. The 4D spatio-temporal propagation-based segmentation framework is a semi-automatic approach. The MetaMorphs segmentation method is implemented on tag-removed images. Then segmented contours are propagated spatio-temporally to the whole 4D image data set, using myocardial tracking and spatial key frames. Based on this method, we

Table 5.4: Error analysis in millimeters.

	$\bar{error}(mm)$	$\bar{\sigma}(mm)$
LV	1.24	0.66
RV	0.79	0.81
Epicardium	0.67	0.91
Near Base	0.77	0.89
Mid	0.71	0.81
Near Apex	0.87	0.99
Normal	0.76	0.86
Patient	0.89	1.03

developed a software system that can efficiently process images of full 4D data sets. It has a user-friendly computer-user interface that allows manual interactions. The advantage of this system is that the spatio-temporal propagation strategy speeds up the whole segmentation process, and the user can easily make corrections and achieve the desired segmentation results using the user interface. The disadvantage of this method is that it is not fully automatic. Manual interaction takes time.

The learning-based segmentation is fully automatic. We learn the shape, the appearance, and the motion pattern from a set of training data. The user does not need to input any parameters or make any interactions. The main disadvantage of this method is that the performance of this method totally relies on the completeness of the training data. If the input image to be segmented has a big variation in shape, appearance or motion, and has no similar representatives in the training data, this learning based method might fail.

In practice, we use the first method to generate a large number of training data for the second method. Once we segment new images by using the second method, we also allow the user to make corrections by loading the results onto the first system and using the user-interface.

Chapter 6

Strain Estimation and Regional Cardiac Function Analysis

6.1 Introduction

Many cardiovascular diseases, such as ischemia and infarction, are associated with the alteration of the global or local contractility of myocardium. Accurately assessing the detailed myocardial deformation, such as the estimation of the local strain values, could be critical for the early diagnosis of cardiac diseases and dysfunctions.

The technique of tagged MRI acquires short axis and long axis images at different positions to capture the 3D motion of the heart. As long as the tagging pattern is dense enough to capture the myocardial deformation, and the imaging planes are dense enough in covering the whole heart, we are able to estimate the 3D deformation and strain values of the whole heart. However, 3D strain estimation methods have been mainly applied on the ventricles, because the atrial muscle is so thin that tagging technique cannot place enough tagging patterns inside the atrial muscle. In [45, 46, 48], several researchers in our group have developed a generic bi-ventricle Finite Element Model (FEM) to estimate 3D ventricular deformation and strain. In their method, the cardiac boundary segmentation results are used to fit the generic FEM model onto the real heart data. The tagging lines or grids are used as landmark points, which are registered to each FEM element. Then the tracking results of the tagging lines or grids are used to deform the FEM model. The 3D deformation and strain estimation can be obtained by solving the FEM, i.e., the model converging to the desired shape when the external forces diminish to zero and the residual motion is negligible. In [47, 48], cardiac stresses and fiber orientations are obtained from the strain estimations using an EM scheme.

In imaging acquisition process, tMRI requires the patients to remain in still positions

and hold their breaths for up to about 30 seconds at a single imaging position. In order to acquire a full 3D tMRI scan that is dense enough to reconstruct the 3D FEM model and calculate the complete 3D ventricular strains, it can be necessary to acquire images at up to about 20 imaging positions, which makes the whole acquisition process last about 45-60 minutes. Although 3D modeling is desirable to estimate and analyze 3D ventricular strains, currently it is not clinically practical for patients with heart diseases, who would have difficulties to stay still inside the MRI machine for such a long time. Therefore, in clinical practice, the radiologists will choose a faster and more economical way. Rather than a whole 3D scan, they only acquire 2D images at a limited number of imaging positions that are likely to show the presence of heart diseases. Estimating 2D deformation and strain in single a 2D image can be more relevant in clinical applications.

In this chapter, we will develop both tracking and non-tracking-based strain estimation methods for 2D tMRI. We will also develop an inter-modal registration algorithm that makes ultrasound elastography and tMRI comparable. In the last section of this chapter, we will develop a tensor-based classification algorithm to detect and localize myocardial abnormalities from the strain and motion estimation.

6.2 Tracking Based Strain Estimation in 2D tMRI

We focus on developing 2D strain estimation and analysis methods. In continuum kinematics, strain can be formulated as the derivative of displacement. Many researchers have proposed tracking-based methods to first derive myocardial displacement. Then strain can be calculated from the displacement field. In [49], deformed tags are tracked and interpolated using a spline method to obtain the displacement map. Then the 2D Lagrangian strain is calculated from the horizontal and vertical displacement maps. In [93], 3D strain is derived from a 3D displacement map.

6.2.1 In Case of 1D Tagging Lines

As described in Chapter 3, we implement a set of free-end Snakes to track the 1D tagging lines. Tagging lines are straight lines at time 0. They are equally spaced at

an interval of $1/\sqrt{(U^2+V^2)}$. Starting from time 0, we keep tracking the tagging lines only *within the heart wall* using the results of the boundary segmentation. The tagging lines' model is basically a set of *Snakes* whose external forces are from the original intensity images and the tag-enhanced images. The internal forces are used to regulate the curvatures within each single Snake, and the distances between Snakes.

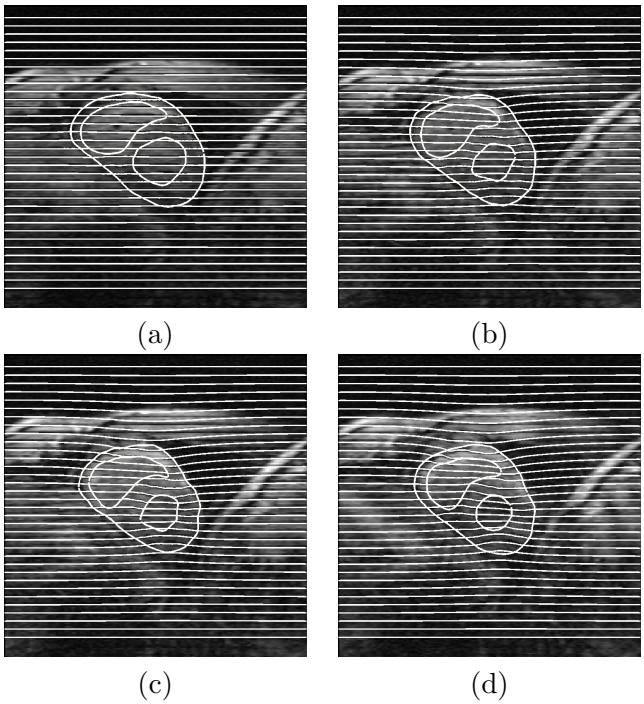

Figure 6.1: Four sequential tracking examples (a to d) during systole.

6.2.2 In Case of 2D Tagging Grids

For 2D tagging grids data, we implemented a template-based tracking algorithm on a 2D grid-shaped mesh to obtain the displacement vectors of the crossing points (or nodes) on the tagging grids (Fig. 6.2). Each crossing point (or node) on the mesh is tracked by calculating the similarity between templates, which are modeled using two tunable Gabor filters and the underlying images. The crossing points on the mesh are driven iteratively by forces from the neighboring image patches, whose texture patterns are the most similar to a reference template. The coordinates of the crossing points in a time sequence are further smoothed by a cubic spline function.

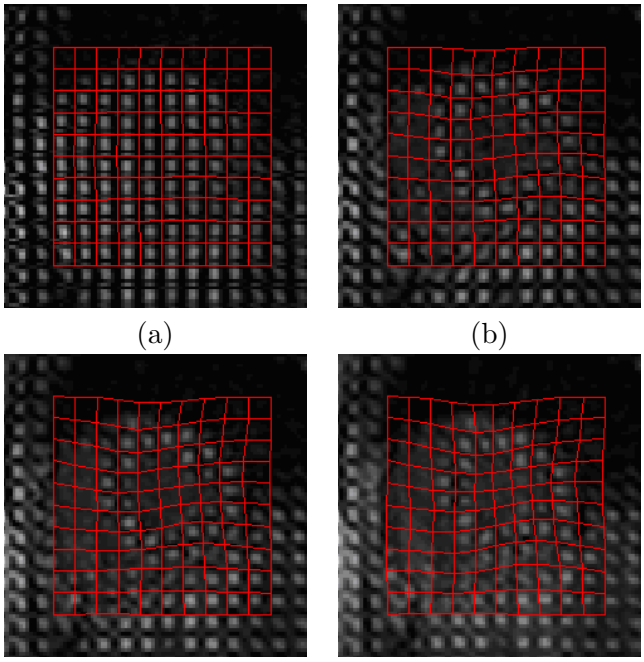

Figure 6.2: Four sequential tracking examples (a to d) during systole. Note that only the nodes inside the myocardium are tracked by spline-based method.

6.2.3 Strain Calculation From Tracking

After we track the tagging lines or grids, the displacements of the line nodes or grid nodes can be calculated through subtraction. Finally, a cubic B-spline-based method is used to interpolate the line or grid nodes in 2D to obtain the entire displacement distribution within the myocardium.

Strain is defined in terms of the gradient of the displacement. A displacement vector $\mathbf{u}$, is written as $\mathbf{u} = u_x\mathbf{e}_x + u_y\mathbf{e}_y$, where u_x and u_y are horizontal and vertical displacement components, respectively, and $\mathbf{e}_x$ and $\mathbf{e}_y$ are the unit vectors in the horizontal and vertical directions, respectively. The displacement gradient tensor $\mathbf{G}$ in Cartesian coordinates (x, y) is thus defined as $\mathbf{G} = \nabla\mathbf{u}$.

$$\mathbf{G} = \nabla\mathbf{u} = \begin{bmatrix} \frac{\partial u_x}{\partial x} & \frac{\partial u_x}{\partial y} \\ \frac{\partial u_y}{\partial x} & \frac{\partial u_y}{\partial y} \end{bmatrix} \tag{6.1}$$

The in-plane Lagrangian finite strain tensor, $\mathbf{E}$, is formulated as in [94]:

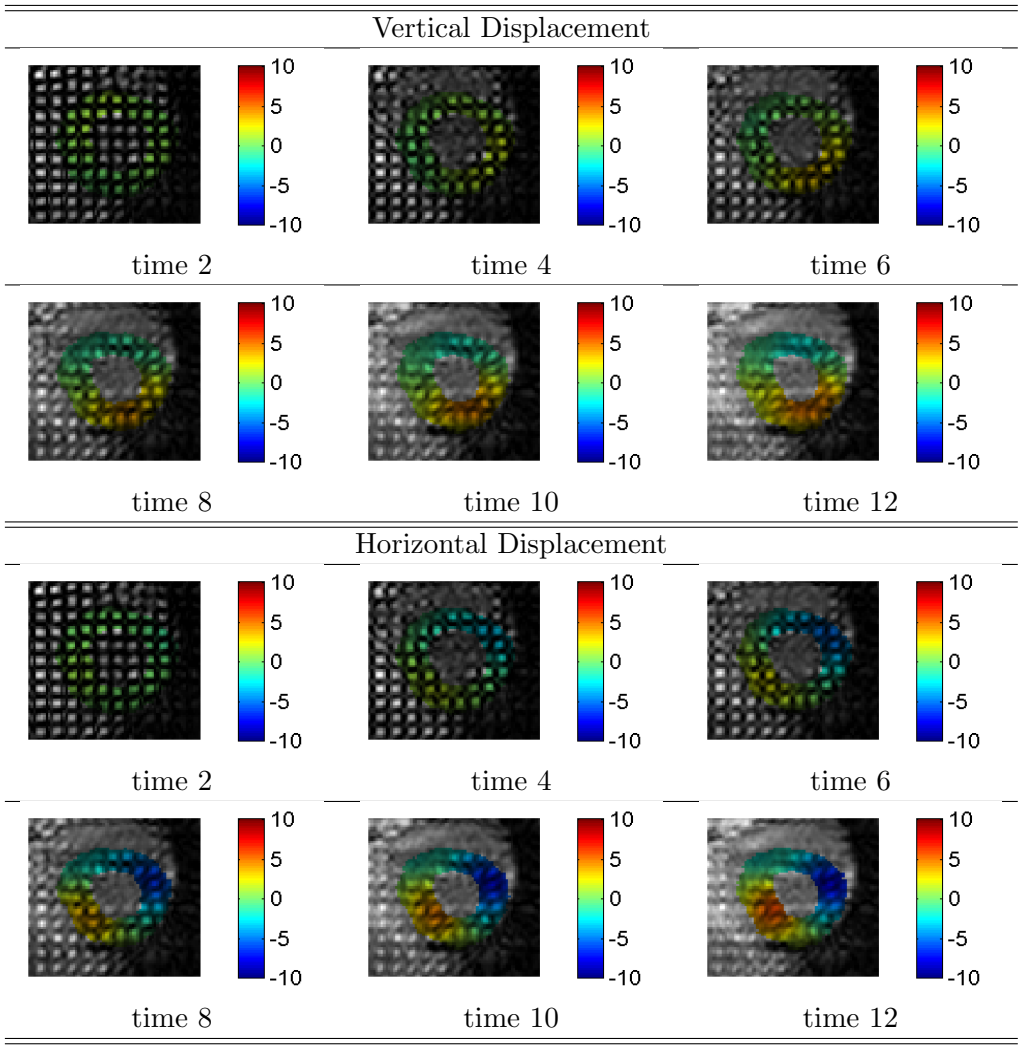

Figure 6.3: Displacement in vertical and horizontal coordinates.

$$\mathbf{E} = \frac{1}{2}(\mathbf{G} + \mathbf{G}^T + \mathbf{G}^T\mathbf{G}) \tag{6.2}$$

Horizontal and vertical strains are the diagonal components of $\mathbf{E}$, i.e., $\mathbf{E}_{xx}$ and $\mathbf{E}_{yy}$, respectively. The off-diagonal terms are related to the corresponding sheering strains.

The above mentioned 2D (or, vertical and horizontal) Lagrangian finite strains are dependent on the myocardial locations with respect to the centroid of the ventricle. This angle-dependence may complicate the interpretation of the myocardial deformation in the left ventricle. Therefore, radial and circumferential strains are obtained by defining an angle, θ, about the centroid of the left ventricle and by transforming the finite

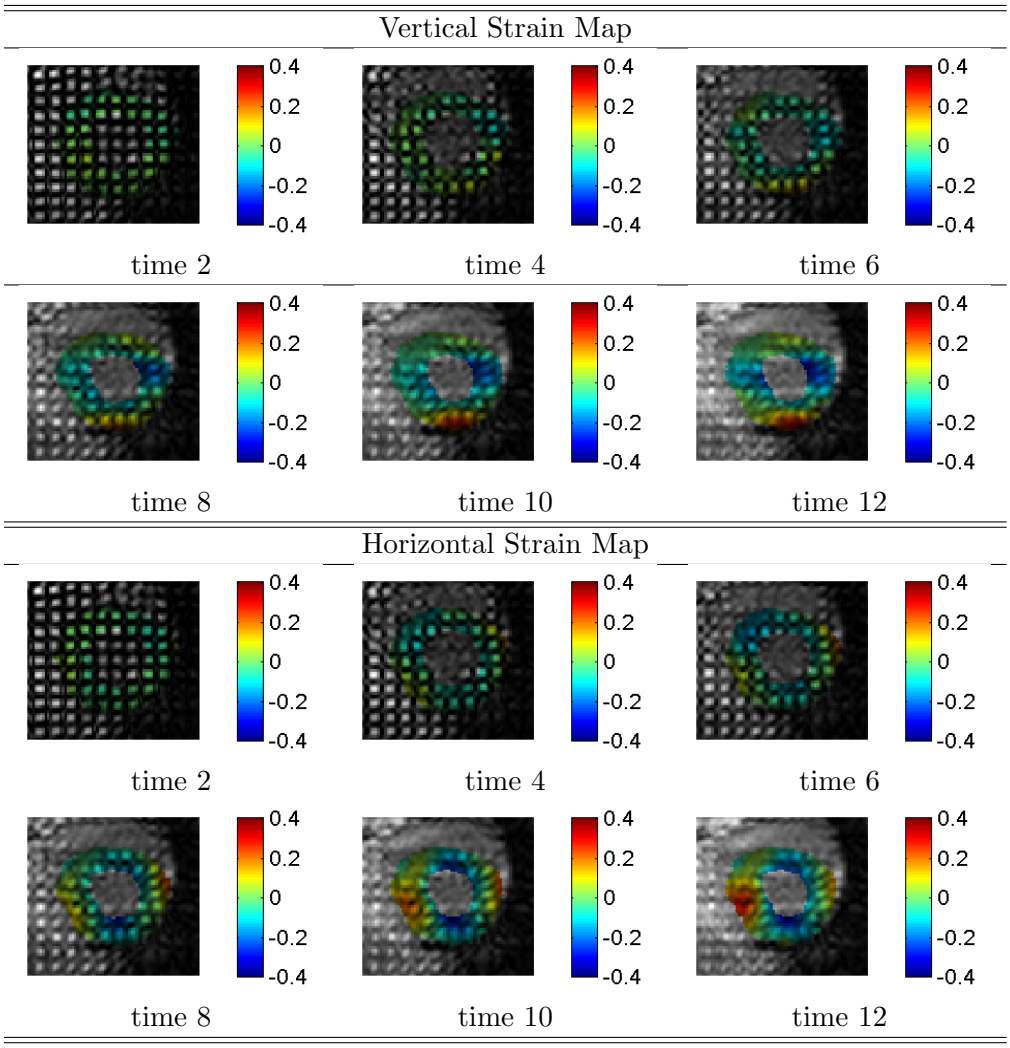

Figure 6.4: Strain map in vertical and horizontal coordinates.

strain tensor $\mathbf{E}$ into a radial-circumferential strain tensor $\dot{\mathbf{E}}$ with a rotation matrix $\mathbf{Q}$: $\dot{\mathbf{E}} = \mathbf{QEQ}^T$ [94].

$$\dot{\mathbf{E}} = \mathbf{QEQ}^T, \qquad where, \qquad \mathbf{Q} = \begin{bmatrix} \cos\theta & \sin\theta \\ -\sin\theta & \cos\theta \end{bmatrix} \tag{6.3}$$

Positive and negative radial strains indicate myocardial thickening and thinning, respectively, while myocardial stretching and shortening are represented by positive and negative circumferential strains, respectively.

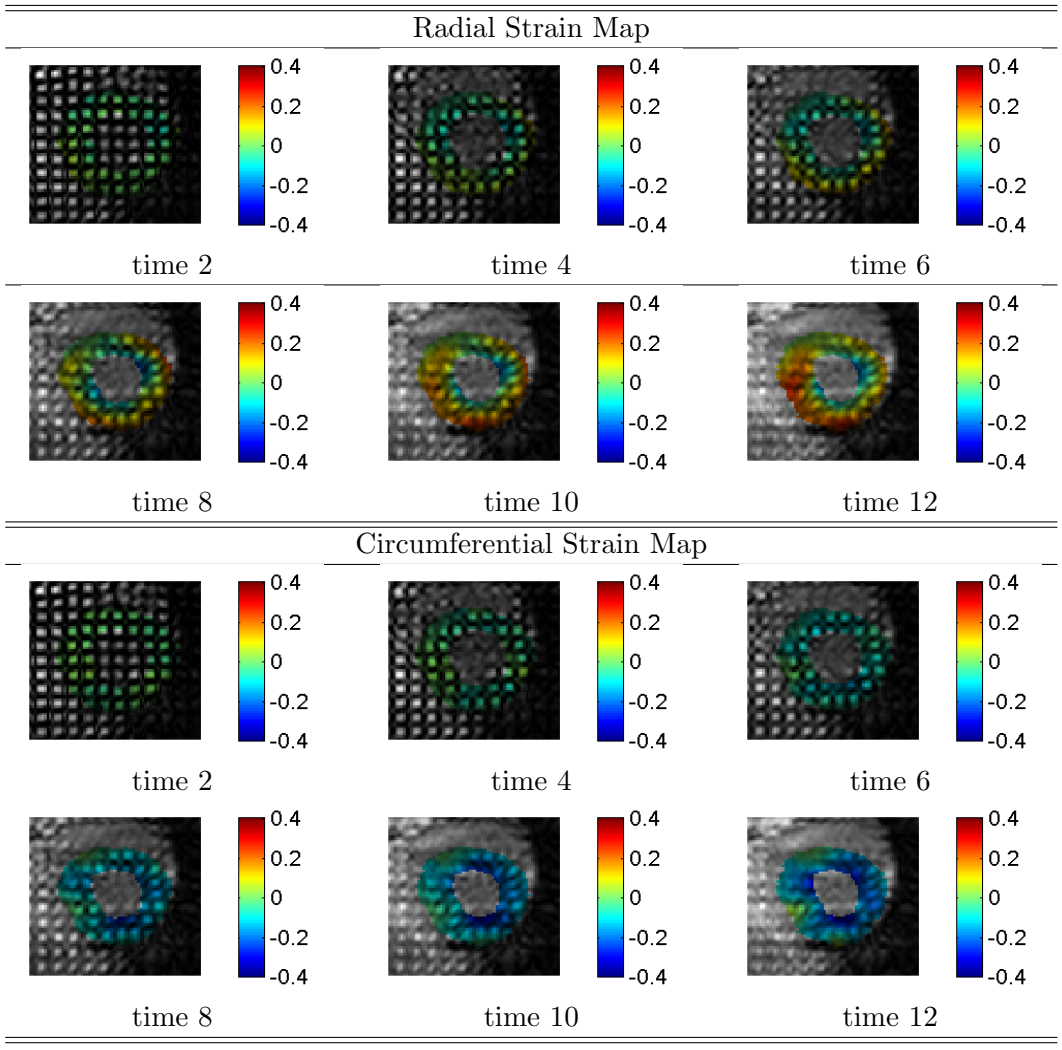

Figure 6.5: Strain map in radial and circumferential coordinates.

6.3 Comparison With Registered Ultrasound Myocardial Elastography

Ultrasound Myocardial Elastography (UME) is a radio-frequency (RF) based speckle tracking technique [95]. Despite the low SNR nature of ultrasound signals, echocardiography enjoys widespread availability in the clinic, as well as its relatively low cost and high temporal resolution. In UME, the two in-plane orthogonal displacement components (lateral and axial) are estimated using 1D cross-correlation and recorrelation of RF signals in a 2D search [96]. Then, the incremental displacements are integrated to

obtain a cumulative motion estimation.

Tagged MRI is currently considered the most accurate noninvasive myocardial motion and strain estimator. Several studies have compared the estimates from ultrasound with those from tMRI. Notomi et al. [97], Helle-Valle et al. [98] and Cho et al. [99] have demonstrated that left-ventricular torsion measured from B-mode-based speckle tracking methods is consistent with that from tMRI in short-axis (SA) views. In [100] 2D motion and strain estimates from UME are shown to be highly comparable with those from tMRI. However due to the different characteristics of ultrasonic imaging and tMRI, a main limitation of these comparisons is that the two modalities are not registered in 3D. Thus, the ultrasound and tMR images may not be acquired at the same SA slice with the same orientation. To address this potential discrepancy, in this paper we have developed a semi-automatic intensity and gradient-based mutual information registration framework that rigidly registers the 3D corresponding tagged MRIs with the 2D ultrasonic images. Based on the two registered modalities, we are able to conduct more detailed quantitative strain comparison of the RF-based UME technique and tagged MRI.

6.3.1 Ultrasound And tMRI Data Acquisition

Both RF ultrasound and 3D tMRI images were acquired in 2D short-axis (SA) views from two healthy subjects with breath-holding and ECG gating. A clinical echocardiography ultrasound scanner (GE Vivid FiVe, GE Vingmed Ultrasound, Horten, Norway) with a phased array probe (FPA 2.5MHz 1C) was used to acquire cardiac ultrasound in-phase and quadrature (I/Q) data at the papillary muscle level at a frame rate of 136 fps. The I/Q data were upsampled to retrieve the RF signals.

Tagged MR images were obtained from a Siemens Trio 3T MR scanner with 2D grid tagging. The 3D tagged MR images consists of a stack of 6 equally spaced SA image sets from near the left ventricle (LV) base to the LV apex. The SA orientation of the ultrasound was approximately consistent with that of the tMRI, but was not guaranteed to be the same. Both modalities utilized full ECG gating during the scans so that they can be registered temporally in a heart beat cycle.

6.3.2 Rigid-body Registration of 2D Elastography with 3D Tagged MRI

For the purpose of inter-modal comparison, we assume that the overall pattern of the heart shape, size and function of the same subject did not change between acquisition by the different imaging modalities. Previous work on inter-modal registration of cardiac ultrasound (US) with MR images has been very limited [101]. It has two main difficulties. First, the cardiac left ventricle (LV) in SA view has a circular shape that lacks reliable anatomical landmarks. Second, the US images have very different appearances compared to MR images. In [102], an approach combining intensity and gradient information was proposed to address the registration of brain US with MR images. In [103] a dynamic cardiac US and MR image registration is achieved by optical tracking of the US probe and fine-tuned by a mutual information registration method.

In our system, since the US probe is not tracked during the imaging process, the semi-automatic registration has to rely on user interactions as well as the image information from the myocardium and the neighboring anatomical structures. The main idea of our registration framework is that we allow the user to freely translate and rotate the US imaging plane w.r.t. the 3D tMRI data and manually find a proper initial registration. Then, a 2D pseudo US image is reconstructed from tMRI, which has an appearance comparable with the 2D US image, so that a mutual information based method can automatically fine-tune the initial manual registration by optimizing the translation (t_x, t_y, t_z) and rotation $(\theta_x, \theta_y, \theta_z)$ of the imaging plane.

Both modalities are ECG gated, which makes them easily temporally aligned. First, the tagged MR images at a mid-systolic phase undergo a Gabor filter bank-based tag removal process [39], which essentially enhances the tag-patterned regions. The tag patterns in the blood are flushed out very quickly after the initial tagging modulation, as shown in Fig. 6.6. This tag removal method enhances the areas of the chest wall, the myocardium and the other surrounding organs, and suppresses the areas of the blood pools and lungs. This de-tagging process increases the image's readability. It is helpful for both the user initialization and the following mutual information-based registration

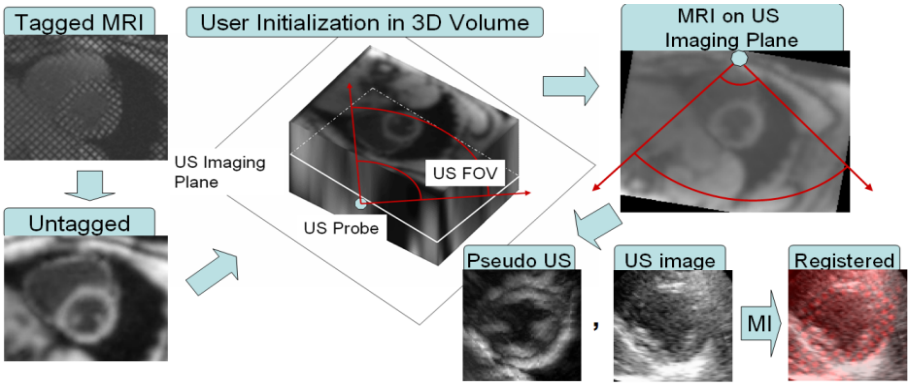

Figure 6.6: The flowchart of the rigid-body registration framework. The stack of the untagged images is interpolated using splines to achieve a 3D isotropic volume. The user can freely tune the translation and rotation parameters of the US imaging plane. After manual initialization, a pseudo US image is constructed from the untagged MRI. The position of the simulated US probe gives the US beam direction. Finally a mutual information-based registration procedure is performed to fine-tune the manual initialization.

algorithm.

Both modalities are interpolated to achieve uniform and isotropic resolution. Then the rigid registration problem becomes one of looking for the position and orientation of the 2D UME imaging plane with respect to the 3D tMRI volume.

The characteristic appearance of cardiac US images comes from two main sources. First, the speckle intensity levels vary in different tissues. For instance, we observe that the blood pool area is darker than the myocardium. Second, because of the impedance mismatch effect, US images usually enhance the interfaces between successive tissue layers [102]. We further observe that the angles between the interfaces with the incoming US beam affect the enhancement magnitude. Here we denote vector $\mathbf{b}$ as the direction of the incoming US beam. Therefore we model the transformation T from the tag removed tMRI, I_u, to the reconstructed image by:

$$T(I_u(x,y)) = \alpha I_u(x,y) + \beta \nabla I_u(x,y) \cdot \mathbf{b}(x,y) + \gamma I_v(x,y) \tag{6.4}$$

The right hand side of the equation is a linear combination of three terms, where the relative weighting parameters α, β and γ are experimentally determined. The first

term is the tag-removed image. The second term is an edge detector, which is sensitive to orientation . In order to detect the dark strips between the myocardium and the neighboring liver, the third term I_v acts as a valley detector. Suppose $\mathbf{H}(x, y)$ is the Hessian matrix at $I_u(x, y)$, and λ_1 and λ_2 are the eigenvalues of $\mathbf{H}$. If $\lambda_1 < -|\lambda_2|$, then at pixel (x, y) an intensity valley exists, whose width is proportional to $|\lambda_1|$, and its orientation is determined by the eigenvector $\mathbf{v}_1$. Hence we model the valley detector as:

$$I_v(x, y) = \begin{cases} \lambda_1^2 \mathbf{v}_1(x, y) \cdot \mathbf{b}(x, y), \; if \;\; \lambda_1 < -|\lambda_2| \\ 0, \qquad\qquad\qquad otherwise \end{cases} \tag{6.5}$$

The mutual information-based optimization of the translation and rotation parameters is found by using gradient decent. Since the tag-removed image I_u is heavily blurred, the algorithm tends to get stuck in local maxima. Thus a proper manual initialization is necessary. Multiple initializations are also helpful to find the global maximum.

6.3.3 Strain Estimation

Ultrasound Myocardial Elastography

In the UME technique, the two in-plane orthogonal displacement components (lateral and axial) were estimated using one-dimensional (1D) cross-correlation and recorrelation of RF signals in a 2D search [96]. The cross-correlation technique employed a 1D matching kernel of 7.7 mm and 80% overlap. The reference and comparison frames respectively contained the RF signals before and after deformation. An $8:1$ linear interpolation scheme between two adjacent original RF signal segments of the comparison frame within the 1D kernel was employed to improve the lateral resolution [96]. The maximal cross-correlated value yielded from the RF signal segment in the comparison frame was considered the best match with the RF signal segment in the reference frame. Cosine interpolation was then applied around this maximum of the cross-correlation function for a more refined peak search.

The correction (or, recorrelation) in axial displacement estimation [96], was performed to reduce the decorrelation resulting from axial motion. In UME, recorrelation was implemented by shifting RF signal segments according to the estimated axial displacement in the comparison frame, prior to the second lateral displacement estimation.

Tagged MRI

The registered imaging plane may not be the same as one of the tMRI SA slices. Simply interpolating in between the slices might blur the tagging grids and result in inaccurate strain calculations. We observe that the 2D tagging grids are actually the intersections of two sets of orthogonal tagging sheets and the tMRI imaging planes. If we recover the geometry of the tagging sheets, then by finding their intersections with the registered US imaging plane, we are able to calculate the strain values in the registered imaging plane. Therefore we chose to track the tagging sheets over time as in Chapter 3 [104].

First we decompose the grid tagged images into two sets of horizontal and vertical line tagged images by suppressing the component of one direction of the tagging grids via band-stop filtering in the images' Fourier domain. Then the two sets of 3D tagged MR images are filtered with a tunable 3D Gabor filter bank so that the tagging sheets can be enhanced, where the parameters of the 3D Gabor are adaptive to the spacing and orientation of the local tagging sheets. In the tracking step, we impose a set of deformable meshes onto the initial tagging sheets and let them deform according to the enhanced tagging sheets over time. The tracking process is controlled by a dynamic model, and the deformable mesh is smoothed with an internal spring force as well as an inter-mesh spring force.

During tracking, the displacements $\mathbf{u}$ of the intersection points of the two sets of perpendicular tagging sheets and the registered imaging plane are recorded. Then for all the other pixels in the myocardial area, their displacements $\mathbf{u}$ are interpolated by a spline interpolation method.

The strain calculations is the same as that employed in the previous UME section. Horizontal, vertical, radial and circumferential strains are calculated.

6.3.4 Experimental Results

In our experiments, active contraction (i.e., systole) was only considered for the assessment of the contractility of cardiac muscle. The strain estimates of these two imaging modalities have qualitatively good agreement. A visual comparison of the strain patterns can be found in Fig. 6.7 and Fig. 6.8. For a normal subject (shown in Fig. 6.7), the horizontal and vertical strains of this clinical data show similar patterns to those of the theoretical framework proposed by Lee et al. [96].

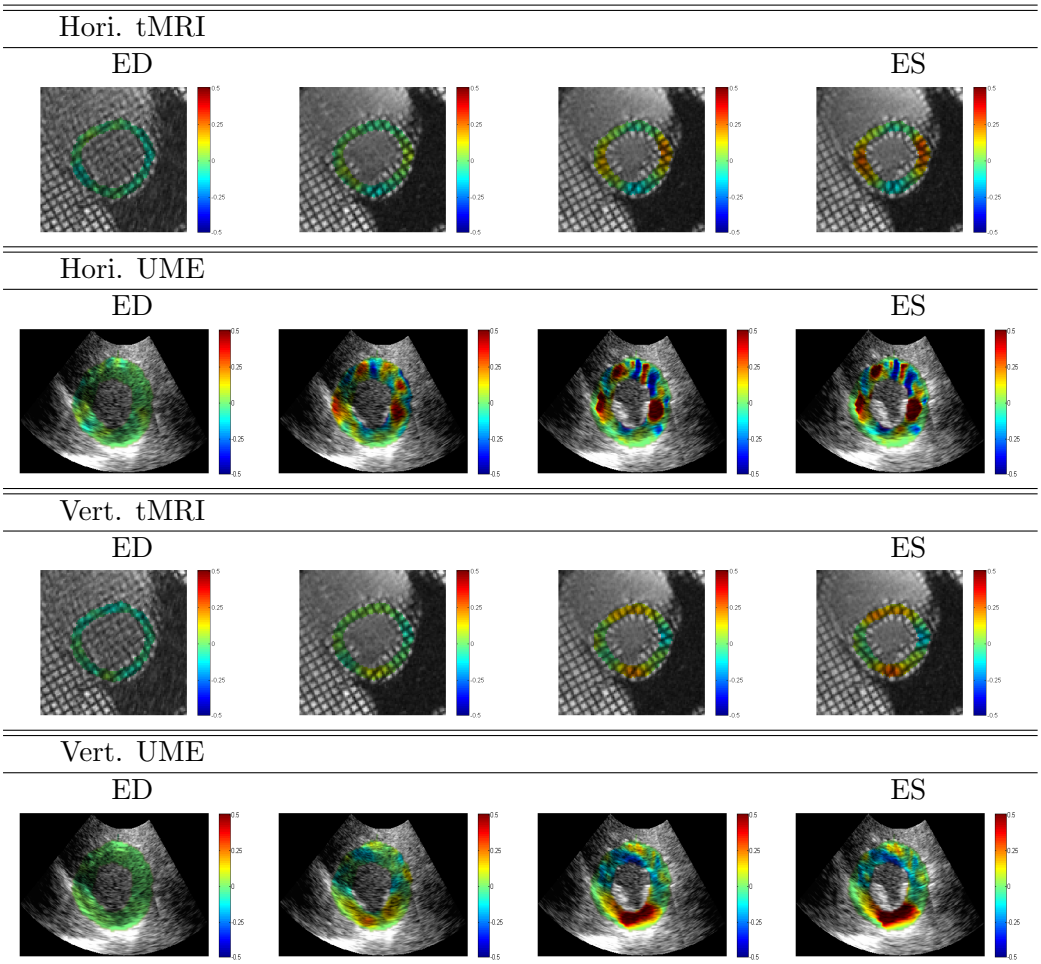

Figure 6.7: Strain pattern comparison between tMRI and UME on a healthy subject. Horizontal and vertical strains of the left ventricle are displayed. For each strain component, four time frames are shown from the end-of-diastole (ED) phase to the end-of-systole (ES) phase. The pseudo color is displayed on a scale of the strain value from -0.5 to 0.5.

Furthermore, polar strains (shown in Fig. 6.8) show radial thickening and circumferential shortening except for the anterior and septal walls in the ultrasound images due to the low signal-to-noise (SNR) ratio, which results from shadowing by the rib and the lung.

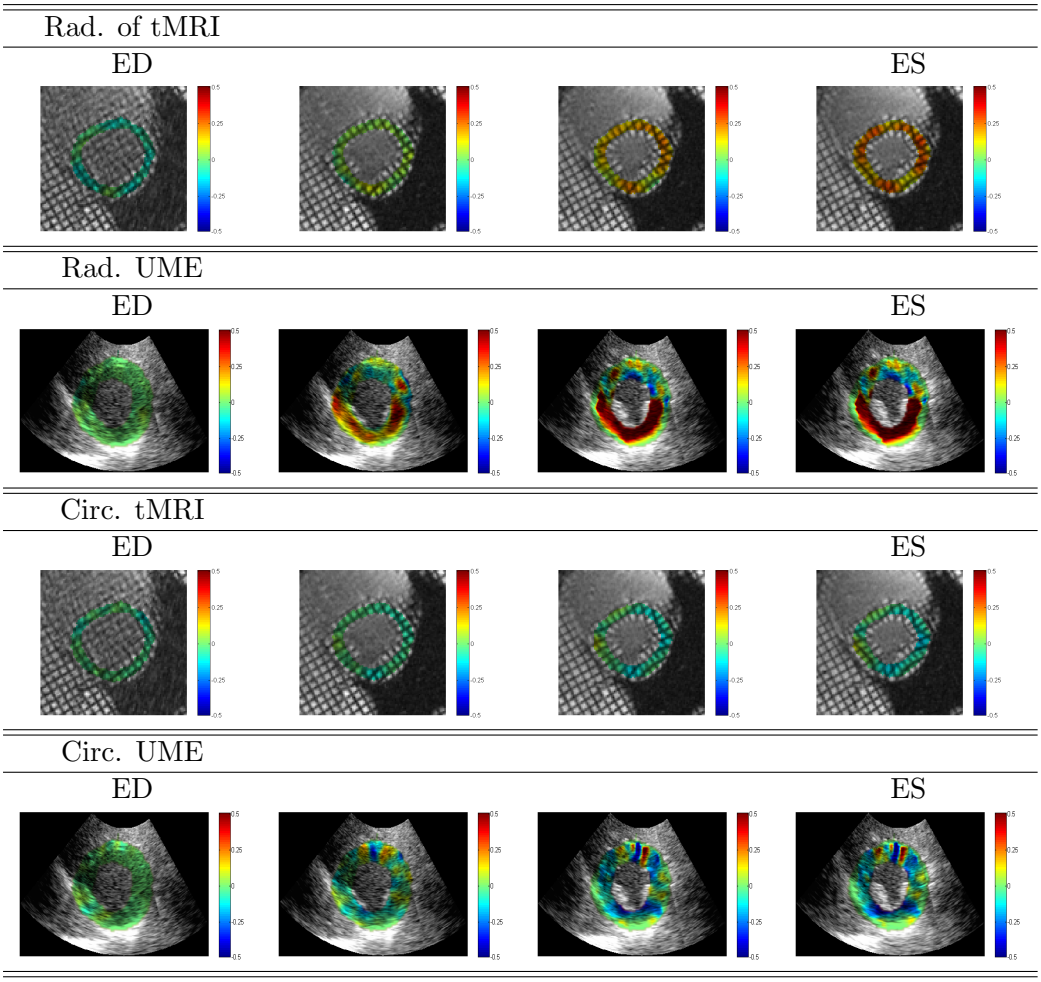

Figure 6.8: Strain pattern comparison between tMRI and UME on a healthy subject. Radial and circumferential strains of the left ventricle are displayed. For each strain component, four time frames are shown from the end-of-diastole (ED) phase to the end-of-systole (ES) phase. The pseudo color is displayed on a scale of the strain value from -0.5 to 0.5.

As shown in Fig. 6.3.4, for more spatially localized quantitative analysis, we divide the LV into 6 sectors: the septum 1, the septum 2, the posterior wall, the lateral wall 1, the lateral wall 2, and the anterior wall.

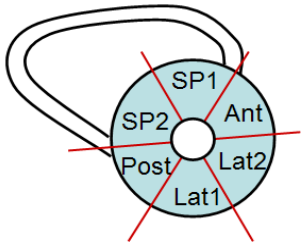

Figure 6.9: Illustrates the division of the 6 sectors.

According to the quantitative results shown in Fig. 6.3.4, both modalities show that the total radial and circumferential strains, from ED to ES, in six different myocardial regions show similar trends of strain value accumulation. In tMRI results, we observe that for intra-subject case, the mean strain values in each sector have similar shapes and slopes, which means the myocardial strain grows evenly and stably over time. Even for the inter-subject case, the strain patterns of the two subjects look similar, which shows that tMRI strain estimation is quite robust. In addition, the relatively small and stable standard deviations of tMRI strains also show the robustness of tMRI. In UME results, for the case of subject 1, the mean strain values of sectors posterior, lateral 1 and lateral 2, which are opposite to the US probe, are higher than those of the tMRI, while the other 3 sectors, which are near the chest wall and closer to the US probe, have smaller strains. This suggests that UME may be affected by the US beam direction. On the other hand, in general, ultrasound elastographic strain estimates exhibit higher spatial resolution but larger noise. Even though the original pixel resolution in both tagged MR and ultrasonic images is adjusted to the same scale, the overestimation from ultrasound elastography for subject 1 may also come from its high resolution of estimation.

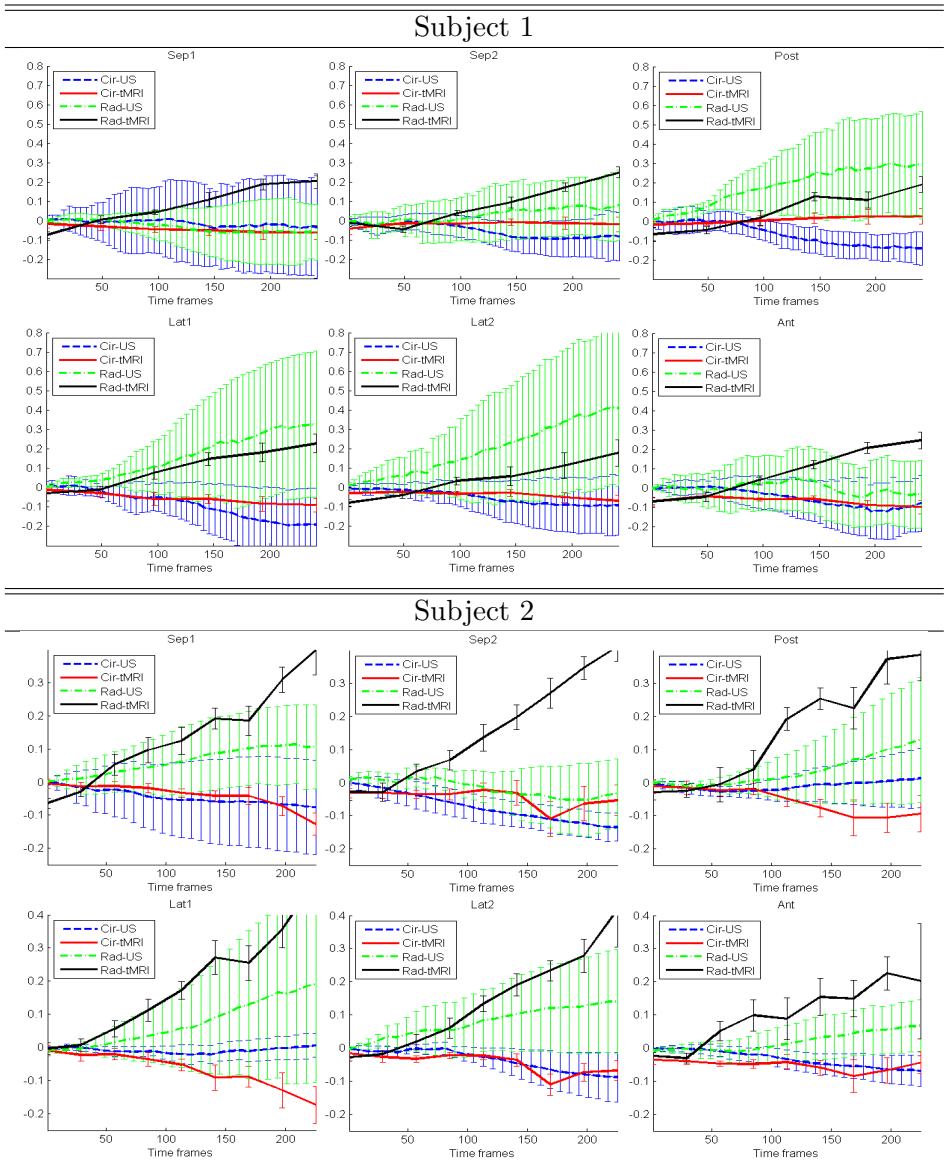

Figure 6.10: In each sector of the LV, the mean and standard deviation of the radial and circumferential strain values are calculated from end-diastole to end-systole. We find that the UME results have an overall trend which is similar with that of the tMRI. However the standard deviation of the US results tends to keep growing quickly, while that of the tMRI remains stable.

As shown in Fig. 6.11, the mean strain discrepancies between UME and tMRI increase over from ED to ES. In addition, the ultrasound elastographic estimation errors accumulate during systole, as can also be depicted from the increasing standard deviations. The circumferential strain estimates show the strongest agreement between the two modalities.

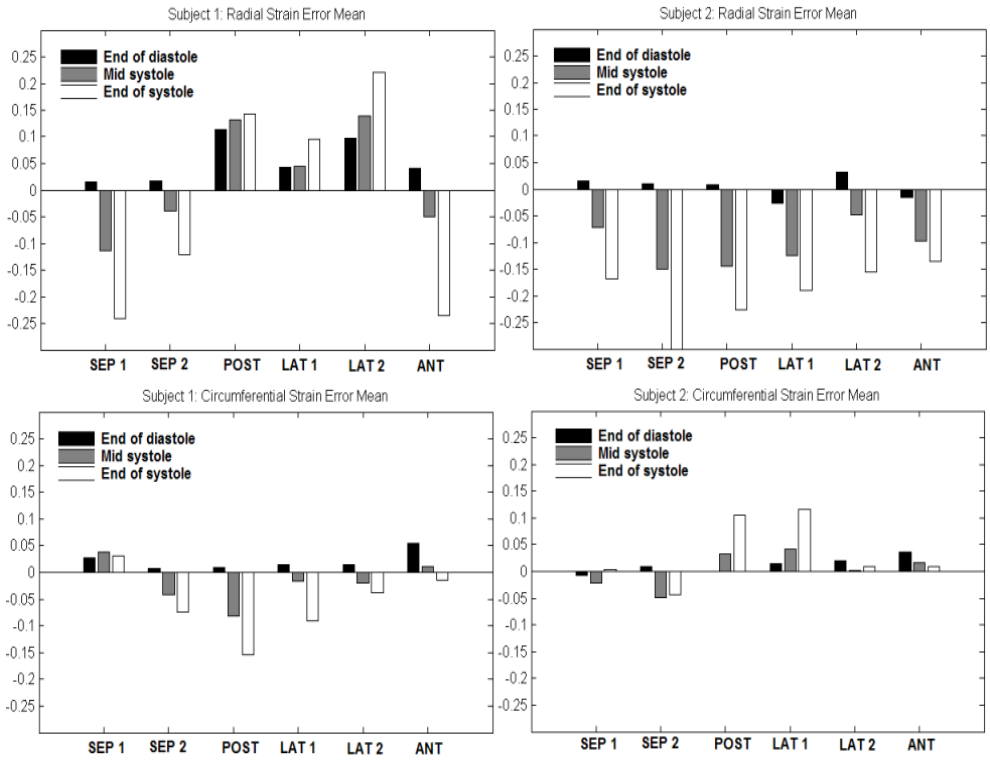

Figure 6.11: The strain error mean of the UME technique compared with tMRI. We find in UME modality, from ED to ES, the errors are also accumulative.

6.3.5 Discussion

Ultrasound Myocardial Elastography is qualitatively able to assess myocardial motion and deformation with values well comparable to those obtained with tagged MRI in normal subjects. However, for quantitative strain measurement, tMRI will provide much more accurate and robust estimates. Future work will focus on the assessment of the role of the sonographic SNR on the myocardial elastographic strain estimates and study of the tradeoff between spatial resolution and strain accuracy for precise

quantification in both normal and acute infarction patients. We will also carry out more UME and tMRI comparisons.

6.4 Non-tracking Based Strain Estimation

A main difficulty of tag-tracking based methods is in balancing the internal and external forces of the deformable model that is used in the automated tracking process. If the internal forces are too small, then irregular tracking results, such as tag jumps, will be present. If the internal forces are too big, then over-smoothed tags will lead to underestimated strain results. Another popular approach is using the HARP technique [36]. In [105, 106], myocardial velocity field and pathlines are calculated from the phase map using the HARP technique. Then strain is obtained from the HARP phase *tracking* results. A limitation of HARP-based methods is that they have difficulties in handling tags with large deformation. In addition, phase *tracking* is done by adding up the phase changes in each previous temporal frame. Therefore the tracking error is prone to accumulation.

As described in the previous chapters, comparing with Fourier-transform-based methods, such as HARP, Gabor filter is a spatially localized method, so that it is more adaptive to large tag deformation. In this section, we propose a non-tracking 2D strain estimation method based on Gabor filters. At each pixel in the myocardium area, we extract the local tag distances and orientations in both $x-$ and $y-$ coordinates by searching for an optimal Gabor filter. Then the 2D strain and local rotation angle at each pixel can be obtained by using the strain formula in terms of deformation gradient. In this way, we don't need to track the tags or phase angles over time, and the limitations of tracking methods listed in the previous paragraph can be avoided. We first test our method on a series of phantom images and study the effectiveness of our Gabor-based strain estimation method. Then we apply this method on normal and patient data. From the experiments, we find that our strain estimation method is accurate and robust to noise. It has the potential to quantitatively diagnose cardiac malfunctions or diseases.

6.4.1 Gabor Filter Design

In this application, we use a symmetric Gaussian envelope with $\sigma_x = \sigma_y = 1/\sqrt{U^2 + V^2}$, so that the rotation of the Gabor filter is determined only by the 2D frequencies of the complex sinusoid, which can be derived by $\phi = \arctan(V/U)$. The spacing between peaks of the sinusoid is determined by $S = 1/\sqrt{U^2 + V^2}$. A Gabor filter in our application can be defined with only two parameters U and V:

$$h(x, y) == \frac{U^2 + V^2}{2\pi} e^{-[\frac{(x^2+y^2)(U^2+V^2)}{2} + j2\pi(Ux+Vy)]} \tag{6.6}$$

Same as described in Chapter 5, the myocardial tracking section, at time 0 of the tagged MR imaging process, when the tagging lines or grids are initially straight and equally spaced with distance D, we set the initial parameters U_i and V_i of the Gabor filter to be equal to the frequencies of the image's first harmonic peaks in the spectral domain [58]. During a heart beat cycle, the tagging lines or grids deform with the underlying myocardium, and the spacing changes $m = S/D$ and orientation changes $\Delta\phi = \phi - \phi_i$ occur accordingly. We optimize U and V of the Gabor filter to fit the deformed local tag patterns, which means by convolving the optimal Gabor filter $h_o(U_o, V_o)$ with the local image patch I that centers at a certain pixel (x, y), we get the highest magnitude response. Then, we can extract the local deformations m and $\Delta\phi$.

$$(U_o, V_o) = \underset{U,V}{\operatorname{argmax}}(|h(U, V) * I|) \tag{6.7}$$

The optimization procedure can be performed using different strategies, such as gradient descent or simplex method. Since we only need to optimize two parameters U and V, in our experiment, the optimization converges very fast by using either method.

6.4.2 Strain Estimation

Instead of calculating the strain values in terms of the gradient of the displacement by tracking the tag pattern, we directly analyze the local tag deformation. For simplicity, we assume that the myocardium is incompressible, and it undergoes three possible deformations: stretching, compression, and local rotation. The initial tag spacings and

orientations are referred to as the initial state, so that Lagrangian strains in beating myocardium can be obtained by comparing the deformed tags to the initial state.

For a myocardial element, we assume that in a certain coordinate system $\mathbf{X}$ its initial length is $d\mathbf{X}$. After deformation, the myocardial element's length is $d\mathbf{x}$ in coordinate $\mathbf{X}$. At position $\mathbf{x}$ we can define the deformation gradient as in [94]:

$$\mathbf{F} = \frac{d\mathbf{x}}{d\mathbf{X}} = \nabla \mathbf{x} \tag{6.8}$$

For 2D deformation gradient, we have:

$$\mathbf{F} = \begin{bmatrix} \frac{d\mathbf{x}}{d\mathbf{X}} & \frac{d\mathbf{x}}{d\mathbf{Y}} \\ \frac{d\mathbf{y}}{d\mathbf{X}} & \frac{d\mathbf{y}}{d\mathbf{Y}} \end{bmatrix} \tag{6.9}$$

As seen in Figure 6.12, the initial tag pattern has two sets of horizontal and vertical tagging lines with spacings equal to D_x and D_y. After myocardial deformation, the deformed tagging line spacings become S_x and S_y, and the orientation changes of the tagging lines are $\Delta\phi_x$ and $\Delta\phi_y$. Then from Equation 6.9, the deformation gradient tensor $\mathbf{F}$ can be derived by:

$$\mathbf{F} = \begin{bmatrix} \frac{S_x \cos\Delta\phi_y}{D_x \sin\phi} & \frac{S_y \sin\Delta\phi_x}{D_x \sin\phi} \\ \frac{S_x \sin\Delta\phi_y}{D_y \sin\phi} & \frac{S_y \cos\Delta\phi_x}{D_y \sin\phi} \end{bmatrix} \tag{6.10}$$

where $\phi = \frac{\pi}{2} - \Delta\phi_x - \Delta\phi_y$. From the previous subsection, the spacing parameter m and orientation changes $\Delta\phi$ of the Gabor filter can be directly used to derive $\mathbf{F}$.

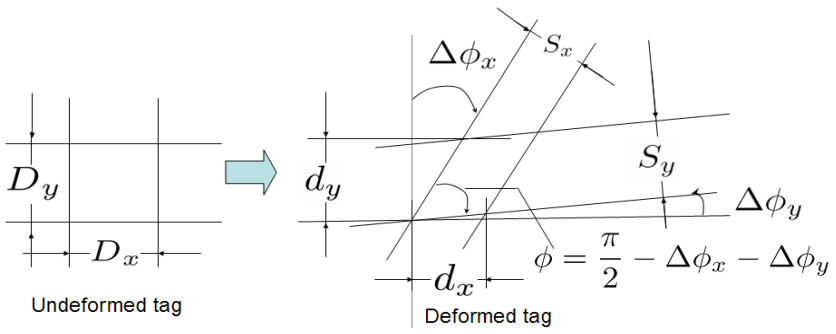

Figure 6.12: The illustration of $\mathbf{F}$ calculation. After tag deformation, $d_x = S_x \cos\Delta\phi_y / \sin\phi$, and $d_y = S_y \cos\Delta\phi_x / \sin\phi$, which are used in Equation. 6.10.

From $\mathbf{F}$, we can derive the Lagrangian finite strain tensor $\mathbf{E}$ and local rotation matrix $\mathbf{R}$ by:

$$\mathbf{E} = \frac{1}{2}(\mathbf{F}^T \cdot \mathbf{F} - \mathbf{I}) \tag{6.11}$$

$$\mathbf{R} = \mathbf{F}(\mathbf{F}^T \cdot \mathbf{F})^{-1/2} \tag{6.12}$$

where $\mathbf{I}$ is an identity matrix.

6.4.3 Evaluation on Phantom Images

To evaluate our strain estimation method, we generate 5 frames of phantom images that simulate the contraction process of the left ventricular (LV) muscle. A main advantage of using phantom images is that our strain estimates can be easily compared with the ground truth. As seen in the first and second rows of Fig. 6.15, we generate a 2D LV phantom with both horizontal and vertical tagging lines in short axis, by adding 2D sinusoid patterns. Then the LV model undergoes incompressible deformation of contraction and rotation. At time t_4, based on the calculation of the 2D area, the ejection fraction (EF) of this phantom is 75%, which is higher than human values in most cases, so that we guarantee this model can fit most clinical circumstances (In healthy heart, based on calculation of 3D volume, EF is about $55\% - 70\%$ [107]. In diseased heart, this value tends to be smaller.)

In clinical tMRI imaging settings, the initial horizontal and vertical tag spacings are equal: $D_x = D_y = D$. Using Equation 6.7, the local deformations S_x/D, S_y/D, $\Delta\phi_x$ and $\Delta\phi_y$ can be obtained by optimizing the Gabor filter's frequency parameters U and V. In the third row of Fig. 6.15, the Gabor-estimated local deformation maps at time t_4 are illustrated. For maps of S/D, the grey background equals 1, and brighter intensity corresponds to bigger tag spacing. For maps of $\Delta\phi$, the grey background equals 0, and brighter intensity stands for positive orientation change. We can find that our Gabor filter optimization method achieves very smooth deformation maps that are consistent with the deformed tag patterns. Then the deformation gradient tensor $\mathbf{F}$, the strain

tensor $\mathbf{E}$ and the local rotation matrix $\mathbf{R}$ can be derived from Equations 6.10, 6.11 and 6.12.

Rather than the 2D horizontal-vertical Lagrangian strain tensor in Equation 6.11, in myocardial deformation research, we are more interested in the radial and circumferential strains. Positive and negative radial strains indicate myocardial thickening and thinning, respectively, while myocardial stretching and shortening are represented by positive and negative circumferential strains, respectively. As in the previous section, we define an angle θ about the centroid of the LV, and transform $\mathbf{E}$ into a radial-circumferential strain tensor $\dot{\mathbf{E}}$ with a rotation matrix $\mathbf{Q}(\theta)$, so that:

$$\dot{\mathbf{E}} = \mathbf{Q}\mathbf{E}\mathbf{Q}^T. \tag{6.13}$$

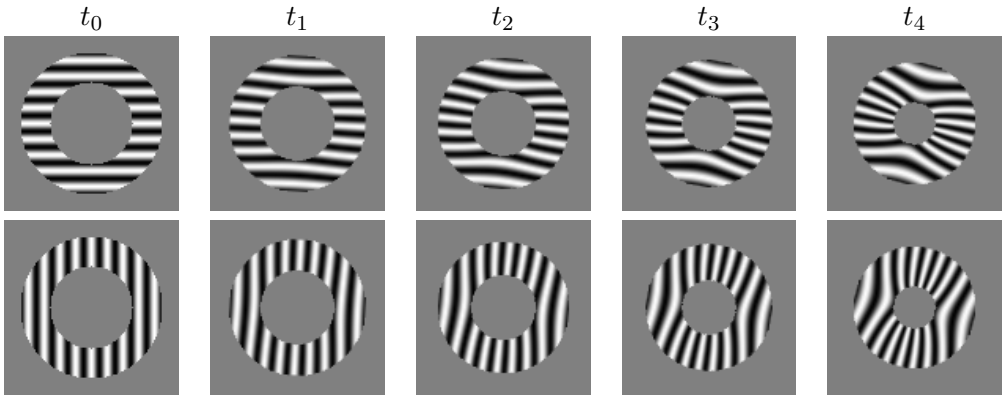

Figure 6.13: These two rows are the simulated phantom images with horizontal and vertical tagging lines, which undergo an inward contraction with a rotation from t_0 to t_4.

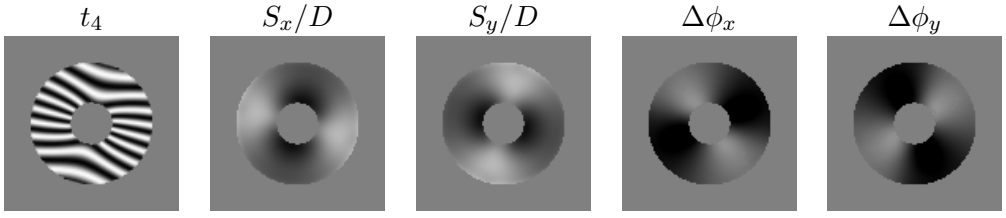

Figure 6.14: The deformations are extracted from the phantom images at t_4 using our Gabor filter method.

For quantitative evaluation, we calculate the means and standard deviations of the 2D strain and rotation angle. As seen in Fig. 6.16, we find that our method is

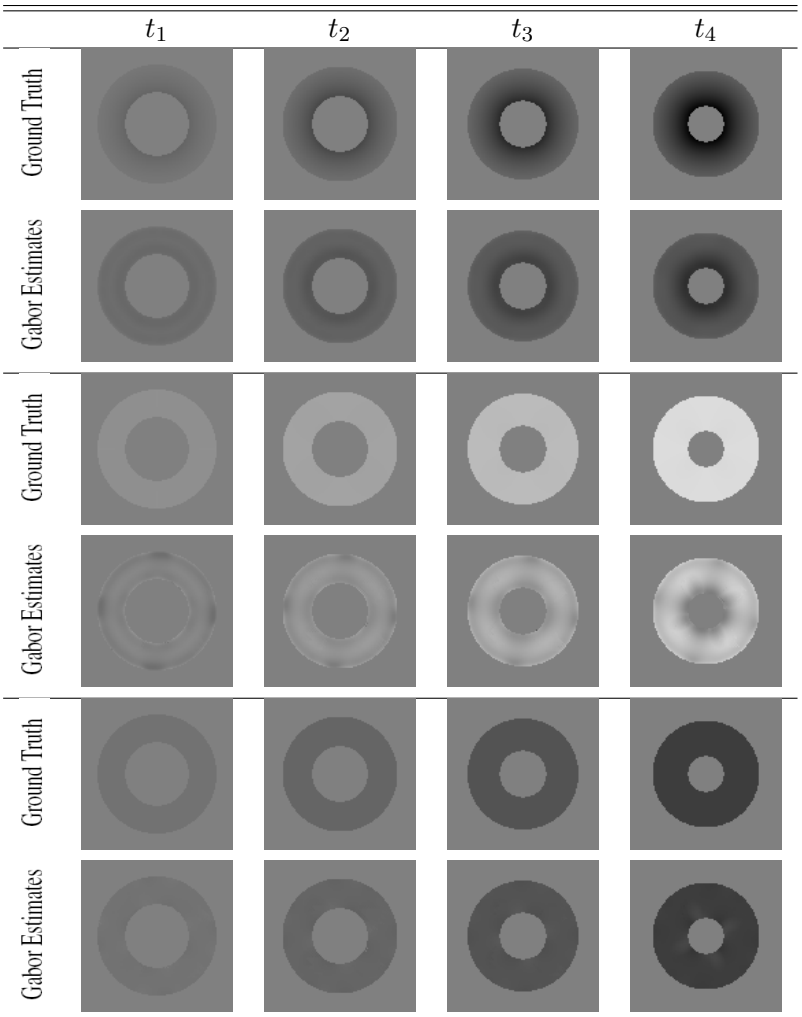

Figure 6.15: The comparison of the ground truth and our estimation. Circumferential strain, radial strain and rotation angle at t_1 to t_4 are compared.

most accurate in estimating rotation angle. For circumferential strain, our estimation matches with the ground truth well from t_1 to t_3, and tends to underestimate when contraction gets bigger at t_4 (EF = 75%, which is rare in real human data). For radial strain, our method underestimates for every time frame, but still has the same trend as the ground truth.

Our non-tracking method calculates the local deformation at each single pixel. Therefore, in real data implementation, a major difficulty comes from the noisy nature of tMRI, which usually leads to irregular deformation maps. To solve this problem, we add a filtering loop to smooth out the noise. As illustrated in Fig. 6.19, in each iteration of the filtering loop, at each pixel, the local image patch is convolved with

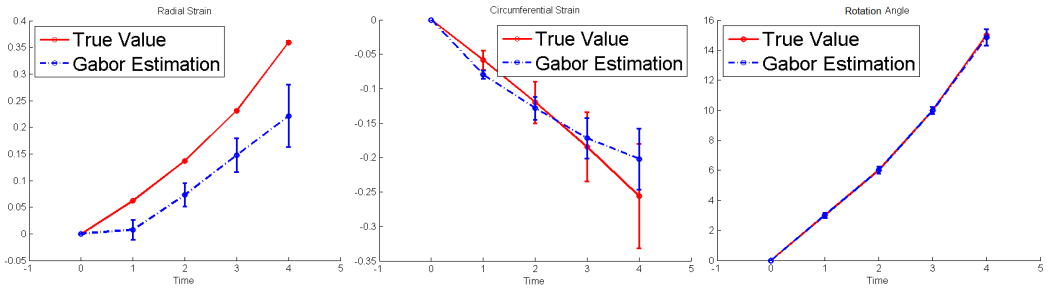

Figure 6.16: Quantitative comparisons of the mean and standard deviation, at each time frame, of the radial strain (left-hand-side), the circumferential strain (middle) and the rotation angle (right-hand-side) show our estimations are consistent with the ground truth.

the estimated optimal Gabor filter, and the convolution result is used to update the pixel's intensity, which is used in the next iteration. As seen in Fig. 6.17, the LV region LV_0 in the input image is noisy, thus without smoothing, the deformation maps S_{x_0}/D and $\Delta\phi_{x_0}$ are corrupted with error estimations. After 3 iterations of filtering the LV with the estimated Gabor filter at each pixel, the smoothed LV_3 gives more regular deformation maps S_{x_3}/D and $\Delta\phi_{x_3}$.

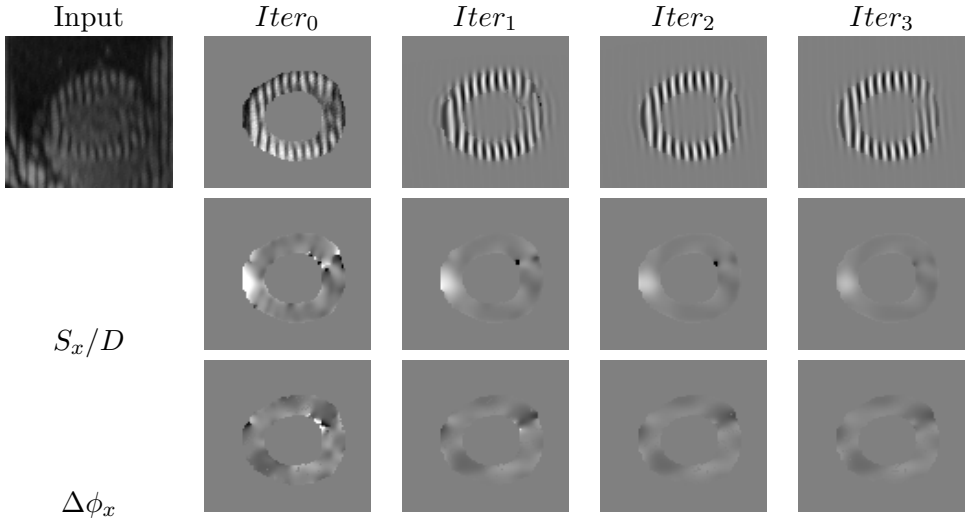

Figure 6.17: A representative of real world tagged MR images whose left ventricle in the input image is noisy, which leads to irregular estimations of S_{x_0}/D and $\Delta\phi_{x_0}$. After 3 smoothing iterations, we get a smoother LV area and better estimations of S_{x_3}/D and $\Delta\phi_{x_3}$.

However, smoothing the input image could be a dangerous strategy because it also smoothes the myocardial deformations. Therefore we need to examine how smoothing

loops affect the strain estimation. In the phantom images, at time t_4, we apply filtering loops and observe how strain and rotation angle change. In Fig. 6.19, we see the estimations of rotation angle and circumferential strain do not change much after 4 smoothing loops. But radial strain estimation decreases after the first loop, and tends to be stable after a few iterations.

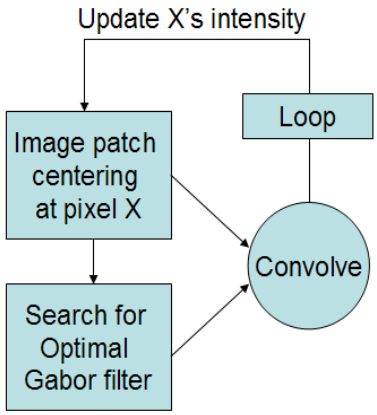

Figure 6.18: The flowchart of the smoothing method.

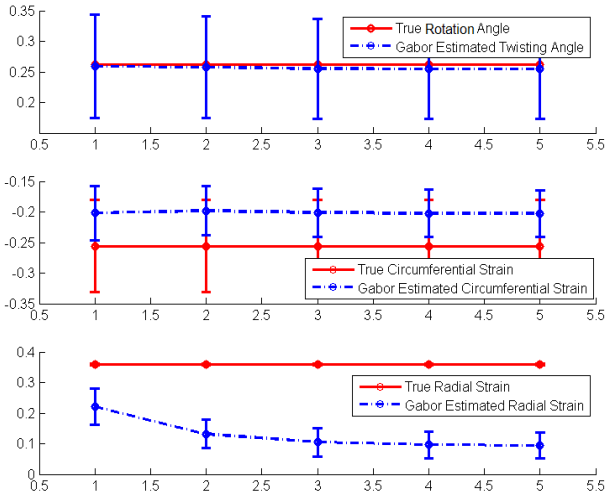

Figure 6.19: Quantitative analysis of the rotation angle (first row), the circumferential strain (second row) and the radial strain estimations (third row) w.r.t. the iteration number of the smoothing loop.

6.4.4 Experiments On Real Data

We tested our novel strain estimation method on both normal and patient data. For grid tagged MRI, we first separate the tag grids into 2 sets of tagging lines by a band-stop filter [108]. We estimate the strain and rotation angle only within the LV contours. To smooth out noise, we apply 3 iterations of the smoothing filter. In Fig. 6.20, we show a visual comparison of our estimates in a normal subject and a patient. For quantitative analysis, we divide the LV into 6 sectors, and calculate the means of strain and rotation angle in each sector at each time frame. In Fig. 6.21 we show the quantitative comparison. It is interesting to see that the magnitudes of the strain or rotation angle value are not the only criteria to diagnose abnormality. Their spatial and temporal distributions seem more important. Normal heart seems to have more smoothly distributed strain and rotation angle values. On the other hand, the patient heart seems to contract more vigorously at the 12 and 7 o'clock positions (indicated by the high strain magnitudes). However, most of the contraction is turned into a rotating motion (indicated by the big rotation angles), which makes the contractive efficiency poor. This suggests that the myocardial function should be assessed on comprehensive bases, including the strain magnitude, the regional strain pattern, and the regional tissue rotation pattern. Our novel strain estimation method works well in capturing the regional myocardial strain and rotation in tMRI.

6.4.5 Discussion

In this section, we developed a novel non-tracking-based strain estimation method in tagged MRI. This method calculates strain by extracting the tag's deformation gradient, and avoids the limitations of conventional tracking-based strain estimators. We tested this method on both simulated and real world images. In simulated images, we quantitatively evaluated the accuracy and robustness of our non-tracking estimator. We also tested our method on both normal and patient data. We find that our estimation results are highly consistent with simulated ground truth, and are potentially valuable to distinguishing normal and abnormal data. In future work, we will develop

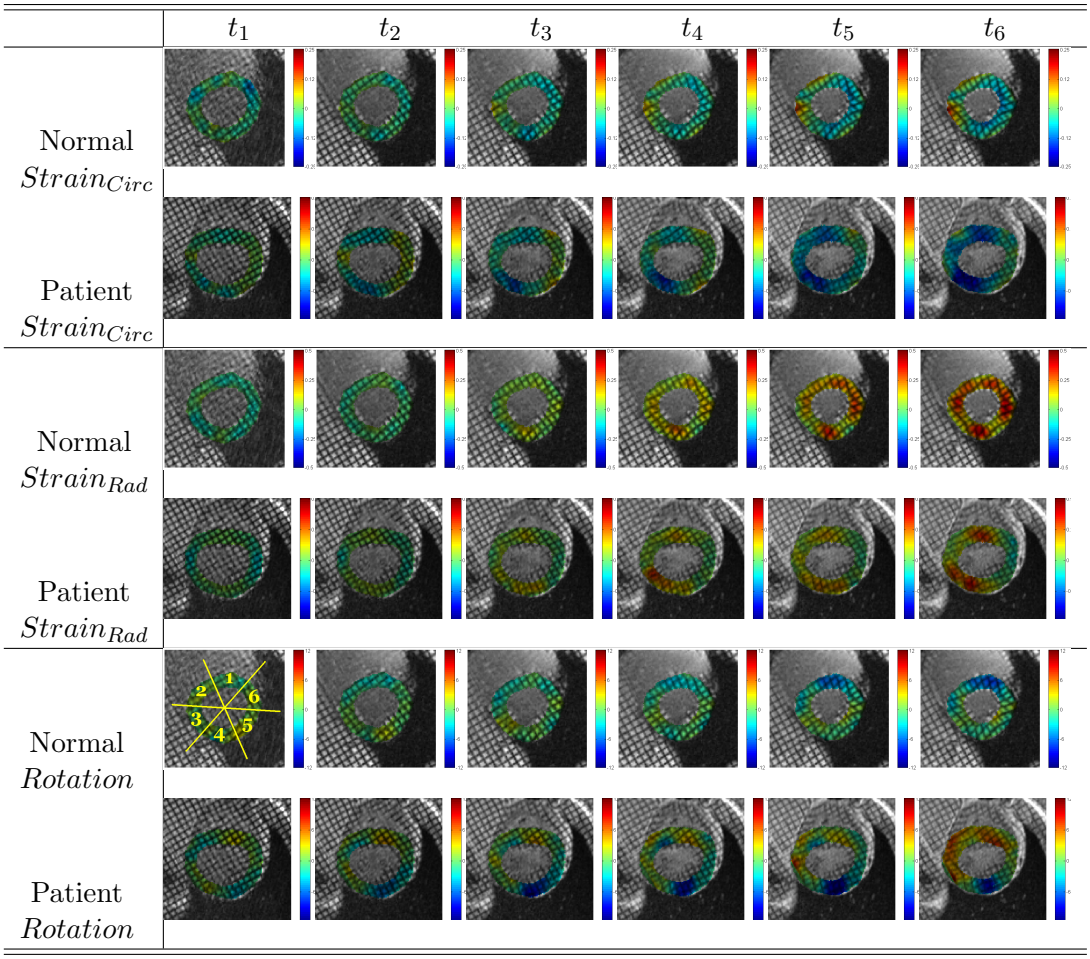

Figure 6.20: Visual comparison of normal (left-hand-side) and patient's (right-hand-side) circumferential strain (first row), radial strain (second row) and rotation angle (third row) estimations at time t_1, t_4 and t_6. For quantitative analysis, we divide the LV into 6 sectors, which is illustrated in the lower-left image.

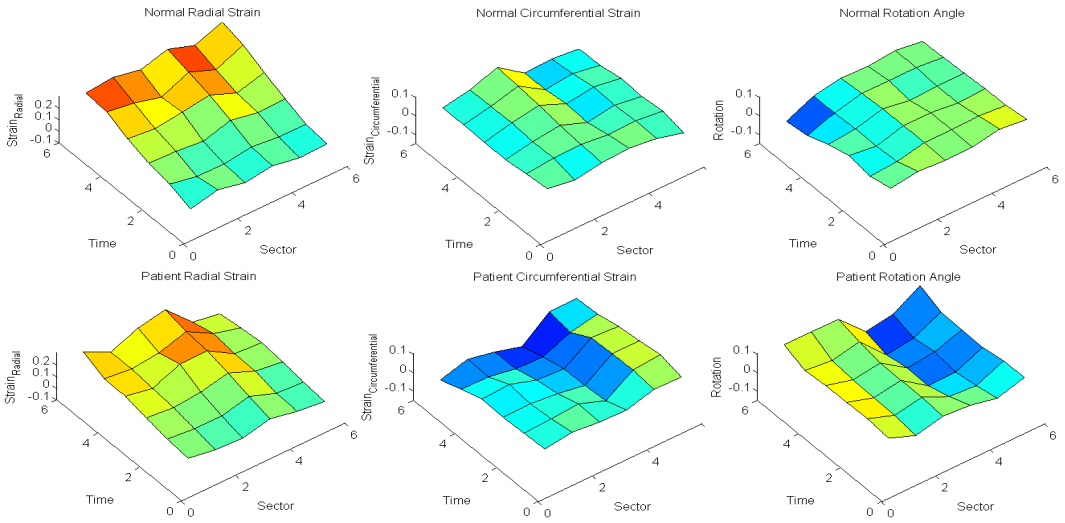

Figure 6.21: In each LV sector, at each time frame, we calculate the mean value of the radial strain (left), the circumferential strain (middle) and the rotation angle (right). Thus, the colored surfaces illustrate the temporal and spatial distributions of the estimated values. The first row is from normal data. The second row is from patient data.

the analysis of the strain and rotation patterns, in order to extract useful information to help with cardiac malfunction and disease diagnosis.

6.5 Identifying Regional Cardiac Abnormalities Using Tensor Analysis

Some previous strain estimation methods [49, 47, 43] have been implemented to compare normal and pathological data. Their results show noticeable differences in the strain pattern of normal and abnormal hearts, which reveals the potential of using strain to identify pathology in cardiac function. However, limited research has been conducted to fulfill this potential in a quantitative manner. In [109], the percentage change in end-systolic circumferential strain was used to detect acute ischemia in an animal heart with experimentally induced coronary artery occlusion. However, this was not a study of naturally developed pathology, and no inter-subject variation has been evaluated.

In this section, we will try to use the spatio-temporally distributed myocardial strain pattern to identify and localize abnormal cardiac function in human subjects. In [110], an exploratory normal contraction reference model has been set up based

on the principal component analysis (PCA) of tMRI scans from 8 healthy subjects using their spatio-temporal deformation. Abnormalities could be found by comparing with the reference model in the PCA subspace. However, the main difficulty behind this is the large strain variance among normal subjects, and the even larger variance in patients, which make it difficult to define a normal or abnormal criterion. On the other hand, the spatio-temporally distributed myocardial strain is far more complicated to quantitatively interpret than the 1D ECG signal or the scalar ejection fraction. Pathology develops with complicated and systematic consequences. For example, as shown in the patient images in Fig. 6.23, a region of ischemia might cause the rest of the heart to contract more vigorously to compensate. In this case, the spatial or temporal pattern of the strain could be of more importance than strain value alone in detecting cardiac malfunctions.

To solve these two difficulties, we formulate the detection of abnormality into a novel spatio-temporal tensor-based linear discriminant analysis (LDA) classification framework. In order to learn the classifier in a supervised fashion, we gathered a group of normal and patient tMRI sequences in short axis (SA), and applied the non-tracking-based strain estimation method in the previous section to extract the radial strain, circumferential strain and tissue rotation angles to construct the training data. Then a tensor-based LDA classifier is employed based on the Fisher criterion to find an optimal linear projection that maximizes the between-class, i.e., the normal and patient, scatter and minimizes the within-class scatter. Rather than the conventional vector-based LDA that projects the feature space onto a scalar, the advantage of using our spatio-temporal tensor based LDA is that its dimension reduction is separately operated in the spatial and temporal domains, so that it conserves better the spatio-temporal structure and the information of the training data. On the other hand, the advantage of using a linear classifier rather than nonlinear approaches such as SVM, is that using the pseudo-inverse matrix of the linear projection function, we are able to back-project the abnormality found in the subspace to the original feature space, so as to localize the regional cardiac abnormality in a more physically meaningful way. We have tested our novel classification algorithm on a clinical dataset of forty one tMRI

sequences from normal and patient subjects, and have achieved a higher or comparable detection accuracy rate compared to conventional classification algorithms, such as PCA, LDA and SVM. The recovered regional abnormalities from our algorithm agree with the patient's pathology and doctor's diagnosis well and provide a promising avenue to regional cardiac function analysis.

6.5.1 Quantitative data preparation

For quantitative regional cardiac function analysis, we divide the left ventricle at a given base-apex level into two layers (endo- and epi-cardium) and ten sectors (septum is equally divided into 3 sectors and the rest of the heart is divided into 7). This results in 20 ordered regions in total, as can been seen in Fig. 6.22.

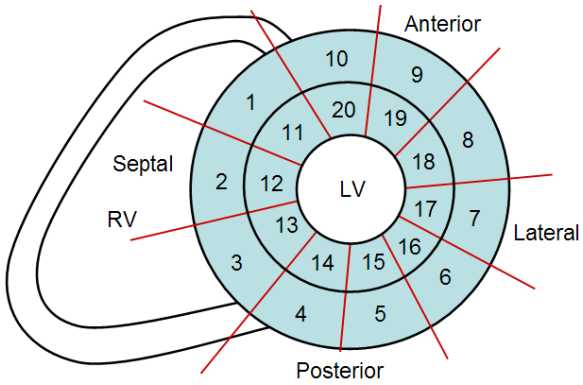

Figure 6.22: The left ventricle is divided into 20 regions.

Within each region, we use the median value of the radial strain, the circumferential strain and the rotation angle that are calculated using the non-tracking based strain estimation method to represent this region's deformation, so as to remove outliers and make the data preparation more robust. We denote them as $\mathbf{E}_R^i$, $\mathbf{E}_C^i$ and θ^i $(1 \leq i \leq 20)$, respectively. Therefore, the myocardial deformation in a single time frame can be represented by a 60×1-sized vector:

$$\mathbf{V} = (\mathbf{E}_R^1, ..., \mathbf{E}_R^{20}, \mathbf{E}_C^1, ...\mathbf{E}_C^{20}, \theta^1, ..., \theta^{20})^T \tag{6.14}$$

Due to the fading of the tags, myocardial deformation cannot be reliably extracted from frames after the end of systole (ES). Therefore, we only consider the image frames

from end of diastole (ED) to ES. In addition, the heart beat rate varies in human subjects, so that the frame number from ED to ES ranges from 5 to 12 in our training data. We implement a B-spline technique to interpolate them into 10 frames. Therefore, the myocardial motion of a tMRI time sequence can be represented by a 60×10-sized feature tensor $\mathbf{T} = [V_1, ..., V_{10}]$. As seen in Fig. 6.23, the feature tensor $\mathbf{T}$ exhibits noticeable differences between normal subjects and patients.

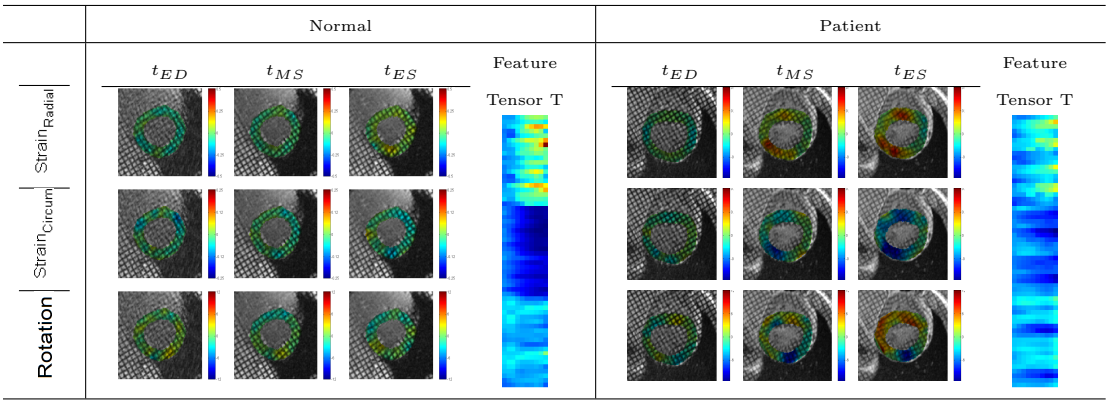

Figure 6.23: Visual comparison of normal (left-hand-side) and patient's (right-hand-side) radial strain (first row), circumferential strain (second row) and rotation angle (third row) estimations at the time of ED, MS and ES. For regional cardiac function analysis, we divided the left ventricle into 20 regions and interpolate the ED to ES deformation sequence into 10 frames, so as to form a 60×10-sized feature tensor $\mathbf{T}$, which is illustrated as a pseudo-color bar.

6.5.2 Spatio-Temporal Tensor LDA

Learn the classifier

Suppose we have collected N samples (including normal and abnormal) for training purposes. We can train a typical two-class classifier to make the normal samples far away from the abnormal samples. LDA is a popular method to maximize the between-class scatter and minimize the within-class scatter, but it is a vector-based method. If we reshape the spatio-temporal tensor feature into a vector, it will collapse the spatio-temporal structure information, which is very important for identification. Additionally, the conventional LDA can only project the features into a scalar in the two-class case. In this paper, we propose to use spatio-temporal tensor LDA to deal with the above issues, which can preserve the spatio-temporal information well, and it also has no

limitation on dimensionality reduction.

Let $\mathbf{T}_i, i \in [1, 2, ..., N]$ be training tensor features with the labels of normal and abnormal. Similar to LDA, the spatio-temporal tensor-based LDA (ST-LDA) also employs the Fisher criterion that maximizes the between-class scatter and minimizes the within-class scatter, but it extends the vector-based norm into the Frobenius norm [111]. With the tensor features $\mathbf{T}_i \in \mathfrak{R}^{60\times 10}$, the between-class scatter S_b and the within-class scatter S_w measured by the Frobenius norm are $S_b = \sum_{i=1}^{2} N_i \|M_i - M\|_F^2$ and $S_w = \sum_{i=1}^{2} \sum_{\mathbf{T}_j \in X_i} \|\mathbf{T}_j - M_i\|_F^2$, where N_i means the number of i-th class sample, and M is the mean matrix of all the $\mathbf{T}_i$, and M_i represents the mean matrix of the i-th class, and $\mathbf{T}_j \in X_i$ means that $\mathbf{T}_j$ belongs to the i-th class.

The goal is to find the optimal projection matrices $L \in \mathfrak{R}^{60\times d_L}$ and $R \in \mathfrak{R}^{10\times d_R}$ which maximize S_b and minimize S_w in the low dimensional subspace of $L \bigotimes R$, i.e., maximizing $S'_b = \sum_{i=1}^{2} N_i \|L^T(M_i - M)R\|_F^2$ and minimizing $S'_w = \sum_{i=1}^{2} \sum_{\mathbf{T}_j \in X_i} \|L^T(\mathbf{T}_j - M_i)R\|_F^2$ at the same time.

Because $\|X\|_F^2 = trace(XX^T)$, S'_b and S'_w can be written as $S'_b = trace(L^T D_b^R L)$ and $S'_w = trace(L^T D_w^R L)$ when R is given, where

$$D_b^R = \sum_{i=1}^{2} N_i (M_i - M) R R^T (M_i - M)^T \tag{6.15}$$

$$D_w^R = \sum_{i=1}^{2} \sum_{\mathbf{T}_j \in X_i} (\mathbf{T}_j - M_i) R R^T (\mathbf{T}_j - M_i)^T \tag{6.16}$$

Then we can get the optimal projection L by maximizing $trace((L^T D_w^R L)^{-1}(L^T D_b^R L))$, i.e., computing the eigenvectors of $(D_w^R)^{-1} D_b^R$.

Similarly, if L is fixed, we can rewrite S'_b and S'_w as $S'_b = trace(R^T D_b^L R)$ and $S'_w = trace(R^T D_w^L R)$, because of $trace(AB) = trace(BA)$, where

$$D_b^L = \sum_{i=1}^{2} N_i (M_i - M)^T L L^T (M_i - M) \tag{6.17}$$

$$D_w^L = \sum_{i=1}^{2} \sum_{\mathbf{T}_j \in X_i} (\mathbf{T}_j - M_i)^T L L^T (\mathbf{T}_j - M_i) \tag{6.18}$$

Input: $\mathbf{T}_1$,$\mathbf{T}_2$,...,$\mathbf{T}_N$
Initialization: Set $R_0 = (I_{d_R}, 0)^T$, and compute the mean M_i of the i-th class for each class, and the global mean M.
Iteration: For $t = 1$ **to** t_{max}
1). For a given R_{t-1}, compute D_w^R and D_b^R using Equations 6.16 and 6.15, and get the optimal L_t by solving for the first d_L leading eigenvectors of $(D_w^R)^{-1}D_b^R$.
2). Based on , compute D_w^L and D_b^L as in Equations 6.18 and 6.17, and get the optimal R_t by solving for the first d_R leading eigenvectors of $(D_w^L)^{-1}D_b^L$.
3). If $t > 1$, $\|L_t - L_{t-1}\| < \varepsilon$ and $\|R_t - R_{t-1}\| < \varepsilon$, break; else, continue.
End iteration.
Output: $L = L_{t_{max}}$ and $R = R_{t_{max}}$

Table 6.1: The ST-LDA algorithm.

Then the optimal projection can be obtained by maximizing $trace((R^T D_w^L R)^{-1}(R^T D_b^L R))$, i.e., solving for the eigenvectors of $(D_w^L)^{-1}D_b^L$.

Thus, the final optimal solution can be computed by an iterative procedure, as shown in Table 6.1. It can be found that the ST-LDA algorithm not only avoids the eigen-decomposition in the 600 dimensional space, but also well preserves the geometric relations of row and column of $\mathbf{T}_i$. In addition, in the conventional LDA, the available dimension has the upper bound $C - 1$, which means it will project onto a scalar in our normal/abnormal two classes situation, while ST-LDA has no such constraint and is able to keep more information, which will be essential when we back-project the low dimensional subspace feature to the original feature space and look for the ground of the classification.

For a new myocardial deformation pattern $\mathbf{T}_{test} \in \Re^{60\times 10}$, its projection in the reduced dimensional subspace is: $Y_{test} = L^T \mathbf{T}_{test} R \in \Re^{d_L \times d_R}$. Classification is done in this subspace using a k-nearest neighbor scheme, where we empirically set $k = 3$.

Regional abnormality analysis

Identifying and localizing abnormal cardiac regions could be of more clinical value than just classifying a heart as normal or diseased. The intuition behind the ST-LDA algorithm is that the high dimensional feature tensor can be projected into a lower

dimensional subspace that is optimal for classification. Therefore, the tensor distance between abnormal and normal features in the low dimensional subspace becomes a concise but accurate description of the abnormality. If we back-project this feature distance to the original space, we can recover the location of the pathology on the original spatio-temporal structure in a more physically meaningful way.

Because the linear projection functions L and R are not orthogonal matrices, the back-project operation needs to be done using their pseudo-inverse matrices L^+ and R^+. Suppose T_a is a feature tensor, and Y_a is its projection in the low dimensional subspace, which is classified as abnormal using the ST-LDA classifier. Then the feature distance in the original space can be derived by:

$$dT = (L^+)^T (Y_a - \bar{Y}_{normal}) R^+ \tag{6.19}$$

Since $dT \in \Re^{60\times 10}$ and we are more interested in recovering the spatial distribution of the cardiac function, we define an index of pathology $P_i, i = 1, 2, ..., 20$ that indicates each cardiac region's degree of functional abnormality. Note that P is a temporal and functional (including radial strain, circumferential strain and rotation angle) combination of the abnormal distances, therefore, it is no longer a descriptor of local strain or rotation angle, but rather a systematic indicator of the local cardiac function.

$$P_i = \sum_{t=1}^{10} (dT^2(i,t) + dT^2(20+i,t) + dT^2(40+i,t))^{\frac{1}{2}} \tag{6.20}$$

6.5.3 Experiments and Results

We acquired 41 time sequences of short-axis tagged MR images from 10 normal subjects and 12 patients. The patient's heart diseases varied from infarction or hypertrophy to general loss of myocardial function. The spatial positions of these SA images are confined to the mid-portion of the left ventricle, where the pathologies are usually prominent. In the ST-LDA classification algorithm, we empirically set the iteration number to 10, and the dimension of the subspace to 10×5, so that $L \in \Re^{60\times 10}$ and $R \in \Re^{10\times 5}$. To make comparisons with other conventional classification methods, we

Classification Algorithm	PCA	LDA	SVM	ST-LDA
Classification Accuracy Rate	73.17%	85.37%	87.80%	87.80%

Table 6.2: Comparison with other conventional classification algorithms.

applied PCA, LDA and SVM algorithms to the same data set. Their parameters are also empirically set to be optimal.

The training and testing procedures are strictly done on a leave-one patient-out-basis, i.e., we leave one patient data for testing, and use the rest for training. In Table 6.2, we list the accuracy rate comparison of PCA, LDA, SVM and our proposed ST-LDA. We find that our novel algorithm outperforms PCA and LDA in accuracy, and has a similar accuracy rate with the nonlinear approach SVM. On the other hand, PCA and ST-LDA is able to recover the regional abnormality by back-projecting the subspace feature to the original feature space, while LDA and SVM cannot.

In Fig. 6.24, we show some representative results of the regional cardiac function analysis. The regional abnormality is represented by the index P, which is encoded in the pseudo color map. Column (a) is from a normal sequence. We can observe that the P index is low and smoothly distributed. Column (b) is from an abnormal subject. The warm color indicates possible abnormal regions, such as the 1 and 5 o'clock regions, which agree with doctor's diagnosis. The high abnormality at the 7 o'clock region very likely comes from the LV-RV connecting area, whose motion is affected by both ventricles and therefore sensitive to pathology. Columns (c) and (d) are from a patient before and after a surgery, respectively. This patient had insertion of a "Coapsys" device to reduce functional mitral regurgitation. We can observe that the doctor's diagnosis (indicated by the surgical sites, which appear as dark dots in the MR image, and depicted as black dots in the analysis results) coincides with the abnormal regions from our analysis results very well. Furthermore, the overall performance is more normal as depicted in the overall cooler color in (d), which shows the effectiveness of this surgery. However, the myocardium at the two surgical sites were impaired in the surgery, which is why the cardiac function is still (or even more) abnormal near the surgical sites in (d). Our regional cardiac function analysis results perfectly agree with

the patient's pathologies before and after the operation.

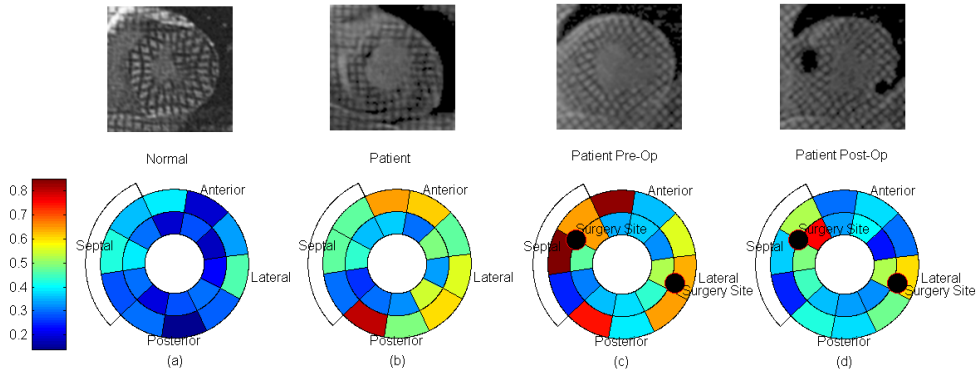

Figure 6.24: Quantitative analysis of the regional abnormality from the back-projection. Warm color represents high P value, which means high degree of abnormality. The first row shows the sampling images at ES from 4 time sequences. The second row shows the analysis results. Column (a) is from a normal sequence. Column (b) is from an abnormal subject. (c) and (d) are from a patient before and after a surgery, respectively. The black dots show the surgery sites.

6.5.4 Discussion

In this section, we proposed a novel spatio-temporal tensor-based LDA classification framework to detect and localize regional cardiac abnormality. The advantage of the proposed method is that its dimension reduction is separately operated in the spatial and temporal domains, so that it conserves better the spatio-temporal structure and information of the training data. In addition, in order to analyze regional cardiac function, we back-project the abnormality distance found in the subspace to the original feature space, so as to localize the regional abnormality in a more physically meaningful way. Our experimental results show our ST-LDA approach achieves a higher classification rate than conventional linear approaches, and achieves comparable accuracy rate to nonlinear method, such as SVM. The recovered regional abnormality agrees with doctor's diagnosis and patient's pathology very well.

6.6 Conclusion

In this chapter, we presented two 2D strain estimation methods in tagged MRI. We also developed a inter-modality registration method and conducted a comparison between tagged MRI and ultrasound elastography. The tracking-based methods track either the tagging lines or phase angles over time, and get the displacement map accumulatively. The strain value is derived from the displacement map. An advantage of this method is that it can incorporate temporal information, such as estimating the local speed, into tracking. Since it models the tagging lines or grids as deformable models, it is robust to local image noise. The disadvantage of this method is that the errors in displacement estimation from tracking are accumulative. Once the mis-tracking occurs, this method will fail in all the following frames.

The non-tracking based method measures the local tag spacings and orientations. The strain estimation is directly obtained from the tag's deformation. Thus, it doesn't need to tracking the tag pattern from the very first frame. The advantage of this method is that it is more efficient if we are only interested in a few frames of a full heart cycle. If in a few frames, especially frame 1 or 2 at the beginning of ED, the myocardium contracts at a very high speed, which leads to blurred tagging lines or grids, this method can still recover the strain values in the other frames. The disadvantage of this method is that it is sensitive to local image noise. Although after the filtering process, we can achieve a smooth strain estimation, the filtering process may lead to under-estimated strain values.

In practice, we have applied both methods on a large number of tagged MR images. Since in MR imaging, there is a trade-off between spatial and temporal resolutions, we found that the tracking-based method works better on images with high temporal resolution, while the non-tracking-based method works better on images with high spatial resolution.

The spatio-temporal tensor-based LDA classification works very well in detecting and localizing the regional abnormalities in myocardial function. The advantage of this method is that we formulate the abnormal detection into a classification problem, so

that it aims to maximize the between-class scatter and minimize the in-class scatter. Therefore, it is more efficient that training a normal or abnormal model from a limited number of training data sets. In addition, our tensor-based approach makes the algorithm more accurate and able to back-project to find the regional abnormalities.

Chapter 7

Conclusions and Future Topics

The main purpose of this dissertation involves developing automatic image analysis algorithms for cardiac tMRI, as part of an effort in pushing this technique into clinical use. Cardiac tMRI is well known for its ability of visualizing the myocardial intramural deformations in vivo. However, the lack of automated and reliable image analysis methods has prevented this imaging technique from routine clinical use. In this dissertation, a full range of image processing methods, such as tag enhancing and tracking, myocardial segmentation, and strain estimation for cardiac tMRI, have been developed.

To enhance and track the deformed tags, previous studies mainly focused on spectral filtering operations in the Fourier domain. However, these methods encounter difficulties in dealing with large myocardial deformation. In this research, a wavelet-like Gabor filter-based method has been developed, which is more locally adaptive. This Gabor based method was later extended to solve tasks such as tag removal, myocardial tracking, and strain estimation. Because of its wide applications, Gabor filtering has the potential to become a routine procedure in tMRI analysis systems.

Segmentation of the myocardial boundaries is a challenging task because of the complexity added by tagging. Previous studies mainly solved this problem by removing the tagging using spectral filtering or morphological operations, which are prone to blurred or merged boundaries. To address this problem, in this research we are the first that introduced statistical shape analysis, learning-based local appearance modeling, and sampling-based tracking techniques into cardiac tMRI. Thus, the prior knowledge of the anatomy (represented as the statistical shape model), the special tMRI image characteristics (represented as the local appearance model), and the cardiac motion

patterns (represented in the sampling-based tracking method) can be naturally integrated into the segmentation framework. To automatically initialize the segmentation, we also developed a heart detection and localization method based on machine learning algorithms. The experimental results of our algorithm achieved highly accurate and robust segmentation of the left/right ventricular endocardium, and the epicardium. This success indicates that prior knowledge is of great importance for solving medical image analysis tasks, and machine learning methods provide good avenues to extract it.

A main goal of cardiac tMRI is to estimate myocardial strain. Some research groups have recently been developing ultrasound-based strain estimation methods. It is of interests for both MRI and ultrasound communities to conduct a comparison between tMRI and ultrasound. For inter-modality comparison, the most difficult part is registration. In this research, we developed an inter-modality registration method for 3D tMRI and 2D RF Ultrasound, by generating pseudo ultrasound images from tMRI so that the mutual information-based registration method could work. This comparison work gives valuable insights into the pros and cons of the two imaging modalities.

In medical image analysis, it is a good practice to keep improving the available methods in accordance with the advancing of the imaging techniques. While the old Gabor-based tag removal method still works, we developed a new Mean-Shift and band-stop filtering based method to suppress the tagging specifically for MESSFP tMRI, which is a recently developed imaging technique that achieves excellent contrast between myocardium and blood pool. This new method preserves the appearance of the original images with high resolution. Using a conventional Markov Random Field segmentation method, we have achieved very accurate ventricular endocardium segmentation, from which it is noticeable that the papillary muscles can be automatically segmented for the first time in tMRI.

There are several directions that this research can be further developed in. First, I plan to improve the statistics and learning-based segmentation methods by formulating more sophisticated and efficient shape and appearance models, such as the nonlinear shape models, which are more suitable for the highly nonlinear cardiac shape and motion. We can also implement incremental learning schemes, which are more efficient

than the current offline learning method. Second, it is of great interest to analyze the myocardial diastolic motion. Current research mainly focuses on the systolic process. However, when many cardiovascular diseases take place, abnormality in diastolic motion appears earlier than in systolic. To achieve earlier heart disease detection, I would like to modify the imaging cycle, and pay more attention to diastolic motion analysis. Third, I plan to continue in developing diagnosis tools using myocardial motion information. Certain pathologies correlate very closely to myocardial motion change. In this dissertation, we developed a tensor-based classification method to detect and localize the abnormalities in regional myocardial function. By acquiring and processing more image data, from both normal and abnormal subjects with different diseases, I will be able to diagnose pathologies using motion pattern classification algorithms for multiple classes.

References

[1] : The world health report 2007 - A safer future: global public health security in the 21st century. World Health Organization (2007)

[2] Rosamond, W., et al: Heart Disease and Stroke Statistics – 2007 Update. American Heart Association (2007)

[3] Nesto, R., Kowalchuk, G.: The ischemic cascade: temporal sequence of hemodynamic, electrocardiographic and symptomatic expressions of ischemia. Am J Cardiol **59** (1987) 23c–30c

[4] Pai, V.M., Axel, L.: Advances in mri tagging techniques for determining regional myocardial strain. Current Cardiology Reports **8** (2006) 53–58

[5] Ohnesorge, B., Flohr, T., Becker, C., Knez, A., Kopp, A., Reiser, M.: High temporal resolution ECG-gated multi-slice spiral CT: A new method for 3D and '4D' cardiac imaging. Eur Radiol **10** (2000) Suppl 1:283

[6] Ohnesorge, B., Flohr, T., Becker, C., Kopp, A., Schoepf, U., Baum, U., Knez, A., Klingenbeck-Regn, K., Reiser, M.: Cardiac imaging by means of electrocardiographically gated multisection spiral CT: initial experience. Radiology **217** (2000) 564–571

[7] Kopp, A.F., Schroeder, S., Kuettner, A., Heuschmid, M., Georg, C., Ohnesorge, B., Kuzo, R., Claussen, C.D.: Coronary arteries: Retrospectively ECG-gated multi-detector row CT angiography with selective optimization of the image reconstruction window. Radiology **221** (2001) 683–688

[8] Ohnesorge, B., Flohr, T.: Non-invasive cardiac imaging with fast multi-slice cardio CT. Electromedica Cardiology (2000)

[9] Becker, C.R.: Advances in cardiac imaging. Journal European Radiology **13, supplement 3** (2003) N50–N52

[10] Saito, K., Saito, M., Komatu, S., Ohtomo, K.: Real-time four-dimensional imaging of the heart with multi-detector row CT. RadioGraphics **23** (2003) 8e

[11] Pujadas, S., Reddy, G.P., Weber, O., Lee, J.J., Higgins, C.B.: MR imaging assessment of cardiac function. Journal of Magnetic Resonance Imaging **19** (2004) 789–799

[12] Guillem, P.L.: Assessment of cardiac function by CMR. Journal European Radiology Supplements **15, supplement 2** (2005) B23–B32

[13] Zerhouni, E.A., Parish, D.M., Rogers, W.J., Yang, A., Shapiro, E.P.: Human heart: tagging with mr imaging - a method for noninvasive assessment of myocardial motion. Radiology **169** (1988) 59–63

[14] Axel, L., Dougherty, L.: Mr imaging of motion with spatial modulation of magnetization. Radiology **171** (1989) 841–845

[15] Fischer, S., McKinnon, G., Maier, S., Boesiger, P.: Improved myocardial tagging contrast. Magnetic Resonance in Medicine **30** (1993) 191–200

[16] Herzka, D., Guttman, M., McVeigh, E.: Myocardial tagging with SSFP. Magnetic Resonance in Medicine **49** (2003) 329–340

[17] Zwanenburg, J., Kuijer, J., Marcus, J., Heethaar, R.: Steadystate free precession with myocardial tagging: CSPAMM in a single breathhold. Magnetic Resonance in Medicine **49** (2003) 722–730

[18] Herzka, D., Kellman, P., Aletras, A., et al: Multishot EPISSFP in the heart. Magnetic Resonance in Medicine **47** (2002) 655:664

[19] Sled, J., Zijdenbos, A., Evans, A.: A nonparametric method for automatic correction of intensity nonuniformity in mri data. IEEE Transactions on Medical Imaging **17** (1998) 87–97

[20] Wells, W., Grimson, W., Kikinis, R., Jolesz, F.: Adaptive segmentation of mri data. IEEE Transactions on Medical Imaging **15** (1996) 429–442

[21] Salvado, O., Hillenbrand, C., Zhang, S., Wilson, D.: Method to correct intensity inhomogeneity in mr images for atherosclerosis characterization. Medical Imaging, IEEE Transactions on **25** (2006) 539–552

[22] Styner, M., Brechbuhler, C., Szekely, G., Gerig, G.: Parametric estimate of intensity inhomogeneities applied to MRI. Medical Imaging, IEEE Transactions on **19** (2000) 153–165

[23] Madabhushi, A., Udupa, J.K.: The interplay of intensity and inhomogeneity correction in mr image analysis. IEEE Transactions on Medical Imaging **24** (2005) 561–576

[24] Montillo, A., Udupa, J., Axel, L.: Interaction between noise suppression and inhomogeneity correction in mri. In: Proceedings of SPIE: Medical Imaging. Volume 5032. (2003) 1025–1036

[25] Axel, L., Costantini, J., Listerud, J.: Intensity correction in surface-coil mr iamging. American Journal of Radiology **148** (1987) 418–420

[26] Nyul, L., Udupa, J., Zhang, X.: New variants of a method of mri scale standardization. IEEE Transactions on Medical Imaging **19(2)** (2000) 143–150

[27] Guttman, M., Prince, J., McVeigh, E.: Tag and contour detection in tagged MR images of the left ventricle. IEEE Transactions on Medical Imaging **13** (1994)

[28] Young, A.: Model tags: direct 3D tracking of heart wall motion from tagged magnetic resonance images. In: Proceedings of Medical Image Computing and Computer-assisted Intervention. (1998) 92–101

[29] Amini, A., Prince, J.: Measurement of Cardiac Deformations from MRI: Physical and Mathematical Models. Kluwer Academic Publishers, Dordrecht (2001)

[30] Dougherty, L., Asmuth, J., Blom, A., Axel, L., Kumar, R.: Validation of an optical flow method for tag displacement estimation. IEEE Transactions on Medical Imaging **18** (1999) 359–363

[31] Prince, J., McVeigh, E.: Motion estimation from tagged MR image sequences. IEEE Transactions on Medical Imaging **11** (1992) 238–249

[32] McVeigh, E., Atalar, E.: Cardiac tagging with breath-hold cine MRI. (1992)

[33] Kraitchman, D., Young, A., Chang, C., Axel, L.: Semiautomated tracking of myocardial motion in MR tagged images. IEEE Transactions on Medical Imaging **14** (1995) 422–433

[34] Chandrashekara, R., Mohiaddin, R., Rueckert, D.: Analysis of myocardial motion in tagged MR images using non-rigid image registration. In: Proceedings of the SPIE Medica Imaging: Image Processing. (2002) 1168–1179

[35] Denney, T., Prince, J.: Optimal brightness functions for optical flow estimation of deformable motion. IEEE Transactions on Image Processing **3** (1994)

[36] Osman, N., Kerwin, W., McVeigh, E., Prince, J.: Cardiac motion tracking using CINE harmonic phase (HARP) magnetic resonance imaging. Magnetic Resonance in Medicine **42** (1999) 1048–1060

[37] Garot, J., Bluemke, D., Osman, N., Rochitte, C., McVeigh, E., Zerhouni, E., Prince, J., Lima, J.: Fast determination of regional myocardial strain fields from tagged cardiac images using harmonic phase (HARP) magnetic resonance imaging. Circulation **101** (2000) 981–988

[38] Montillo, A., Metaxas, D., Axel, L.: Automated segmentation of the left and right ventricles in 4D cardiac SPAMM images. In: Proceedings of Medical Image Computing and Computer-assisted Intervention. (2002) 620–633

[39] Manglik, T., Axel, L., Pai, W., Kim, D., Dugal, P., Montillo, A., Qian, Z.: Use of bandpass gabor filters for enhancing blood-myocardium contrast and filling-in tags in tagged mr images. In: Proc of Int'l Society for Mag. Res. In Med. (2004) 1793

[40] Young, A.: Model tags: direct 3D tracking of heart wall motion from tagged magnetic resonance images. Medical Image Analysis **3** (1999) 361–372

[41] Haber, I., Metaxas, D., Axel, L.: Three-dimensional motion reconstruction and analysis of the right ventricle using tagged MRI. Medical Image Analysis **4** (2000) 335–355

[42] Park, J., Metaxas, D., Young, A., Axel, L.: Deformable models with parameter functions for cardiac motion analysis. IEEE Transactions on Medical Imaging **15** (1996) 278–289

[43] Declerck, J., Feldmar, J., Ayache, N.: Definition of a 4d continuous planispheric transformation for the tracking and the analysis of LV motion. Medical Image Analysis **2** (1998) 197–213

[44] Daugman, M., Zerhouni, E., Mcveigh, E.: Analysis of cardiac function from mr images. IEEE Computer Graphics and Application **17** (1997) 30–38

[45] Park, K., Metaxas, D., Axel, L.: A finite element model for functional analysis of 4D cardiac-tagged MR images. In: Proceedings of Medical Image Computing and Computer-assisted Intervention. (2003) 491–498

[46] Park, K., Montillo, A., Metaxas, D., Axel, L.: Volumetric heart modeling and analysis. Commun. ACM **48** (2005) 43–48

[47] Hu, Z., Metaxas, D.N., Axel, L.: In-vivo strain and stress estimation of the left ventricle from mri images. In: MICCAI (1). (2002) 706–713

[48] Hu, Z., Metaxas, D.N., Axel, L.: Computational modeling and simulation of heart ventricular mechanics from tagged mri. In: FIMH. (2005) 369–383

[49] Axel, L., Chen, T., Manglik, T.: Dense myocardium deformation estimation for 2D tagged MRI. In: FIMH. (2005) 446–456

[50] Osman, N.F., Prince, J.L.: Angle images for measuring heart motion from tagged mri. In: Proc. IEEE Int'l Conf. Image Proc. (1998)

[51] Osman, N.F., Prince, J.L.: On the design of the bandpass filters in harmonic phase mri. In: Proc. IEEE Int'l Conf. Image Proc. (2000)

[52] Dunn, D., Higgins, W.E., Wakeley, J.: Texture segmentation using 2-d gabor elementary functions. IEEE Trans. Pattern Anal. and Machine Intell **16** (1994) 130–149

[53] Weldon, T.P., Higgins, W.E., Dunn, D.F.: Efficient gabor filter design for texture segmentation. Journal of Pattern Recognition **29** (1996) 2005–2016

[54] Weldon, T.P., Higgins, W.E.: An algorithm for designing multiple gabor filters for segmenting multitextured images. In: IEEE Int'l Conf. on Image Processing. Volume 3. (1998) 333–337

[55] Mehrotra, R., Namuduri, K.R., Ranganathan, N.: Gabor filter-based edge detection. Journal of Pattern Recognition **25** (1992) 1479–1493

[56] Daugman, J.: Uncertainty relation for resolution in space, spatial frequency, and orientation optimized by two-dimensional visual cortical filters. Journal of the Optical Society of America A **2** (1985) 1160–1169

[57] Kass, M., Witkin, A., Terzopoulos, D.: Snakes: Active contour models. Int'l Journal of Computer Vision **1** (1987) 321–331

[58] Qian, Z., Montillo, A., Metaxas, D., Axel, L.: Segmenting cardiac mri tagging lines using gabor filter banks. In: Proc of Int'l Conf. of the Engineering in Medicine and Biology Society. (2003) 630–633

[59] Qian, Z., Huang, X., Metaxas, D., Axel, L.: Robust segmentation of 4d cardiac mri-tagged images via spatio-temporal propagation. In: Proceedings of SPIE Medical Imaging: Physiology, Function, and Structure from Medical Images. Volume 5746. (2005) 580–591

[60] Cheng, Y.: Mean Shift, Mode Seeking, and Clustering. IEEE Trans. on Pattern Analysis and Machine Intelligence **17** (1995)

[61] Comaniciu, D., Meer, P.: Mean Shift: A robust approach toward feature space analysis. IEEE Trans. on Pattern Analysis and Machine Intelligence **24** (2002)

[62] Huang, R., Pavlovic, V., Metaxas, D.: A Graphical Model framework for coupling MRFs and deformable models. In: IEEE Conf. on Computer Vision and Pattern Recognition. Volume 2. (2004) 739–746

[63] Fukunaga, K., Hostetler, L.: The estimation of the gradient of a density function, with applications in pattern recognition. IEEE Trans. Information Theory **21** (1975) 32–40

[64] Comaniciu, D., Ramesh, V., Meer, P.: Real-time tracking of non-rigid objects using Mean Shift. In: IEEE Conf. on Computer Vision and Pattern Recognition. Volume 2. (2000) 142–149

[65] Huang, X., Metaxas, D., Chen, T.: Metamorphs: Deformable shape and texture models. In: IEEE Conf. on Computer Vision and Pattern Recognition. Volume 1. (2004) 496–503

[66] Montillo, A., Axel, L., Metaxas, D.: Extracting tissue deformation using gabor filter banks. In: Proc of SPIE: Medical Imaging: Physiology, Function, and Structure from Medical Images. Volume 5369. (2004) 1–9

[67] Huang, X., Paragios, N., Metaxas, D.: Establishing local correspondences towards compact representations of anatomical structures. In: Proc. of Int'l Conf. on Medical Imaging Computing and Computer-Assisted Intervention, LNCS 2879. (2003) 926–934

[68] Osher, S., Sethian, J.: Fronts propagating with curvature-dependent speed : Algorithms based on the Hamilton-Jacobi formulation. Journal of Computational Physics **79** (1988) 12–49

[69] Sederberg, T.W., Parry, S.R.: Free-form deformation of solid geometric models. In: Proceedings of the 13th Annual Conference on Computer Graphics. (1986) 151–160

[70] Amini, A.A., Chen, Y., Elayyadi, M., Radeva, P.: Tag surface reconstruction and tracking of myocardial beads from SPAMM-MRI with parametric b-spline surfaces. IEEE Transactions on Medical Imaging **20** (2001) 94–103

[71] Ginneken, B.V., Frangi, A.F., Staal, J.J., et al: Active shape model segmentation with optimal features. IEEE Trans. on Medical Imaging **21** (2002)

[72] Jiao, F., Li, S., Shum, H., Schuurmans, D.: Face alignment using statistical models and wavelet features. In: IEEE Conf. on CVPR. Volume 1. (2003) 321–327

[73] Li, S., Zhu, L., Jiang, T.: Active shape model segmentation using local edge structures and adaboost. In: Medical Imaging Augmented Reality. (2004)

[74] Cootes, T., Taylor, C., Cooper, D., Graham, J.: Active shape models - their training and application. Computer Vision and Image Understanding **61** (1995) 38–59

[75] Freund, Y., Schapire, R.E.: A decision-theoretic generalization of on-line learning and an application to boosting. In: EuroCOLT '95: Proceedings of the Second European Conference on Computational Learning Theory. (1995) 23–37

[76] Schapire, R.E.: The boosting approach to machine learning: An overview. In: In MSRI Workshop on Nonlinear Estimation and Classification. (2002)

[77] R. E. Schapire, Y. Freund, P.B., Lee, W.S.: Boosting the margin: a new explanation for the effectiveness of voting methods. Annals of Statistics **26** (1998) 1651–1686

[78] Bichsel, M.: Strategies of Robust Objects Recognition for Automatic Identification of Human Faces. PhD thesis (1991)

[79] Brunelli, R., Poggio, T.: Face recognition: Features versus templates. IEEE Trans. on Pattern Analysis and Machine Intelligence **15** (1993) 1042–1052

[80] Pentland, A., Moghaddam, B., T., S.: View-based and modilar eigenspaces for face recognition. In: IEEE Conf. on Computer Vision and Pattern Recognition. (1997)

[81] Yuille, A., Hallinan, P., Cohen, D.: Face recognition: Features versus templates. Int'l Journal of Computer Vision **15** (1992) 99–111

[82] Poggio, T., Sung, K.K.: Example-based learning for view-based human face detection. In: Proc. of the ARPA Image Understanding Workshop. II. (1997) 843–850

[83] Papageorgiou, C.P., Oren, M., Poggio, T.: A general framework for object detection. In: IEEE Int'l Conf. on Computer Vision. (1998)

[84] Viola, P., Jones, M.: Robust real-time object detection. Second International Workshop on Statistical and Computational Theories of Vision - Modeling, Learning, And Sampling. Vancouer, Canada, July 13 (2001)

[85] Sun, W., Cetin, M., Chan, R., Reddy, V., Holmvang, G., Chandar, V., Willsky, A.: Segmenting and tracking the left ventricle by learning the dynamics in cardiac images,. In: Proc. of Information Processing in Medical Imaging. (2005) 553–565

[86] Chandrashekara, R., Mohiaddin, R., Rueckert, D.: Analysis of 3-d myocardial motion in tagged mr images using nonrigid image registration. IEEE Trans. Med. Imaging **23** (2004) 1245–1250

[87] Comaniciu, D., Zhou, X.S., Krishnan, S.: Robust real-time myocardial border tracking for echocardiography: an information fusion approach. IEEE Trans. Med. Imaging **23** (2004) 849–860

[88] Georgescu, B., Zhou, X.S., Comaniciu, D., Rao, B.: Real-time multi-model tracking of myocardium in echocardiography using robust information fusion. In: MICCAI (2). (2004) 777–785

[89] Jacob, G., Noble, J., Behrenbruch, C., Kelion, A., Banning, A.: A shape-space-based approach to tracking myocardial borders andquantifying regional left-ventricular function applied inechocardiography. **21** (2002) 226–238

[90] II, J.C.M., Duncan, J.S.: Shape-based tracking of left ventricular wall motion. IEEE Trans. Med. Imaging **16** (1997) 270–283

[91] Isard, M., Blake, A.: Contour tracking by stochastic propagation of conditional density. In: ECCV (1). (1996) 343–356

[92] Qian, Z., Metaxas, D., Axel, L.: A learning framework for the automatic and accurate segmentation of cardiac tagged mri images. In: In Proceedings Of CVIBA Workshop, In Conjuction with ICCV, LNCS 3765. (2005) 93–102

[93] Bree, D., et al: Low-dose dobutamine tissue-tagged magnetic resonance imaging with 3-dimensional strain analysis allows assessment of myocardial viability in patients with ischemic cardiomyopathy. Circulation **114** (2007) I33–I36

[94] Lai, W.M.: Introduction to Continuum Mechanics. 3rd edn. Butterworth-Heinemann (1993)

[95] Konofagou, E.E., Dhhooge, J., Ophir, J.: Myocardial elastography-a feasibility study in vivo. Ultrasound in Med. & Bio. **28** (2002) 475–482

[96] Lee, W.N., Konofagou, E.E.: Analysis of 3D motion effects in 2D myocardial elastography. In: IEEE-UFFC Symp. Proc. (2006) 1217–1220

[97] Notomi, Y., et al: Measurement of ventricular torsion by two-dimensional ultrasound speckle tracking imaging. J. Am. Coll. Cardiol. **45** (2005) 2034–2041

[98] Helle-Valle, T., et al: New noninvasive method for assessment of left ventricular rotation - *s*peckle tracking echocardiography. Circulation **112** (2005) 3149–3156

[99] Cho, G., et al: Comparison of two-dimensional speckle and tissue velocity based strain and validation with harmonic phase magnetic resonance imaging. The American Journal of Cardiology **97** (2006) 1661–1666

[100] Lee, W., et al: Validation of ultrasound myocardial elastography using MR tagging in normal human hearts in vivo. In: ISBI. (2007)

[101] Makela, T., et al: A review of cardiac image registration methods. IEEE Trans. Med. Imaging **21** (2002) 1011–1021

[102] Roche, A., Pennec, X., Malandain, G., Ayache, N.: Rigid registration of 3D ultrasound with MR images: a new approach combining intensity and gradient information. IEEE Trans. Med. Imaging **20** (2001) 1038–1049 PMID: 11686439.

[103] Huang, X., et al: Dynamic 3D ultrasound and MR image registration of the beating heart. In: MICCAI (2). (2005) 171–178

[104] Qian, Z., Metaxas, D., Axel, L.: Extraction and tracking of MRI tagging sheets using a 3D Gabor filter bank. In: Proc of Int'l Conf. of the Engineering in Medicine and Biology Society. (2006)

[105] Osman, N.F., McVeigh, E.R., Prince, J.L.: Imaging heart motion using harmonic phase MRI. IEEE Trans. Med. Imaging **19** (2000) 186–202

[106] Osman, N.F., Prince, J.L.: Visualizing myocardial function using HARP MRI. Phys. Med. Biol **45** (2000) 1665–1682

[107] E., P.M., A., B., L., Z.B.: Range of normal values for left and right ventricular ejection fraction at rest and during exercise assessed by radionuclide angiocardiography. European Heart Journal **6** (1985)

[108] Qian, Z., Huang, R., Metaxas, D., Axel, L.: A novel tag removal technique for tagged cardiac MRI and its applications. In: Proc. of IEEE Int'l Symposium on Biomedical Imaging. (2007) 364–367

[109] Kraitchman, D., Sampath, S., Derbyshire, J., Bluemke, D., Gerber, B., Prince, J., Osman, N. In: Proc. of the International Conference of the IEEE Engineering in Medicine and Biology Society. Volume 3. (2001) 2598–2601

[110] Clarysse, P., Han, M., Croisille, P., Magnin, I.E.: Exploratory analysis of the spatio-temporal deformation of the myocardium during systole from tagged MRI. IEEE Trans. Biomed. Eng. **49** (2002) 1328–1339

[111] Ye, J.P., Janardan, R., Li, Q.: Two-dimensional linear discriminant analysis. In: Proc. of. Int. Conf. Neural Information Processing Systems. (2004)

Curriculum Vita

Zhen Qian

Education:

09/2001-05/2008	Ph.D. Rutgers University-New Brunswick, Department of Biomedical Engineering,
09/2001-10/2007	M.S. Rutgers University-New Brunswick, Department of Computer Science,
09/1996-07/1999	B.S. South China University of Technology, Department of Electronic And Information Engineering,

Experiences:

06/2002-06/2008	Rutgers University-New Brunswick, Department of Biomedical Engineering, Graduate Assistant
09/2007-01/2008	Rutgers University-New Brunswick, Department of Computer Science, Teaching Assistant

Publications:

1. Z. Qian, D. Metaxas, and L. Axel, "Non-tracking-based 2D strain estimation in tagged MRI." In Proc. of IEEE International Symposium on Biomedical Imaging (ISBI), Accepted, 2008.

2. W-N. Lee, Z. Qian, C. L. Tosti, T. R. Brown, D. Metaxas, and E. E. Konofagou, "Validation of Angle-Independent Myocardial Elastography Using MR Tagging in Human Subjects In Vivo." In Ultrasound in medicine and biology, Accepted. 2008.

3. J. Maikos, Z. Qian, D. Metaxas, and D. Shreiber, "Finite Element Analysis of Spinal Cord Injury in the Rat." In Journal of Neurotrauma, Accepted. 2008.

4. Z. Qian, X. Huang, L. Axel, and D. Metaxas, "Automatic Segmentation of Cardiac Tagged MRI", Book Chapter in Biomedical Image Analysis: Methodologies and Applications, N. Paragios, J. Duncan and N. Ayache (Editors), Springer, 2008. (In

press).

5. X. Wang, W. He, Z. Qian, D. Metaxas, R. Mathew, and E. White, "Cell segmentation for division rate estimation in computerized video time-lapse microscopy", Book Chapter in Image Analysis for Life Science Applications, J. Rittscher, R. Machiraju and S. Wong (Editors), Artech House, 2008. (In press).

6. Z. Qian, W-N. Lee, D. Metaxas, and E. E. Konofagou, "Ultrasound myocardial elastography and registered 3D tagged MRI: quantitative strain comparison." In Proc. of the 10th International Conference on Medical Image Computing and Computer Assisted Intervention (MICCAI), pp. 800-808, 2007.

7. Z. Qian, D. Metaxas, and L. Axel, "Learning methods in segmentation of cardiac tagged MRI." In Proc. of IEEE International Symposium on Biomedical Imaging (ISBI), oral presentation, pp. 688-691, 2007.

8. Z. Qian, R. Huang, D. Metaxas, and L. Axel, "A novel tag removal technique for tagged cardiac MRI and its applications." In Proc. of IEEE International Symposium on Biomedical Imaging (ISBI), pp. 364-367, 2007.

9. W-N. Lee, Z. Qian, C. L. Tosti, S. V. Swaminatha, T. R. Brown, D. Metaxas, and E. E. Konofagou, "Validation of 2D Ultrasound-based Strain Estimates with MR Tagging." In Proc. of the International Society for Magnetic Resonance in Medicine (ISMRM), 2007.

10. W-N. Lee, Z. Qian, C. L. Tosti, S. V. Swaminatha, T. R. Brown, D. Metaxas, and E. E. Konofagou, "Validation of ultrasound myocardial elastography using MR tagging in normal human hearts in vivo." In Proc. of IEEE International Symposium on Biomedical Imaging (ISBI), pp 684-687, 2007.

11. W-N. Lee, Z. Qian, D. Metaxas and E. E. Konofagou, Clinical Validation of Angle-Independent Myocardial Elastography Using MRI Tagging, In IEEE International Ultrasonics Symposium (UFFC), New York, NY, Oct. 28-31. Oral presentation, 2007.

12. J. Maikos, R. Elias, Z. Qian, D. Metaxas, and D. Shreiber, "In Vivo Tissue-Level Thresholds for Spinal Cord Injury." In Proc. of ASME 2007 Summer Bioengineering Conference, 2007.

13. X. Wang, J. Schaerer, S. Huh, Z. Qian, D. Metaxas, T. Chen, and L. Axel, "Reconstruction of detailed left ventricle motion from tMRI using deformable models." In Proc. of International Conf. on Functional Imaging and Modeling of the Heart (FIMH), pp 60-69, 2007.

14. Z. Qian, D. Metaxas, and L. Axel, "Boosting and Nonparametric Based Tracking of Tagged MRI Cardiac Boundaries." In Proc. of the 9th International Conference on Medical Image Computing and Computer Assisted Intervention (MICCAI), LNCS

4190, pp 636-644. 2006.

15. J. Schaerer, Z. Qian, P. Clarysse, D. Metaxas, L. Axel, and I. Magnin, "Fast and Automated Creation of Patient-Specific 3D Heart Models from Tagged MRI" In Proc. Of Workshop on From Statistical Atlases to Personalized Models: Understanding Complex Diseases in Populations and Individuals, In Conjunction with MICCAI, 2006.

16. Z. Qian, D. Metaxas, and L. Axel, "Extraction and Tracking of MRI Tagging Sheets Using a 3D Gabor Filter Bank." in Proc. of International Conf. of the Engineering in Medicine and Biology Society, oral presentation, pp. 711-714, 2006.

17. D. Metaxas, Z. Qian, X. Huang, R. Huang, T. Chen and L. Axel, "Hybrid Deformable Models for Medical Segmentation and Registration" in Proc. of International Conf. on Control, Automation, Robotics and Vision, 2006.

18. D. Metaxas, L. Axel, Z. Qian and X. Huang, "A Segmentation and Tracking system for 4D Cardiac Tagged MR Images." in Proc. of International Conf. of the Engineering in Medicine and Biology Society, pp. 1541-1544, 2006.

19. Z. Qian, D. Metaxas, and L. Axel, "A Learning Framework for the Automatic and Accurate Segmentation of Cardiac Tagged MRI Images." In Proc. of CVIBA Workshop, In Conjunction with ICCV, LNCS 3765, pp. 93-102, 2005.

20. X. Huang, Z. Qian, R. Huang, and D Metaxas, "Deformable-model based Textured Object Segmentation", In Proc. of the 4th Int'l Workshop on Energy Minimization Methods in Computer Vision and Pattern Recognition (EMMCVPR), LNCS 3757, pp. 119-135, 2005.

21. Z. Qian, X. Huang, D. Metaxas, and L. Axel, "Robust Segmentation of 4D Cardiac MRI-tagged Images via Spatio-temporal Propagation", In Proc. Of SPIE, Medical Imaging, Physiology, Function, and Structure from Medical Images. Vol. 5746, pp. 580-591. 2005.

22. Z. Qian, A. Montillo, D. Metaxas, L. Axel, "Segmenting cardiac MRI tagging lines using Gabor filter banks", in Proc. of International Conf. of the Engineering in Medicine and Biology Society, oral presentation, pp. 630-633, 2003.

23. D. Metaxas, L. Axel, Z. Hu, A. Montillo, K. Park and Z. Qian, "Segmentation and Analysis of 3D Cardiac Motion from Tagged MRI Images" in Proc. of International Conf. of the Engineering in Medicine and Biology Society, pp. 122-125, 2003.

24. T. Manglik, L. Axel, Z. Qian, V. M. Pai, D. Kim, P. Dugal, A. Montillo, "Use of Bandpass Gabor Filters for Enhancing Blood-Myocardium Contrast and Filling-in tags in tagged MR Images", in Proc. of the International Society for Magnetic Resonance in Medicine (ISMRM), 2003.